# Single Ion Impact Detection & Scanning Probe Aligned Ion Implantation for Quantum Bit Formation

Dissertation
zur Erlangung des akademischen Grades
Doktoringenieur (Dr.-Ing.)

vorgelegt der
Fakultät für Elektrotechnik und Informationstechnik
der Technischen Universität Ilmenau

von
Dipl.-Ing. Christoph D. Weis

Gutachter:
1. Herr Univ.-Prof. Dr.-Ing. habil. I. W. Rangelow
2. Herr Univ.-Prof. Dr. rer. nat. habil. G. Gobsch
3. Herr Dr. T. Schenkel

urn:nbn:de:gbv:ilm1-2012000064

# Abstract

Quantum computing and quantum information processing is a promising path to replace classical information processing via conventional computers which are approaching fundamental physical limits. Instead of classical bits, quantum bits (qubits) are utilized for computing operations. Due to quantum mechanical phenomena such as superposition and entanglement, a completely different way of information processing is achieved, enabling enhanced performance for certain problem sets. Various proposals exist on how to realize a quantum bit. Among them are electron or nuclear spins of defect centers in solid state systems. Two such candidates with spin degree of freedom are single donor atoms in silicon and nitrogen vacancy (NV) defect centers in diamond. Both qubit candidates possess extraordinary qualities which makes them promising building blocks. Besides certain advantages, the qubits share the necessity to be placed precisely in their host materials and device structures. A commonly used method is to introduce the donor atoms into the substrate materials via ion implantation. For this, focused ion beam systems can be used, or collimation techniques as in this work. A broad ion beam hits the back of a scanning probe microscope (SPM) cantilever with incorporated apertures. The high resolution imaging capabilities of the SPM allows the non destructive location of device areas and the alignment of the cantilever and thus collimated ion beam spot to the desired implant locations. In this work, this technique is explored, applied and pushed forward to meet necessary precision requirements. The alignment of the ion beam to surface features, which are sensitive to ion impacts and thus act as detectors, is demonstrated. The technique is also used to create NV center arrays in diamond substrates. Further, single ion impacts into silicon device structures are detected which enables deliberate single ion doping.

# Kurzzusammenfassung

Daten- und Informationsverarbeitung via Quantencomputer ist ein viel versprechender Ansatz, um die klassische Art und Weise via Digitalrechner, welche sich fundamentalen physikalischen Grenzen annähern, zu ersetzen. Anstelle von klassischen Bits werden Quantenbits (Qubits) für Rechenoperationen verwendet. Aufgrund quantenmechanischer Phänomene wie Superposition und Verschränkung, wird die Informationsverarbeitung in einer ganz anderen Art und Weise umgesetzt und eine Leistungssteigerung für bestimmte Aufgabenstellungen erreicht. Es gibt verschiedene Vorschläge zur technischen Umsetzung von Quanten-Bits. Unter ihnen sind Elektronen- oder Kernspins von Defektstellen in Festkörpern. Zwei solche Kandidaten mit Spinfreiheitsgraden sind einzelne Donatoren in Silizium und Stickstoff Fehlstellen (NV) Zentren in Diamant. Beide Qubit-Kandidaten besitzen aussergewöhnliche Eigenschaften, welche sie zu vielversprechenden Bausteinen machen. Neben gewissen Vorteilen verbindet die beiden Qubits auch die Notwendigkeit, diese präzise in ihren Trägermaterialien und Bauelementstrukturen zu platzieren. Eine häufig verwendete Methode, die Fremdatome in die Substratmaterialien einzubringen, ist die Ionenimplantation. Hierfür können fokussierte Ionenstrahl-Systeme verwendet werden, oder Kollimationstechniken, wie in dieser Arbeit. Ein ausgedehnter Ionenstrahl trifft die Rückseite einer Rastersondenmikroskopspitze mit integrierten Öffnungen. Das Rastersondenmikroskop ermöglichen die zerstörungsfreie und hochauflösende Abbildung von Bauteilstrukturen und die Platzierung der Rastersondenmikroskopspitze, und damit des kollimierten Ionenstrahls, um ausgewählte Regionen zu implantieren. In der vorgelegten Arbeit wird diese Technik angewendet und weiterentwickelt, um notwendige Präzisionskriterien zu erfüllen. Die Platzierung des Ionenstrahls auf Bauelementstrukturen, welche empfindsam auf Ionenbombardement reagieren und damit Detektoren darstellen, wurde demonstriert. Die gleiche Technik wird auch zur Anordnung von NV-Zentren in Diamantsubstraten verwendet. Des weiteren werden einzelne Ioneneinschläge in Siliziumbauteilen erfasst, wodurch das gezielte Dotieren Ion für Ion ermöglicht wird.

# Contents

# Chapter 1

# Introduction

*This chapter gives an introduction and overview for the work presented in this thesis. The motivation for quantum information processing, single ion detection and selected qubit approaches are explained. The conducted research is fit in the overall picture and challenges and approaches to solve those are addressed. A more detailed overview and preview of the presented work follows at the end.*

## 1.1 Motivation

A lot of predictions about the future computational needs of humanity are not confirmed or taken out of context. Most of them are attributed to scientist, computer pioneers or company executives of the early stages of semiconductor and computer development saying that only a very small number of computers would be needed to make all necessary calculations worldwide [1, 2]. Although those persons (most-likely) never said what they are quoted for, there is no doubt that anybody could really foresee the huge success and need of computational power in our everyday lives. 56 years passed since Bardeen, Brattain and Shockley received the Nobel Prize in physics [3] and it has been 58 years since Texas Instruments announced the commercial availability of grown-junction silicon transistors [4–6]. During this period of time more than two billion personal computers were sold; the second billion between the years 2004 and 2007. More than 275 million personal computers were sold alone in 2010 [7, 8] and the demand of computational power of our society is still unsatisfied.This is driven by our constantly growing need for speed and computing capacity for mostly personal entertainment reasons at home but also by industry and research facilities with their need to handle increasing amounts of data. Non of these contributing groups are likely to have stagnating or decreasing needs and

it is estimated that two billion personal computers will be in actual use by 2015 [7, 8].

The semiconductor industry has kept up with this increasing demand for computational power by following Moore's law for more than 40 years [9, 10]. Researchers and scientists managed to circumvent roadblocks and technological obstacles to scale transistors year for year to keep the exponential growth of the semiconductor market alive. They increased the transistor density per microprocessor from 2000 in 1965 to 2.3 billion (45 nm process) in 2010 [4, 11]. Device sizes are getting closer and closer to fundamental physical limits, and it will not be possible to continue the scaling trend of complementary metal-oxide-semiconductor (CMOS) technology forever. In order to sustain CMOS performance gains to and beyond the 16 nm generation, new technologies are assessed and explored to replace the traditional silicon channel devices [12].

Among those candidates for the "beyond CMOS" era are atomic switches, single molecule devices and carbon based electronics [13]. Other prospects are quantum bits (qubits) for quantum information processing. Unless conventional computers, quantum computers operate on entire different principles (a short introduction to quantum computing will be given in chapter 2.1). Instead of using classical bits, qubits are used as the basic building blocks. These building blocks cannot be described by classical physics and quantum mechanics is necessary to fully describe their states. As its classical counterpart, a qubit consists of two base states. The difference is that until the measurement of the qubit's state, which yields one of the base states, it can be in a superposition of both base states. In contrast to that, the bit's state is in either of its base states the entire time. The typical example for a qubit is the electron spin with its associated magnetic moment. Via magnetic fields one can interact with the magnetic moment and determine and manipulate the spin orientation and state of the qubit, similarly to a spinning top or gyroscope and the application of mechanical or gravitational forces. In contrast to classical computers the increase in computational power would not be caused by the scaling down concept itself anymore, but rather by the number of the qubits coupled to each other. A quantum computer would make use of different laws of physics. The application of quantum mechanical principles as superposition and entanglement would lead away from the traditional way computers operate. By employing those quantum mechanical phenomena, a significant increase in computation power can be achieved for certain tasks [14–19] and problems could be addressed and solved that classical computers would face hopelessly [20]. Thus quantum computation has the potential to revolutionize science and technology. The list of proposed qubit candidates is lengthy and consists of e.g. photons,

trapped atoms and ions, nuclear spins in liquid molecules, superconducting qubits, solid state dopants and quantum dots [21]. All of the qubit systems have their advantages but the most promising candidate for a fully functional large scale quantum computing architectures still remains to be determined.

In 1998, Bruce Kane set off the interest in silicon based materials for quantum computing. He proposed to place single donor atoms in a silicon lattice with a spacing of $\approx 20\,\text{nm}$ between each other and below the surface and to use the nuclear spin as a qubit [22,23]. Fig. 1.1 shows a schematic of his concept. Donor atoms are located in a silicon matrix (in blue) and metal gates

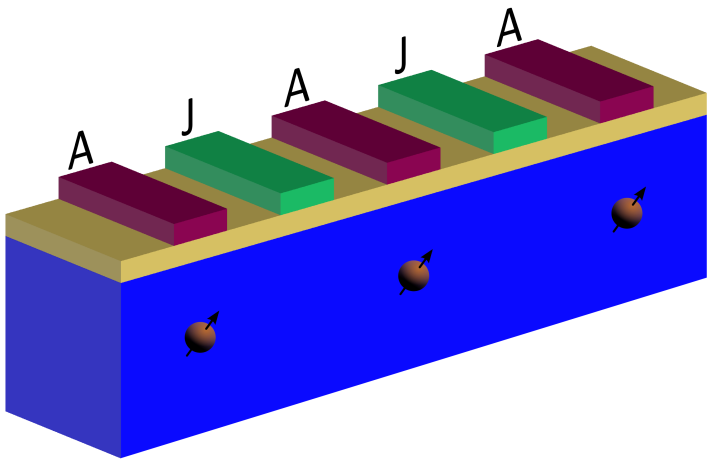


Figure 1.1: Illustration of Kane's quantum computer architecture with donor atoms located in a silicon substrate.

on an insulating silicon dioxide layer act on the donor atoms. Accumulation gates (in purple) pull the electron wave function towards the interface and de-tune the hyperfine coupling between the electron and nucleus of a donor. Thus, individual donor nucleus addressability by a global magnetic field is achieved (single qubit operation). J-Gates (in green) allow two adjacent donor atoms' electron wave functions to overlap and vary the nuclear exchange interaction between them (two qubit operation). Single-electron capacitance techniques are then used to read out the electron position after an electron spin dependent transfer between two neutral donors, revealing the nuclear spin state. Since then, Kane's initial proposal has been modified and various other device layouts and operation mechanisms have been suggested, e.g. use of the electron spin as a qubit too.

Other promising qubit candidates are color centers in diamond. The most well known and studied center is the negatively charged nitrogen-vacancy (NV) center [24–28]. It consists of a substitutional nitrogen atom, a carbon vacancy on a neighboring lattice site in the diamond

matrix and an additional electron. Similar to the phosphorus atom in Kane's proposal, the NV center could form the building block of a quantum computer. Its easy optical access and materials properties makes the NV center not only interesting for quantum information processing, it also finds applications in different fields, such as magnetometry [29, 30], single photon sources [31–33], quantum cryptography [34] and biological process imaging [35] due to the great bio-compatibility of diamond particles.

The donor based quantum computer approach shows that by using a single donor as a qubit, new architectures can be explored and quantum information processing be realized. Even without using a single donor as the functional part of the device itself, individual donors can have an effect on conventional CMOS devices performance [36]. In traditional CMOS technology, dopants are used to modify the device characteristic, e.g. the change of threshold voltage. Over time, the device structures have been scaled down continuously and reached dimensions where a homogeneous doping profile can no longer be assumed. Statistical variations of individual dopant positions become noticeable and can cause fluctuations in electrical characteristics and device performance from device to device [36–43].

If one tries to build qubits with donor atoms in silicon, NV centers in diamond or study effects of single donor on traditional device performance, a good control over the placement process of single donors is needed. The required accuracy can be as small as a few nanometer, depending on the architecture of choice. Thus as good control over single atom placement can help to conduct and explore new science with potential for breath-taking applications.

## 1.2 Status of the Field

The process of accurate single ion placement is a twofold problem. It requires the precise control of the ion placement process and control over the number of dopant atoms. Over the years, a variety of techniques have been developed to address these issues. On the ion placement side, ion implantation tools are the most common way to introduce donor atoms into substrates. Ion implanters are very versatile in terms of implant species and the spatial control can be either achieved with focused ion beam setups or collimation techniques. Standard focused ion beams using gallium or indium ions achieve spot sizes down to 10 nm. Since those ion species are not applicable as donor atoms for the here described purpose, customized focused ion systems need to be build for other species, such as phosphorus or antimony. An aiming precision of on average 60 nm has been achieved and can be further reduced by properly tuning the ion beam optics [39, 44].

The collimation technique can be split into two groups where the collimation apertures are either masks directly fabricated onto the samples or mounted statically or dynamically with a certain distance away from it. For on chip resists and electron beam (ebeam) lithography patterning, apertures of 20 nm in diameter have been combined with sub 20 keV phosphorus implantation [45]. Not until recently and after the here presented work [46, 47], dynamically mounted apertures (100 nm by 10 µm long slots) on a scanned nano-aperture apparatus in combination with on chip ebeam resist apertures were used and impacts of 500 keV helium ions detected [48]. A special case for the latter approach is the use of SPM cantilevers with incorporated apertures as it is used here in this work. This technique which also constitutes a dynamic aperture mask was developed in this group at LBNL a few years ago and the high resolution imaging capability of the SPM is used to place the ion beam on the sample [49,50]. A sketch for better visualization of the idea behind this technique can be seen in Fig. 6.1. Patterns in photoresist next to alignment marks were demonstrated with aperture sizes of 100 nm and 90 nm but without in-situ feedback control of the ion beam position [51, 52]. Apertures in cantilevers down to $\approx 5$ nm and 30 nm have been achieved and could be used for the implant work [53, 54].

The spatial placement control needs to be combined with the ability to detect single ion impact (SII) events. This can be done via the detection of released secondary electrons [44, 55, 56] or the collection of electron hole pairs at low temperatures [45, 57–59]. For reasons explained in chapter 7.2, here SII are detected via the changes in device currents [60] which was later on demonstrated by other groups too [61, 62].

A combination of ion placement and ion counting techniques are the following two approaches. The first one is the absorption of single phosphene molecules on hydrogen passivated silicon surfaces [63, 64]. A scanning tunneling microscope is used to remove individual hydrogen atoms from the surface to open up silicon sites intended for doping via the incorporation of the phospene's phosphorus atom. This technique has only been demonstrated for the Si:P system so far but allows shallow doping down to the atomic scale.
The second approach is a deterministic ultracold ion source [65–67]. Single ions can be loaded and cooled down in an ion trap and then ejected onto the sample. Up to now, only $Ca^+$ ions at a kinetic energy of 80 eV with a spot size of a few micrometers have been achieved but simulations predict ion beam spot sizes around one nanometer.

Nitrogen ion implantation has become a common technique to form NV centers. Focused high and low energetic ion beams have been used to create these color centers [54, 68–77]. In order to form NV center arrays, the implantation process of low kinetic nitrogen ions was also combined with on-chip apertures down to 30 nm [69,70] and with dynamic nano apertures [78] after our proof of principle demonstration with µm sized implant spots at LBNL [46]. Recent application of stimulated emission depletion (STED) fluorescence microscopy [79] to NV centers in diamond [78, 80] allows the study of the NV center placement accuracy with a few nm and well below the conventional diffraction limit of optical microscope systems.

## 1.3 Aim and Outline of the Thesis

The majority of the work presented here is part of a larger silicon base quantum computing effort with the goal to demonstrate device fabrication, precise single ion implant capabilities, coherent manipulation and spin state readout. Thus, all experiments are designed to be compatible with the overall effort of this project. The devices used for implantation demonstration and single ion detection are also used to explore (single) spin state readout via electrically detected magnetic resonance (see Fig. 1.2) [81, 82]. An electron current is passed by the donor atom and via spin dependent processes, such as neutral donor scattering, recombination via defect centers at the interface or trapping mechanisms, a change in the device current is observed which correlates to the spin state of the donor.

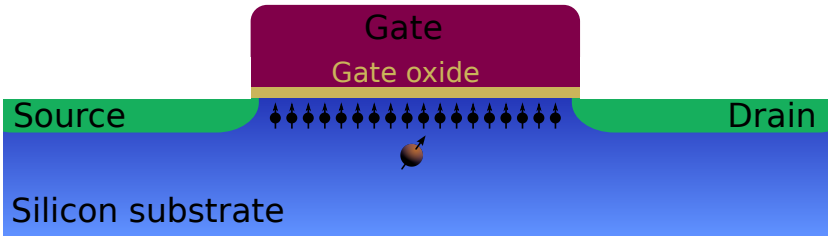


Figure 1.2: Field effect transistor with one donor atom in the channel region. An ideally fully spin polarized electron current interacts with the donor spin, resulting in a change in the device current and revealing the donor spin state.

### Aim

In this thesis the following challenges of both outlined qubit approaches will be addressed:

- Scanning probe microscopy setup improvements for reduced tip wear and improved implant precision.
- Implementation of a metal ion beam creation technique for optimized implantation procedures.
- Integration of SPM tips, ion beams and electrical device structures, demonstrating the imaging and precise ion implantation capabilities of this technique into predefined device structures for the first time.
- Single impact detection of ions low in kinetic energy ($< 70\,\mathrm{keV}$) in silicon structures via changes in device currents at room-temperature.
- Formation of NV center arrays for the study of NV center qualities via optically detected magnetic resonance (ODMR) experiments.

## Outline

Each chapter addresses a certain topic of the presented work. A short introduction is given at the beginning of each chapter which fits in the respective issue into the overall picture. Further a list of relevant publications that was contributed to can be found there.

Here a list with the chapter overviews:

Chapter 2 gives a brief background about the work of this thesis, including details about the used qubit candidates, scanning probe microscopy and ion interaction with matter.

Chapter 3 gives an overview of the ion beamline setup used for the presented implantation work, including some of the upgrades improving its capabilities.

Chapter 4 describes the SPM setup used for the presented work, including all the upgrades and modifications made to the formerly existing system.

In chapter 5 the development of a new ion source setup for low charge state metal ions is discussed. It functions as a complementary source to the electron beam ion trap (EBIT) with the advantages of a more convenient and cheaper running procedure.

Chapter 6 describes the first integration of SPM tips, ion beams and electrical device structures and the controlled alignment of the ion beam to a defined surface feature. Ion beam induced changes in the source drain currents of field effect transistors are recorded versus SPM tip and ion beam position.

Chapter 7 demonstrates the detection of single ion impacts in silicon FETs and silicon wires at room-temperature via changes in device currents. The device sizes range from a couple of micrometers to sub-micrometers. This validates the detection method and allows its application to devices with potential single spin readout capability.

Chapter 8 addresses the formation of few NV center arrays. Nitrogen ions are implanted through dynamic shadow masks (SPM cantilever) into diamond samples. Upon sample annealing the formed NV center arrays are examined by photoluminescence microscopy. Preliminary results on nitrogen channeling effects during ion implantation and work on an ion detection technique similar to chapter 7 are presented.

# Chapter 2

# Background

*This chapter gives a brief background about the work of this thesis, including details about the used qubit candidates, scanning probe microscopy and ion interaction with matter.*

## 2.1 Quantum Computing

### Overview[1]

As mentioned earlier, quantum computing has the potential to revolutionize information processing. Using transistors and switches for Boolean logic, the way computers work has been the same for years. The progressive increase in speed and power has been based on making the building blocks of classical computers smaller and smaller. With quantum computers a completely different working principle would be employed. Quantum mechanical phenomena as superposition and entanglement would be used to run quantum algorithms capable of solving problems in a much more efficient and faster way.

A conventional computer uses bits. Each bit can exist in two states, 0 or 1. The memory or the state of a classical computer can be described in $n$ bits. There are $2^n$ possible permutations of those $n$ bits. To describe the actual present state, one of those $2^n$ possible permutations is enough. It consists of a list of $n$ values, 0 or 1 each. If one changes the value of one of those $n$ bits by a gate operation during the operation of the classical computer, the list stays the same, except for the flipped bit.

[1]The citing is neglected in this section. The reader is referred to [83–85] as sources.

A quantum computer consists of quantum bits (qubits) instead of bits. Instead of discrete values each qubit can exist in any superposition of two states.

$$\alpha_1 |0\rangle + \alpha_2 |1\rangle \tag{2.1}$$

To describe a single qubit, both values $\alpha_1$ and $\alpha_2$ are needed. In order to describe the full quantum state of $n$ qubits, $2^n$ parameters are needed. For $n$ classical bits, $n$ parameters were enough to describe the one state (out of $2^n$ possibilities) that was present. In contrast to that, the quantum state needs the full set of $2^n$ parameters for its full description of superposition. The quantum state needs more parameter to be described properly, but can also store more information.

As classical algorithms, quantum algorithms use gate operations, so called quantum gate operations. It is interesting to note that a quantum gate operation on one qubit can change the entire system and all the $2^n$ parameters necessary to describe its state. In the case of a classical register, only one bit and thus only one of the $n$ parameters to describe the state changes. The Hadamard gate operation is a single qubit operation and acts on one qubit only. For a single qubit the Hadamard operation changes the initial states as follows:

$$|0\rangle \xrightarrow{H} \frac{1}{\sqrt{2}}(|0\rangle + |1\rangle) \tag{2.2}$$

$$|1\rangle \xrightarrow{H} \frac{1}{\sqrt{2}}(|0\rangle - |1\rangle) \tag{2.3}$$

The Hadamard gate puts the initial states $|0\rangle$ and $|1\rangle$ into superposition. Thus if the initial state is $\alpha_1 |0\rangle + \alpha_2 |1\rangle$, the outcome is as follows:

$$\alpha_1 |0\rangle + \alpha_2 |1\rangle \xrightarrow{H} \frac{\alpha_1}{\sqrt{2}}(|0\rangle + |1\rangle) + \frac{\alpha_2}{\sqrt{2}}(|0\rangle - |1\rangle) \tag{2.4}$$

$$= \frac{1}{\sqrt{2}}(\alpha_1 + \alpha_2) |0\rangle + \frac{1}{\sqrt{2}}(\alpha_1 - \alpha_2) |1\rangle \tag{2.5}$$

$$= \beta_1 |0\rangle + \beta_2 |1\rangle \tag{2.6}$$

It is intuitive that applying the Hadamard gate operation on a single qubit changes both parameters ($\alpha_1$ & $\alpha_2 \rightarrow \beta_1$ & $\beta_2$). A state of two qubits can be described as follows:

$$\alpha_1 |00\rangle + \alpha_2 |01\rangle + \alpha_3 |10\rangle + \alpha_4 |11\rangle \tag{2.7}$$

Here $|01\rangle$ means that the first qubit is in state $|0\rangle$ and the second in state $|1\rangle$. Applying the Hadamard gate operation on the first qubit only will result in a change of all parameters as

follows:

$$\frac{1}{\sqrt{2}}(\alpha_1 + \alpha_3)\,|00\rangle + \frac{1}{\sqrt{2}}(\alpha_2 + \alpha_4)\,|01\rangle + \frac{1}{\sqrt{2}}(\alpha_1 - \alpha_3)\,|10\rangle + \frac{1}{\sqrt{2}}(\alpha_2 - \alpha_4)\,|11\rangle \tag{2.8}$$

$$= \beta_1\,|00\rangle + \beta_2\,|01\rangle + \beta_3\,|10\rangle + \beta_4\,|11\rangle \tag{2.9}$$

In contrast to the classical case, the application of the gate operation to the quantum state changes the full set of parameter which is necessary for its description.

Another non-classical phenomena is entanglement. If two qubits are entangled they are connected, regardless of the distance in between them. The measurements of their states is not independent of each other anymore. For a two qubit system, an entangled state can be produced by a Hadamard gate operation on the first qubit followed by a CNOT gate operation with the first qubit being the control qubit. If both quits are initialized to $|0\rangle$, the initial state is $|00\rangle$. As can be seen from equation 2.8, the Hadamard gate operation turns the state into $\frac{1}{\sqrt{2}}(|00\rangle + |10\rangle)$. This is still an unentangled state. If one measures the first qubit the chance for measuring $|0\rangle$ is 50 % as it is for $|1\rangle$. Independent from that the measurement of the second qubit will always yield $|0\rangle$. On the other hand, measuring the second qubit first will always yield $|0\rangle$, the following measurement of the first qubit has a 50 % chance to result in $|0\rangle$ and 50 % chance for $|1\rangle$. The outcome of the first measurement of either qubit neither influences the second measurement nor helps to determine the outcome of the second one. This behavior changes after applying a CNOT operation on the quantum state, which brings it into an entangled state. The CNOT quantum gate operation is a two (or multi-qubit) operation that will perform the NOT operation on the second qubit only if the first qubit is $|1\rangle$.

$$\begin{pmatrix} 1 & 0 & 0 & 0 \\ 0 & 1 & 0 & 0 \\ 0 & 0 & 0 & 1 \\ 0 & 0 & 1 & 0 \end{pmatrix} \begin{pmatrix} \frac{1}{\sqrt{2}} \\ 0 \\ \frac{1}{\sqrt{2}} \\ 0 \end{pmatrix} = \begin{pmatrix} \frac{1}{\sqrt{2}} \\ 0 \\ 0 \\ \frac{1}{\sqrt{2}} \end{pmatrix} \tag{2.10}$$

The whole sequence of gate operations starting with the $|00\rangle$ state looks as follows:

$$|00\rangle \xrightarrow{H} \frac{1}{\sqrt{2}}(|00\rangle + |10\rangle) \xrightarrow{CNOT} \frac{1}{\sqrt{2}}(|00\rangle + |11\rangle) \tag{2.11}$$

The final result is an entangled state of the quantum register. Now, measurements on the two qubits are not independent of each other anymore. The chance for measuring $|0\rangle$ or $|1\rangle$

on the first qubit (it doesn't matter which one is measured first) is still 50 %. However, the measurement of the second qubit will always result in the same value. Without measuring the second qubit, its value can still be determined and is predefined by measuring the first qubit. This even holds true if the two qubits are separated after they are put into the entangled state. If one measures the first qubit at a location A, one already knows what the measurement of the second qubit at location B will yield. Similarly, one can create entangled states where the outcome of both qubit measurements will result in opposite states.

This trivial example of a two qubit system shows the huge potential of multi-qubit systems. The complexity of the quantum system increases rapidly with the addition of qubits. Whereas 10 parameters are enough to describe a 10 bit register, 1024 are necessary for a 10 qubit register. For 20 qubit this number of parameters rises to over 1 million, for 31 qubits the number equals nowadays transistor densities of microprocessors and in the case of 200 qubits the number exceeds the number of atoms that our planet is made out of. Adding a single qubit one at a time makes the system just more and more powerful. Combined with the fact that a single qubit operation can affect the entire quantum system no matter of its size, one easily understands the new possibilities that the use of quantum mechanical phenomena for information processing can offer.

### Quantum algorithms

By the use of the just described quantum mechanical phenomena powerful quantum algorithms can be written that solve certain problems in a much shorter period of time compared to classical algorithms. In 1982, Richard Feynman stated that in order to simulate quantum systems efficiently, the computing device would need to make use of quantum mechanics [86]. But it was David Deutsch with his publication in 1985 [87] who is seen as founder of the field of quantum computation. Together with Richard Jozsa he introduced the first quantum algorithm to solve a problem faster than a classical computer. However, the algorithm has little practical application. Two years later Peter Shor proposed an algorithm to efficiently factorize integer numbers [16, 17]. In 1995, Lov Grover introduced the unsorted database search algorithm (quantum search algorithm) [18, 19]. Both algorithms are considered the most famous and useful examples for quantum algorithms which would affect process optimization and RSA public-key cryptography for instance.

Quantum algorithms have already been compiled and demonstrated to work on real systems. As examples, the Deutsch-Jozsa algorithm was performed on a single NV center [88], liquid-state nuclear magnetic resonance (NMR) with seven spin-$\frac{1}{2}$ nuclei molecules [89] and photonic qubits [90, 91] were used to demonstrate Shor's algorithm to factor the number 15.

For a quantum computation system to be really useful, more qubits need to be combined and entangled. However, the demonstration of small computational tasks are steps into the right direction. This also shows that there are requirements a quantum computation systems needs to fulfill to become really successful and live up to its potential.

### DiVincenzo criteria

In 2000, David DiVincenzo compiled a list of criteria that any physical implementation of a quantum computer needs to fulfill [92]. The list consists of five criteria for the quantum

| | |
|---|---|
| 1. | A scalable physical system with well characterized qubits. |
| 2. | The ability to initialize the state of the qubits to a simple fiducial state, such as $\|000...\rangle$. |
| 3. | Long relevant decoherence times, much longer than the gate operation time. |
| 4. | A "universal" set of quantum gates. |
| 5. | A qubit-specific measurement capability. |
| *6.* | *The ability to interconvert stationary and flying qubits.* |
| *7.* | *The ability to faithfully transmit flying qubits between specified locations.* |

Table 2.1: DiVincenzo's original criteria for the physical implementation of a quantum computer.

computer itself and two for data processing and communication & networking. The original list has been extended by other criteria, which are usually referred to as "Beyond DiVincenzo Criteria". They address further elements like qubit coherence issues, fault-tolerancy and error-correction necessity [93–95]. For any qubit approach to be successful a long list of demands needs to be fulfilled. Any of the proposed candidates shine in certain areas and face challenges in other areas that need to be overcome.

## 2.2 Scanning Probe Microscopy

Scanning probe microscopy (SPM) has its origins in the early 1980s when Binnig and Rohrer invented the first scanning tunneling microscope (STM) [96]. For their work they were awarded the Nobel Prize in physics in 1986 [97]. Since then numerous variations of this technique have been developed. Among those but not limited to them are scanning capacitance microscopy [98], kelvin probe force microscopy [99] and near field scanning optical microscopy [100]. These methods enable the study of surface topography, local density of states, surface potential, workfunction, optical properties and far more down to the atomic scale and have become integral tools in science.

One offspring of the STM is the atomic force microscope (AFM) which was developed in 1986 [101]. It combines the principles of a STM and a stylus profilometer. A small cantilever with a sharp tip is brought into contact with a sample and then moved across the sample surface. The deflection of the cantilever caused by sample topography and surface roughness is then detected. The deflection of the cantilever is usually measured by shining a laser onto the topside of the cantilever which has a reflective finish. A four quadrant photo detector is then used to measure the position of the laser which is deflected off of the cantilever accordingly to its motion (deflection & torsion). A scanning probe microscopy system can be operated in two ways, open-loop and closed-loop. During open-loop operation the cantilever is moved along the surface and the deflection is recorded. The signal from the photo diode can then be used to extract the topography of the sample. Due to the stiffness of the tip, high contact forces can occur depending on the topography and roughness of the sample. It is even possible to crash the tip into objects and lose scanning resolution due to bluntness of the tip. In case of closed-loop operation, the piezo scanner corrects the distance of the tip to the sample, so that the deflection of the cantilever is kept constant at a certain value. That way a small contact force can be achieved during the entire data acquisition. In this mode the topography information is obtained from the piezo movement in $z$-direction.

The traditional way of AFM operation is to bring the tip into contact with the sample. If one wants to obtain information about friction qualities of the surface this is actually essential. However, it is also possible to actuate the cantilever so that it constantly oscillates. Upon approach to the sample surface a change in oscillation amplitude, frequency and phase occurs which is caused by the cantilever interaction with the surface. In vacuum van-der-Waals forces can increase the oscillation amplitude whereas in air a damping effect due to the viscosity of the air cushion between the cantilever body and sample can be observed. If

the cantilever is approached further, the oscillation amplitude is reduced due to tip impacts with the sample surface. The changes in the oscillation parameters can be used as a source signal for closed-loop feedback operation, keeping either amplitude, frequency or phase shift constant. Depending on the cantilever distance from the sample surface during oscillation, the AFM system can be operated in hard-tapping, soft-tapping or non-contact mode. In latter case, tip wear can be prevented and continuous high resolution imaging enabled.

### Contact AFM Basics

Is the AFM operated in closed-loop contact mode, the tip touches the sample and a constant force is applied during the scanning motion. The cantilever acts as a spring with spring constant $k$ and presses the tip onto the sample with a force $F$ depending on the position of the cantilever base $\Delta z$ in respect to the sample. The position where the cantilever is in its natural unbent state determines $\Delta z = 0$. The force can be calculated according to Hooke's law $F = k\Delta z$. Commercial AFM tips often come with calibrated spring constant values for each individual tip, but there exist certain methods a tip's spring constant can be determined.

Following Cleveland *et al.* [102], one can obtain the spring constant of a rectangular cantilever with the knowledge of its length $l$, width $w$, thickness $t$, Young's modulus $E$, density $\rho$ and resonance frequency $f_0$.

$$k = \frac{Et^3w}{4l^3} = 2\pi^3 l^3 w f_0^3 \sqrt{\frac{\rho^3}{E}} \tag{2.12}$$

Sader's method [103] for rectangular cantilevers (with $l \gg w \gg t$ and $Q_f \gg 1$) suggests,

$$k = 0.1906\rho_f w^2 l Q_f \Gamma_i(\omega_f)\omega_f^2 \tag{2.13}$$

with density and viscosity of the surrounding medium/fluid $\rho_f$ & $\eta$, radial resonance frequency $\omega_f$ and quality factor $Q_f$ of the fundamental mode of the cantilever in the fluid and $\Gamma_i$ being the imaginary component of the hydrodynamic function. Values for the latter only depend on the Reynolds number $Re = \rho_f \omega w^2/4\eta$ and are listed in [103] as well.

The spring constant can also be determined by using the thermal tune method [104, 105] which is derived from the equipartition theorem and yields:

$$k = 0.817\frac{k_B T \cos^2\alpha}{\langle z_c^{*2}\rangle} \tag{2.14}$$

$k_B$ denotes the Boltzmann constant, $T$ the absolute temperature, $\langle z_c^{*2}\rangle$ the mean squared displacement of the cantilever's thermal motion as measured by the optical readout of the cantilever mounted under angle $\alpha$ to the sample.

Another trickier experimental option to determine the spring constant is to bring an unknown cantilever in contact with a well calibrated cantilever, e.g. backside to backside. From the ratio of both cantilever's deflections measured under a microscope, the unknown spring constant can be derived $k = k_{ref} \frac{\Delta z_{ref}}{\Delta z}$.

In order to find the cantilever position for $\Delta z = 0$, one can take a force-distance (FD) curve. During a FD-curve the AFM tip and sample are approached to each other, brought into contact and then separated from each other again. Thus, a FD-curve consists of two traces; an approach and a retract trace as can be seen in Fig. 2.1 on the right hand side. The

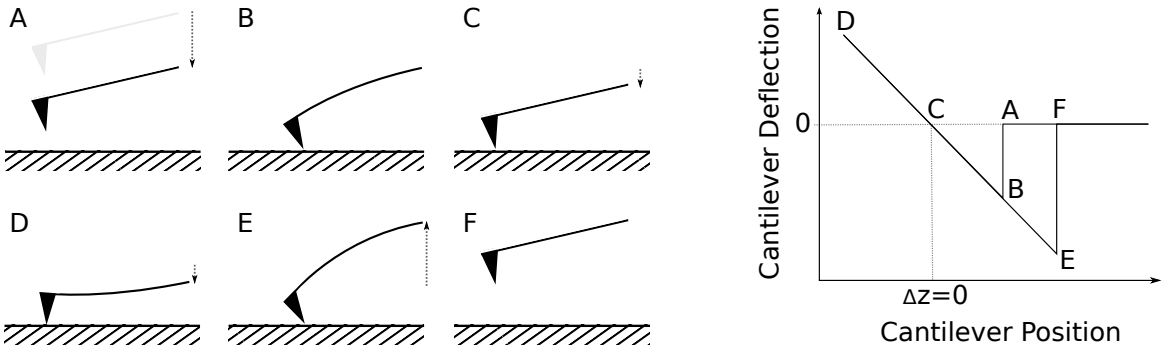


Figure 2.1: Force distance curve (right) and the respective cantilever motion during the acquisition of a force-distance curve (left).

tip and sample are brought into proximity up to a point (point A) where the tip is suddenly pulled towards the surface into contact (B). This is caused by near range forces, e.g. van-der-Waal forces, or water bridge formation if operated in moist environment. After that, the cantilever base is approached further and one follows the linear spring regime where the tip bends more and more upwards all to point (D), passing the unbent state of the cantilever (C). After starting the sample retraction process one follows again the linear curve to the point where the cantilever is not flexed anymore. At that point the cantilever does not immediately leave the surface since the tip is held in contact by adhesion forces. At the point where the force of the bent cantilever is slightly larger than the adhesion force the cantilever snaps off of the sample surface (E→F) and flexes back into its unbent state. Depending on the tip surface interaction and sensitivity of the AFM system, the snap into contact and pull of point are not observed during FD-curve acquisition. The signal dip in the cantilever retract trace in the FD-curve is usually more pronounced than the snap into contact dip. This is due to the stronger adhesion forces acting on the tip and keeping it in contact with the sample than the short range forces that pull the tip into contact.

With the knowledge of $k$ and $\Delta z$ the applied force by the cantilever can now be determined and the cantilever deflection signal on the $y$-axis (e.g. signal from photo diode) be converted to an actual force. The usual regime of contact mode operation is where the cantilever is bent through and applies a force onto the sample via the tip. It is also possible to have the cantilever apply a force away from the surface and have the tip kept in contact by the greater adhesion forces only. However, in practice this is an unstable way of running the system. Due to variations of the adhesion forces and the scanning motion itself, there is always a given chance that the cantilever snaps out of contact.

In order to obtain good image qualities, a low noise system is essential. The image resolution in $z$-direction can be determined relatively easy. Scanning the tip across atomically flat surfaces like highly ordered pyrolytic graphite (HOPG), MICA (silicate (phyllosilicate) minerals) or single crystal silicon samples will yield the $z$-resolution or an upper bound. Another way is to bring the tip into contact with the sample and take a Fourier transform (noise power spectrum) of the deflection signal. Integration of the noise power spectrum across the contributing frequency bandwidth will yield a noise deflection value which can be converted into length scale with the slope information form the FD-curve (cantilever deflection vs. cantilever-sample position). This value then represents the to be expected noise level in $z$-direction of the AFM system and the vertical resolution can be better than 0.1 nm [106, 107]. Obtaining values for the lateral resolution is harder and usually not dominated by noise sources. The obtained topography information is a convolution of the actual surface features and the tip shape, usually with a tip radius of tens of nm. Unless ultra sharp tips with small tip radii are used, the convolution issue dominates the noise contributions. This especially holds true for identifying small indentations or trenches rather than features extending form the sample surface. For the latter case it yields a broader structure only, but in the former case the features may not be detected at all.

### Piezoresistive SPM Cantilevers

As mentioned before, the traditional way to measure the cantilever deflection is by reflecting a laser off of the cantilever's backside and tracking the laser movement with a photo-diode. However the deflection of the cantilever can also be tracked by detecting the mechanical stress induced in the cantilever body with equal resolution limits [106, 107].

This can be done by using piezo-resistive materials that are embedded in the cantilever. The maximum mechanical stress appears at the cantilever support point. This is the desired location for the piezo-resistive elements which change in resistivity upon mechanical stressing due to the cantilever deflection. Implementation of full Wheatstone bridge arrangements at the cantilever base have been achieved by Rangelow *et al.* [106, 108, 109]. The tips used here are provided by the same group and an optical image of a tip can be seen in Fig. 2.2. The fabrication of the cantilevers and the Wheatstone bridge can be done with standard CMOS processing. The use of piezo-resistive AFM systems saves the laser alignment and is advantageous for compact designs.

Figure 2.2: Optical image of one of the piezo-resistive cantilevers used in this work.

## 2.3 Ion Interaction with Matter [1]

Ion interactions with solids are manifold and a lot of different processes occur. After a charged ion hits the surface of a solid and then travels deeper into the substrate material, secondary electrons, X-rays, recoil atoms and defect centers are produced and other processes take place. Over the years, scientist learned how to interpret the data, make use of the various ion interaction processes and extract information about thin films and sample substrates. One of the first and most famous experiments is Rutherford's gold foil experiment [114,115]. In 1909, he supervised an experiment conducted by H. Geiger and E. Marsden where they observed a considerable amount of backscattered $\alpha$-particles. Two years later this lead to the revision of the, at that time, accepted "plum-pudding model" by J. Thomson and the introduction of the Rutherford model, stating that most of the atoms mass and all positive charge is concentrated to a small volume and centered within the atom surrounded by electrons. Among those techniques developed over time, but not limited to them, are secondary ion mass spectroscopy (SIMS), Rutherford back scattering (RBS), particle induced X-ray emission (PIXE), elastic backscattering spectroscopy (EBS), hydrogen forward scattering spectrometry (HFS), nuclear

[1] The citing is partially neglected in this section. The reader is referred to [85, 110–113] as sources.

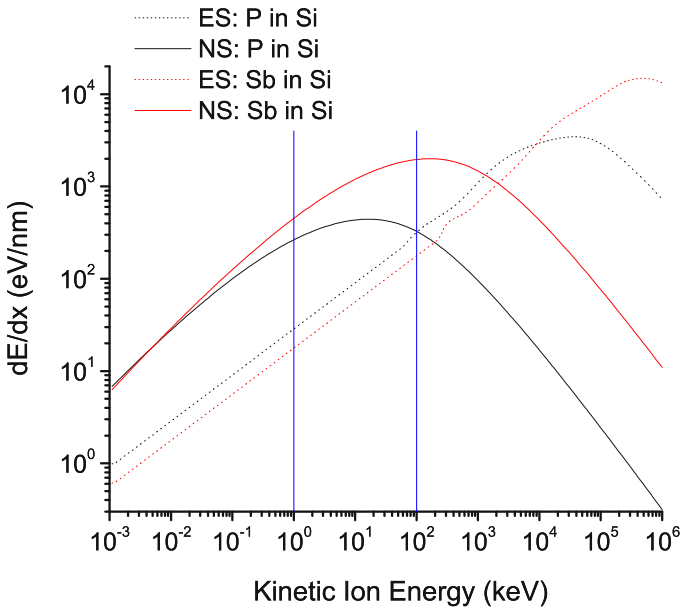


Figure 2.3: Electronic (ES) and nuclear stopping (NS) versus kinetic ion energy for phosphorus and antimony ions into silicon (SRIM simulation [116]). The blue lines roughly mark the ion energy interval applicable to this work and shallow donor implantation.

reaction analysis (NRA) and elastic recoil detection (ERD). Ion beams have become versatile and powerful analysis tools in science and industry and are also utilized for ion implantation, sputtering or ion milling.

### Energy Transfer

When an ion hits the atoms of a solid target material, it loses its kinetic energy via various processes, namely nuclear and electronic collisions. During nuclear collisions, the ion transfers its energy via elastic scatter events to the nucleus of a target atom due to their repulsive potential. Electronic stopping slows down the ion due to the interaction of the bound target electrons with the charged ion moving through the target. Fig. 2.3 shows the contributions for the electronic and nuclear stopping for two donors (phosphorus and antimony) in silicon. Both electronic and nuclear stopping contributions have a local maximum for a certain kinetic ion energy, with the nuclear stopping maximum occurring at much lower energies. For the ion energy applicable to this work and precise doping of silicon structures, nuclear stopping is the main energy loss process. For implants with higher kinetic ion energy, electronic stopping dominates the beginning and nuclear stopping the end of the ion trajectory.

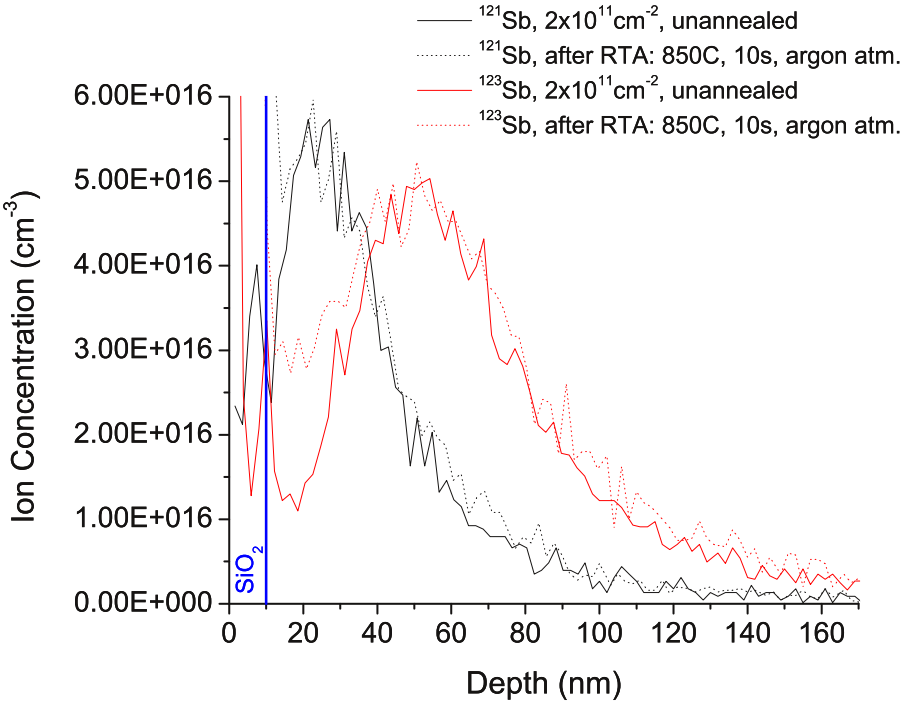


Figure 2.4: Secondary ion mass spectroscopy measurements showing the longitudinal species profile of implanted 60 keV $^{121}$Sb and 120 keV $^{123}$Sb ions into a $^{28}$Si sample with a 10 nm oxide on top. Dotted lines show the species profiles after a rapid thermal annealing step at 850 °C for 10 s in argon atmosphere.

The energy loss of the ion per unit distance is $\frac{dE}{dx}$. Thus the lost energy $\Delta E$ per traveled distance $\Delta x$ is $|\Delta E| = \frac{dE}{dx}\Delta x$. Since $\Delta E$ is proportional to the target atom density $N$, the convention is to define a density independent proportionality coefficient $S(E)$ called stopping power.

$$\Delta E = S(E)N\Delta x \quad \text{with} \quad S(E) = -\frac{1}{N}\frac{dE}{dx} \tag{2.15}$$

The total energy loss per ion is the sum of the electronic and nuclear contributions:

$$\frac{dE}{dx} = (\frac{dE}{dx})_e + (\frac{dE}{dx})_n = -N(S_e(E) + S_n(E)) \tag{2.16}$$

The traveled distance by an ion with initial kinetic energy $E_0$ then can be calculated according to:

$$R(E_0) = -\frac{1}{N}\int_{E_0}^{0} \frac{dE}{S_e(E) + S_n(E)} \tag{2.17}$$

However, this total traveled distance is not the depth that the ion comes to rest. Due to scatter events, the ion changes direction various times on its path through the solid. Unfortunately, a complete analytical description of the processes is not straight forward. Various binary collision approximation (BCA) methods have been implemented via Monte-Carlo models, in which the ion undergoes independent nuclear collisions. After each collision the ion changes direction, is assumed to travel on a straight path on which it loses further energy due to electronic stopping events until it interacts with the next nucleus. A commonly used BCA code is the Stopping Range of Ions in Matter (SRIM) code [85,116–118] which is available for free. Despite certain limitations as the lack of single crystalline target materials, which are implemented in other codes [119–122], it gives good estimates of the to be expected implant profile. An example for the resulting ion depth profile due to the energy transfer from the ion to the solid can be seen in Fig. 2.4. It shows the longitudinal depth distribution of implanted antimony ions before and after rapid thermal annealing. The data was acquired by secondary ion mass spectroscopy (SIMS) measurements which were done by Evans Analytical Group LLC [123]. The ion distributions and differences in implantation depths depending on the kinetic energies are clearly visible. No significant diffusion occurred during the annealing step. Electron spin resonance measurements on these implanted donors showed a $T_2$ lifetime of 0.5 ms at 5 K [124].

### Ion Range Parameters

A common way to describe experimentally obtained or simulated implant profiles is via certain definitions and moments. The most relevant parameters are defined on the next page. They are calculated for $N$ ions hitting the surface at $x = y = z = 0$ and ending up at coordinates $x_i, y_i$ and $z_i$. The $x$-direction is oriented along the surface normal and the $y$- & $z$-direction lie in the surface plane. The mean projected range and radial range denote the average implant depth and ion distance from the $x$-axis, respectively. The longitudinal and radial straggling are the standard deviation (square root of the variance) of the projected and radial range. In case of a normal distributed curve, 68.3 % of the ions would lie within the $\pm\sigma$ interval. The skewness and kurtosis are the 3rd and 4th standardized moment of the projected range distribution. The kurtosis describes the peakedness of the profile, with a larger number meaning a pointier peak. The skewness provides information about the asymmetry of the projected range distribution. Negative values mean a more pronounced tail with the median and mean projected range values at smaller depth values than the mode (peak maximum

position). For a positive kurtosis all the mentioned values lie at greater depth than the mode.

$$\text{Mean Projected Range:} \quad R_p = \langle x \rangle = \frac{1}{N} \sum_i^N x_i \tag{2.18}$$

$$\text{Radial Range:} \quad R_r = \langle r \rangle = \frac{1}{N} \sum_i^N \sqrt{y_i^2 + z_i^2} \tag{2.19}$$

$$\text{Longitudinal Straggling:} \quad \sigma = \sqrt{\langle (\Delta x_i)^2 \rangle} = \sqrt{\frac{1}{N} \sum_i^N (x_i^2) - R_p^2} \tag{2.20}$$

$$\text{Radial Straggling:} \quad \sigma_r = \sqrt{\langle (\Delta r_i)^2 \rangle} = \sqrt{\frac{1}{N} \sum_i^N (y_i^2 + z_i^2) - R_r^2} \tag{2.21}$$

$$\text{Skewness:} \quad \gamma = \frac{\langle (\Delta x_i)^3 \rangle}{\langle (\Delta x_i)^2 \rangle^{\frac{3}{2}}} = \frac{1}{N\sigma^3} \sum_i^N (x_i - R_p)^3 \tag{2.22}$$

$$\text{Kurtosis:} \quad \beta = \frac{\langle (\Delta x_i)^4 \rangle}{\langle (\Delta x_i)^2 \rangle^2} = \frac{1}{N\sigma^4} \sum_i^N (x_i - R_p)^4 \tag{2.23}$$

### Ion Channeling

Ion channeling is an effect that occurs in single crystalline target materials. Due to its highly ordered structure, there are crystal orientations for which lattice atoms are in line of sight of each other. Common examples are the silicon crystal structure when looked at along the (100) or (110) axis. Then the impinging ion does not interact with a randomly distributed target atom distribution anymore. Instead the target material appears as columns of atoms and spaces in between them. Ions can travel along those ”hollow channels” far deeper than usual, due to decreased scatter interactions with target nuclei. For an ion to undergo channeling events, it needs to be within a certain angle to the highly oriented crystal axis. Further this effect depends on the ion energy as well as ion and target materials. Since ions can already change directions considerably during the first scatter events within the first atomic layers at the surface, only parts of the impinging ions channel along the crystalline target material. On the other side, ions can be scattered into channel directions later on after the first scatter events as well. Overall, this effect leads to a second peak in the implant profile at a greater depth of the ions undergoing ”random” scattering events. This effect needs to be taken into account during ion implantation for single crystal materials, as e.g. for silicon where ion implantation under 7° is a common technique to reduce ion channeling. Further, ion channeling plays a large role during the evaluation of RBS data of crystalline material where the back-scattered ion yield is reduced during channeling conditions.

### Defect Creation

While the ion travels through the substrate and deposits its ion energy to the lattice various defects can be generated. Vacancy sites can occur when enough energy is transferred via nucleus-nucleus collisions to overcome the lattice binding energy. This defect can either relax immediately or persist with the target atom ending up on an interstitial lattice position. A threshold concentration of created vacancies can be reached, where the formerly crystalline target material can not be considered as such anymore and amorphization occurs. It is even possible that enough energy and momentum are transferred so that the lattice atom gets scattered forward with high enough energy to set of collision cascades. The target atom then travels through the target material itself undergoing the same energy relaxation processes as the incident ion. Such cascades can cause material intermixing and can lead to backscattered target atoms that leave the substrate if its energy is larger than the surface binding energy (sputtering). This phenomena is used in FIB systems to remove target material or in SIMS to analyze its composition. Similarly, it is possible to transfer enough energy to target electrons enabling them to leave the material as well (secondary electrons). If inner shell electrons are removed, the relaxation process can be either accompanied by auger electrons or x-ray emission.

### Highly Charged Ions

A special case are (slow) highly and multiply charged ions (HCI) [125]. The potential energy associated with low charged ions (1+, 2+, ...) is small itself and also small compared to its kinetic energy, as it is the case for the ions used in this work, including $^{121}Sb^{14+}$ used in chapter 7 ($E_{pot} = 1.9\,keV$). The potential energy is a result of the accumulated ionization energies for the $q$ electrons that are missing to form a neutral atom. The ionization energies for the first electron of a neutral atom is usually a few eV, but reaches thousands of eV for higher charge states and the removal of an additional electron. Thus the accumulated ionization energies can reach a few keV for HCI, e.g. $\approx$ 202 keV for $Xe^{54+}$. As a result, interactions with surfaces and matter are very different and the deposition of the potential energy has a greater effect than the kinetic ion energy contribution. Electrons are captured from the surface to the ion before ion impact and increased secondary electron and ion emissions or the emission of charged clusters observed.

## 2.4 Ion Arrival Statistics

During the single ion impact detection experiments, ions at a fixed average rate hit the sample. Thus their impact statistics follows a Poissonian distribution which needs to be considered when analyzing changes in device currents and evaluating their origin. The Poisson distribution $\mathrm{P}_\lambda(n)$ is a discrete probability distribution ($n \in \mathbb{N}_0, \lambda \in \mathbb{R}_{>0}$) and can be derived from the binomial distribution.

$$\mathrm{P}_\lambda(n) = \frac{\lambda^n}{n!} e^{-\lambda} \tag{2.24}$$

It describes the probability of the expected number of events $n$ in a given time interval that the average number of events $\lambda$ is known for. For large $\lambda$ the Poisson distribution can be approximated by the Normal (Gaussian) distribution.

The Poisson distribution can be applied to estimate the probability for the number of expected ion impacts $n$ in a certain area $A$ and time interval $\tau$ when the ion beam density $J$ is known. With $e$ being the elementary charge and $q$ being the charge state of the ions, $\lambda$ can be expressed as following:

$$\lambda = \frac{J}{qe} A\tau \tag{2.25}$$

Figs. 2.5 & 2.6 show the probabilities for $n$ events in a time interval with different expected average values ($\lambda$). For timed ion implantation with constant implantation intervals, it is obvious that implant spots will vary in ion distribution $n$ following the distribution function described above. Compared to that, the ability to detect every ion impact by SII enables the placement of exact numbers of ions per implant spot preventing Poissonian distribution statistics [126].

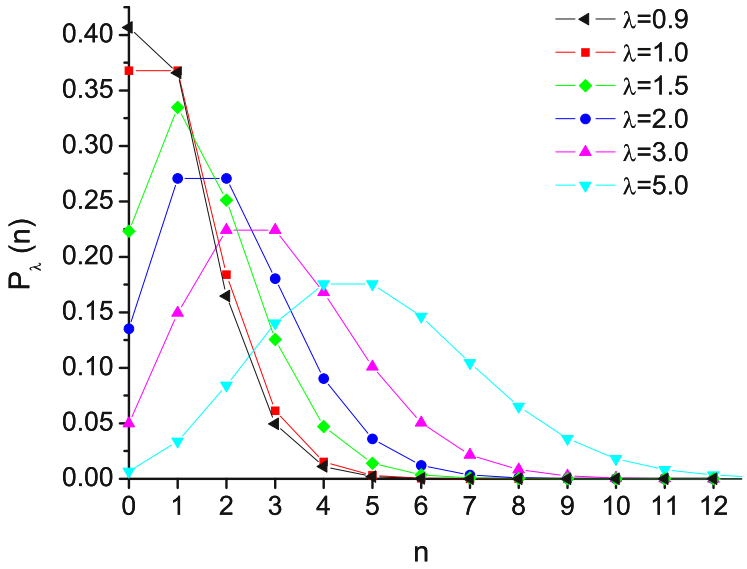


Figure 2.5: Poisson Distribution for different average event values $\lambda$.

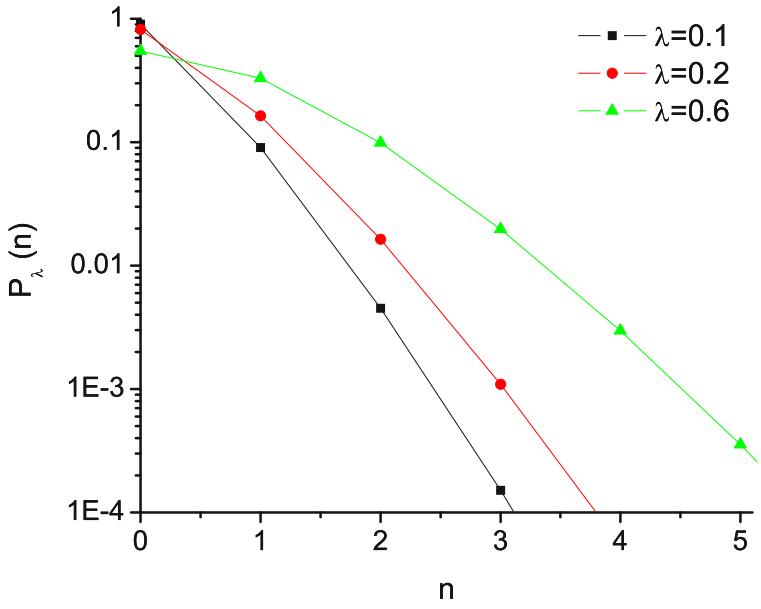


Figure 2.6: Poisson Distribution for different average event values $\lambda$.

## 2.5 Merits and Promise of Donor Spins as Qubit Candidates in Silicon

Among the many proposed ideas about how to physically realize qubits, donor spins in silicon are a very promising candidate. Besides the fact that the materials system itself possesses extraordinary qualities another circumstance plays to its favor. Silicon might be the best studied material on earth, on a fundamental and technological basis. Once the basic architectures have been demonstrated and leave the research environment, the step towards industrial scale fabrication will be relativley easy. This is a point that cannot be underestimated when assessing the various competing qubit systems. The implementation of large scale qubit arrays using nanofabrication tools in solid state systems was also envisioned when quantum dots as qubits were proposed [127]. Often referred to as artificial atoms, electrostatic gates define quantum dots which in the limit are occupied by one electron only. The spin state of the electron would be used as qubit and electrons could be moved closer to each other for communication and quantum logic operations, similar to trapped ion approaches in vacuum [21]. The initial work was all performed in III - V semiconductor materials (GaAs) and the coherent control of single spins has been achieved [128, 129]. A major drawback for that material system is the presence of a nuclear spin moment associated with the lattice atoms which create an inhomogenous magnetic field. These nuclear spins cause decoherence of the electron qubit spin via dynamic spin-diffusion from the nucelar dipole-dipole interactions [21]. This limits the electron spin decoherence time ($T_2$) to a few microseconds [21, 129, 130]. Switching to a different host material which is mostly made up from nuclear spin free isotopes such as silicon or germanium will reduce the amount of nuclear spins and thus the decoherence sources. The major isotope of silicon ($^{28}$Si) has a nuclear spin of zero and makes up 92.2 % of the natural occurring material. The other nuclear spin free isotope is $^{30}$Si and only 4.68 % of the atoms are associated with a nuclear spin caused by $^{29}$Si atoms with spin-$1/2$. The use of elements with nuclear spin free isotopes also enables the application of isotope engineering methods which can further reduce the amount of nuclear spins in the material. Quantum dot systems similar to the GaAs work have been implemented in natural silicon since [131–133].

Instead of confining the electron location electrostatically as in quantum dots, one can also introduce donor atoms into silicon that the electron gets bound to at low temperatures. This was first suggested by Bruce Kane [22] as mentioned in chapter 1. Extremely long electron spin coherence times have been achieved for this qubit candidate, approaching several seconds

in isotopically enriched silicon with less than 0.05 % $^{29}$Si content [134–136]. The nuclear spin coherence times are even longer [137]. Besides the mature nanofabrication technology, the extremely long electron and nuclear spin coherence times are the main incentive for this qubit system.

Due to the fact that the electron spin can be accessed much easier than the nuclear spin, the electron spin is more suited for communication, gate operations and readout, whereas the nuclear spin serves best for memory. The necessary coherent transfer of the electron spin information to the nuclear spin and back to the electron spin has been demonstrated for $^{31}$P donors [138]. The control and manipulation of the electron spin can be done with µ-wave pulses.

Since the magnetic moment of a single spin is very hard to measure, various spin selective spin to charge conversion mechanisms have been proposed and partially achieved. Among those donor spin state readout schemes are spin dependent scattering, recombination with defect centers, trapping or tunneling [139–145].

Phosphorus is the intuitive and most discussed and proposed donor species. It is the common n-type donor species and its electron and nuclear spin is $1/2$ and thus the simplest case in terms of spin description. However, other donors are considered and explored since they possess certain advantages. As discussed later, ion implantation is a common technique to place donor atoms in the host material. To keep the ion range straggling as low as possible, low implantation energies are preferred. Since the surface or interface are sources of noise a certain implant depth is required. For different donor species, the ion range straggle is different and changes with implantation energy. Since the implantation energy leads to different implant depths, it is not a good value for comparison. A plot for different donor species (phosphorus, arsenic, antimony and bismuth) showing the range straggle values versus implant depth can be seen in Fig. 2.7. The trend of reduced ion range straggling with increased ion mass of the donor species is clearly visible. Heavier species are thus preferred in terms of improved donor and qubit placement.
After implantation, the donor species need to get electrically activated by an annealing step. Another reason for choosing one of the heavier donor species is their lower diffusion constant and thus less movement away form their implant position during the annealing step [146].
Besides the larger range straggling and diffusion constant, phosphorus atoms can also segregate to the silicon oxide interface during the anneal or oxide growth [56, 134, 147]. This leads to pile up effects at the oxide interface where the phosphorus is electrically inactive. Overall,

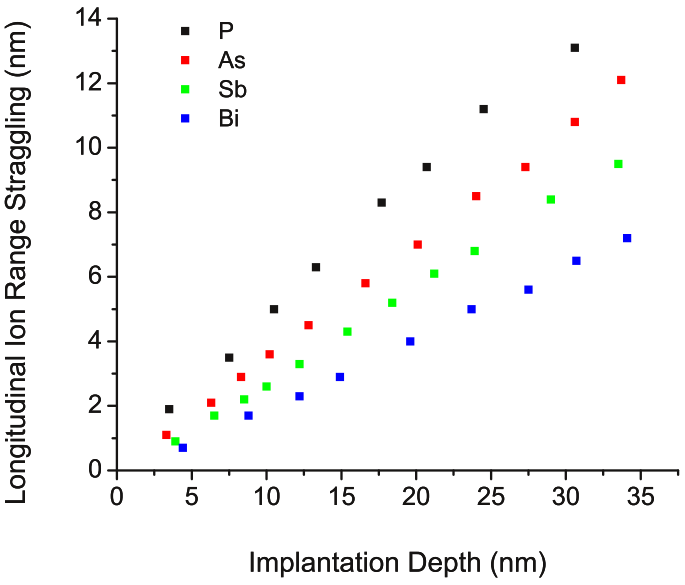


Figure 2.7: Monte Carlo Simulation (SRIM [116]) of the longitudinal range straggle versus implant depth for different implanted dopant species into silicon.

donor atoms in silicon are a promising path for qubits due to their very long coherence times and mature silicon nanofabrication technology.

## 2.6 Color Centers in Diamond: Another formidable Qubit Choice

Diamond possesses some remarkable material qualities. Its high electron mobility, high breakdown field, wide band-gap, high saturation velocity and a thermal conductivity five times larger than copper (at room-temperature) make it an ideal material for high-frequency, high-temperature, high-power and high-irradiation-tolerant electronic devices [148–154]. Despite all of these advantages, diamond never managed to stand up against its silicon counter part for device electronics. This has been due to several unresolved problems, such as a lack of shallow n-type dopant species, heteroepitaxy as a route to large-area single-crystal growth, re-crystallization issues at ambient pressures, low crystal quality and poor consistency of synthetic materials [149,154]. Great improvements have been made in regards to the latter points and single-crystal CVD diamond has been commercially available for a few years now. As it turns out, diamond not only is advantageous for conventional device electronics, but is a suitable host for qubits as well. Defect centers in diamond give diamond their characteristic color and have been known for a few decades. Only after the demonstration of nuclear magnetic resonance (NMR) on single NV centers in 1997 [155] and especially after the observation of coherent oscillations of the nuclear and electron spin in 2004 [27,28] it caught the attention of scientist as a qubit candidate. Since then, propelled by the emerging commercial availability of synthetic diamond substrates, work around the NV center has progressed drastically and the control of the electron and nuclear spin have been achieved [27, 28, 156–161] as has the coupling between two NV centers [162]. The NV center is the most studied [24, 80, 163], but not sole color center in diamond. Its natural abundance made it the perfect object of study among more than 500 color centers in diamond [164]. Differences in emission wavelength, line width and emission intensity offer a wide parameter range among these color centers [163].

One of the biggest advantages of color centers as qubits are, that the centers can be accessed optically and that all the spin manipulation and spin state readout can be done at room-temperature. The wide band-gap and deep center levels result in photo-stability and light in the visible range does not transfer the qubit electron into electronic bands of the host material. This is a big convenience factor whereas for other qubit systems low temperature setups need to be utilized. Further, as with silicon, diamond can be manufactured as a nuclear spin free lattice via the use of $^{12}$C atoms only. Natural diamond contains 1.1 % $^{13}$C atoms (nuclear spin of $1/2$) which can be much reduced by isotopic engineering during CVD growth

of the diamond substrates. This and the weak spin-orbit coupling in diamond and thus the limited spin interaction to the environment results in long spin coherence times even at room-temperature [165]. Those advantages are accompanied with some partially mentioned material drawbacks. All the initial work was done on natural occurring NV centers. As people try to engineer those centers, so that they can be arranged and placed next to or into device structures, it becomes clear that there are material issues that need to be solved. First off, diamond is not the thermodynamical stable form at ambient conditions. Device fabrication processes that seem given with silicon, e.g. re-crystallization and damage repair are not easily accomplished with diamond. Further, in silicon donor activation of 100 % can be achieved [134]. Unfortunately, this is not true for the NV center formation in diamond [70, 71, 77, 166] and is only a few percent depending on the implant energy. After nitrogen implantation, residual nitrogen atoms that did not convert to NV centers and remaining defect centers nearby can act as decoherence sources and limit the good properties inherent to natural occurring NV centers.

### Nitrogen Vacancy Center

The NV center in diamond is a defect center that consists of a substitutional nitrogen atom on a carbon lattice side neighboring one vacancy site. Six electrons are associated with the negatively charged NV center (unless denoted otherwise, the term NV center will always refer to the singly negatively charged state). One electron each from the three carbon atoms surrounding the vacancy site, two from the nitrogen atom and one electron that is captured from the bulk material [167]. Two unpaired electrons lead to spin triplets for the ground and first excited state with a spin conserving optical transition at 1.945 eV. The energy levels can be seen in Fig. 2.8. The $m_s = 0$ and $m_s = \pm 1$ levels are split by $\approx 2.87$ GHz at zero magnetic field. Applying a magnetic field will split the $m_s = \pm 1$ levels. The $m_s = 0$ state has a higher fluorescent rate than the $m_s = \pm 1$ levels [168]. Thus, by choosing $m_s = 0$ and e.g. $m_s = -1$ as the two levels of the qubit, its state can be easily determined.

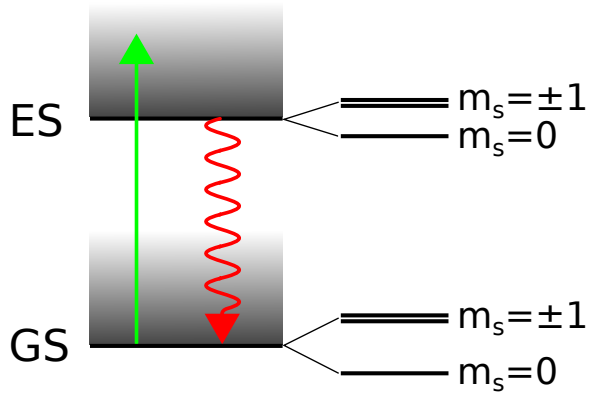


Figure 2.8: Energy level diagram of the NV center.

Further, due to a spin selective non-radiative transition between a singlet state, the qubit can be optically initialized into the $m_s = 0$ state [169]. The ground state can be optically excited resonantly with light at 637 nm wavelength. However, shorter wavelengths (e.g. 532 nm) are predominantly used for excitation involving phonon decay processes.

# Chapter 3

# Ion Beamline Setup

*This chapter gives an overview of the ion beamline setup used for the presented implantation work, including some of the upgrades improving its capabilities.*

## 3.1 Overview

The beamline setup used here features all the necessary elements for ion implantation with scanning probe aligned ion beams. The main parts are various ion sources, a 90° analyzing magnet and two implant chambers with one containing a scanning probe microscope system which will be described in detail in chapter 4. The beamline was originally built at Lawrence Livermore National Laboratory for an Electron Beam Ion Trap, then moved to Lawrence Berkeley National Laboratory and then equipped with a SPM system. Schematics of the beamline layout showing all the major parts can be seen in Figs. 3.1 & 3.2. The vacuum chamber elements of the beamline are mounted $\approx 2\,\mathrm{m}$ off of the ground and the vacuum section has a total length of almost 5 m. Bertan Associates, Inc voltage controllers are used to supply high voltages to the different einzel lens and quardrupole elements along the beam path. With those lens elements the beam can be focused and steered along the beamline. Granville-Phillips Vacuum gauge controller (series 303, 307, 350) in combination with convectron and ion gauges are used to monitor the pressure inside the beamline at various locations. Differently sized turbo pumps maintain a vacuum level of below $1 \times 10^{-7}$ torr.

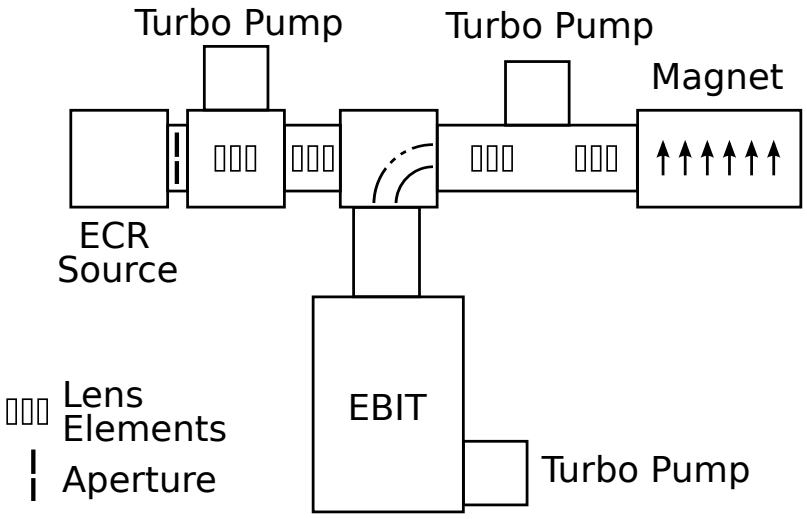


Figure 3.1: Schematic of all the important elements of the beamline section up to the analyzing magnet.

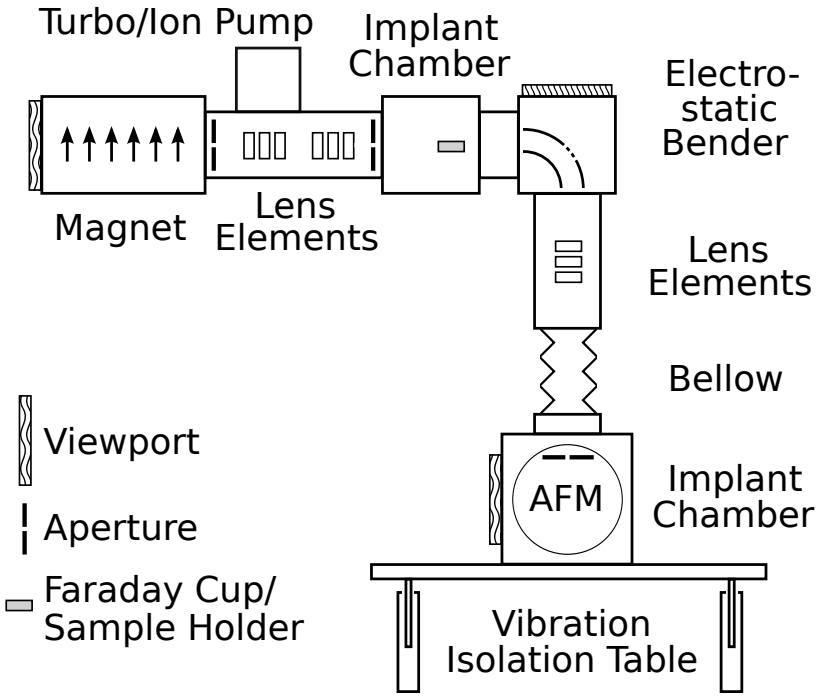


Figure 3.2: Schematic of the beamline section after the 90° analyzing magnet featuring the different implant chambers and the scanning probe setup.

## 3.2 Ion Sources

Three ion sources are used to acquire the presented data. Two Electron Cyclotron Resonance (ECR) Sources and the original Electron Beam Ion Trap (EBIT) source, which will be described in the following.

### 3.2.1 ECR Sources

An ECR source is a type of plasma source where electrons are forced onto a cyclotron motion ($\omega_c = eB/m$) by a magnetic field. Micro- or radio-frequency waves are coupled to the plasma to maintain the cyclotron motion and the plasma state. The electrons ionize gas atoms which then can be extracted from the source. Both sources connect to a microwave power supply built by Sairem which produces microwaves at a frequency of 2.45 GHz at a maximum output power of 2000 W. A wave-guide three stub tuner enables the tuning of the microwave guide for optimal coupling of the microwaves to the source plasma. Both source bodies are electrically isolated from the beamline and connected to high voltage (HV) power supplies with the extraction plate being connected to ground. Thus the waveguide and gas supply lines need to be electrically isolated from the source as well and all parts on HV are housed in a protective cage. Voltages up to 14 kV can be applied before a voltage break down occurs with the current isolation design. Both sources are mounted at the same location of the beamline, so that only one source can be used at a time.

#### ECR1 source

A full description of the source can be found in ref. [170] and Fig. 3.3 shows its schematic. The source is made from stainless steel, features a permanent-magnet dipole structure and a coaxial microwave feed through for coupling the microwaves to the plasma via an antenna. Further it is equipped with water cooling to prevent overheating. The source has three ports and an extraction hole in the back plate. The microwaves are fed through port #2, the various source gases are supplied through port #1 and an oven is attached to port #3. Port #1 is also used to feed in a retractable metal sample which is mounted on a linear motion feedthrough. Due to the lack of a pressure gauge that is connected directly to the source body, the absolute pressure within the source can not be measured. An ion gauge behind the extraction hole is used as a gas pressure indicator. The design value for the gas pressure is a few $10^{-4}$ torr. The ion source produces multiply charged ions and the plasma electron energy

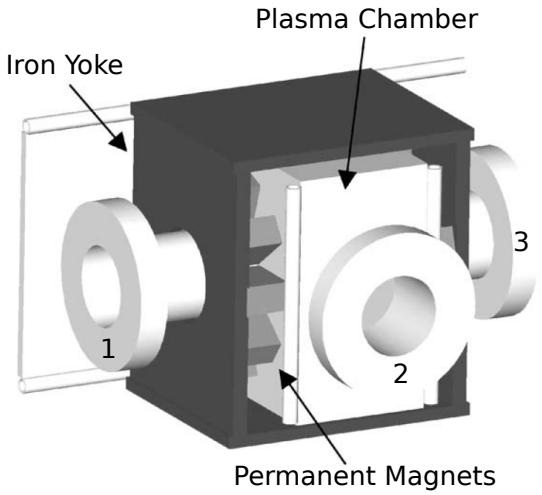


Figure 3.3: Schematic of the ECR1 source [170].

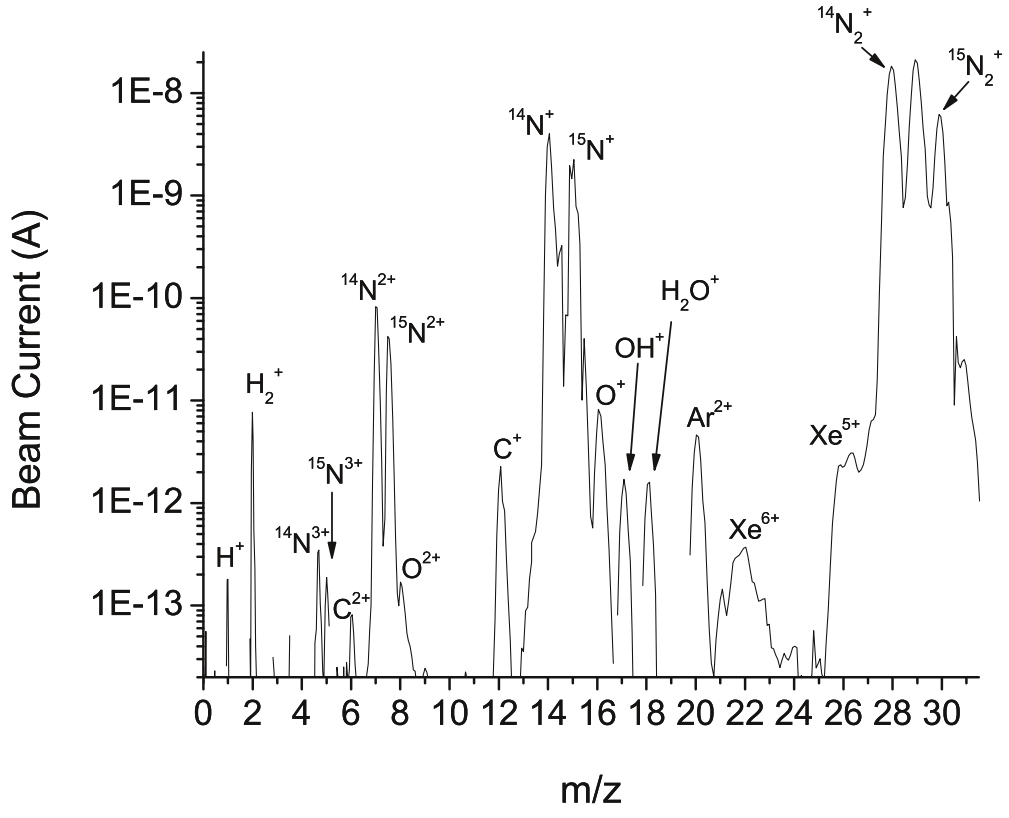


Figure 3.4: Magnet scan of ECR1 with nitrogen-14 and nitrogen-15 gases supplied to the source. The beam is extracted at 6 kV. Besides impurities like oxygen and water, previously run gas species are still detectable at low amounts (argon, xenon).

is up to 100 eV by design. $Xe^{6+}$ and $Ar^{6+}$ ions could be generated and a magnet scan of a gas mix of nitrogen-14 and nitrogen-15 can be seen in Fig. 3.4.

### ECR2 source

A schematic and a picture of this source can be seen in Fig. 3.5. The full description of the source is available in ref. [171]. It is again a permanent magnet source and the microwaves are coupled directly into the plasma chamber via a microwave window which also acts as the vacuum break. The source is much smaller in chamber volume than the previously described

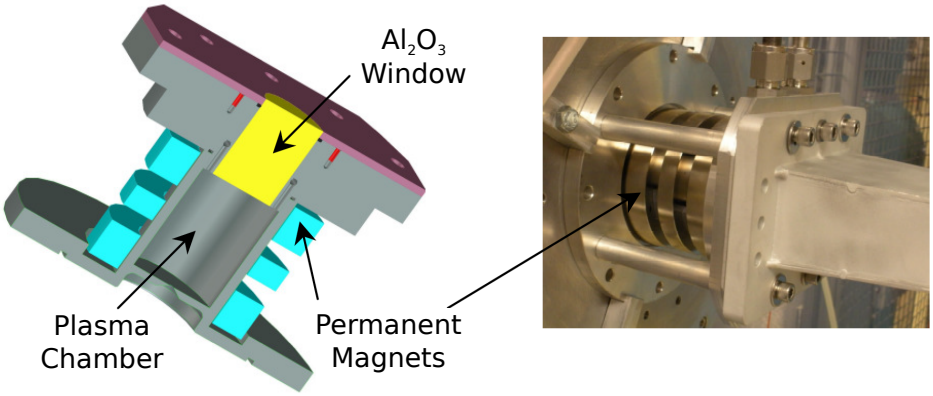


Figure 3.5: Schematic and picture of the ECR2 source [171].

ECR source, 4 cm in diameter and 5 cm in length. Besides the extraction aperture, two small holes are used for gas supply and as a return-line to a Barocell pressure gauge to monitor the gas pressure inside the source. The design value for the pressure is a couple of mtorr. Compared to the ECR1 source, this source features a much better ratio of atomic to molecular hydrogen species due to a higher power density. A nitrogen-15 magnet scan from this source can be seen in Fig. 3.6.

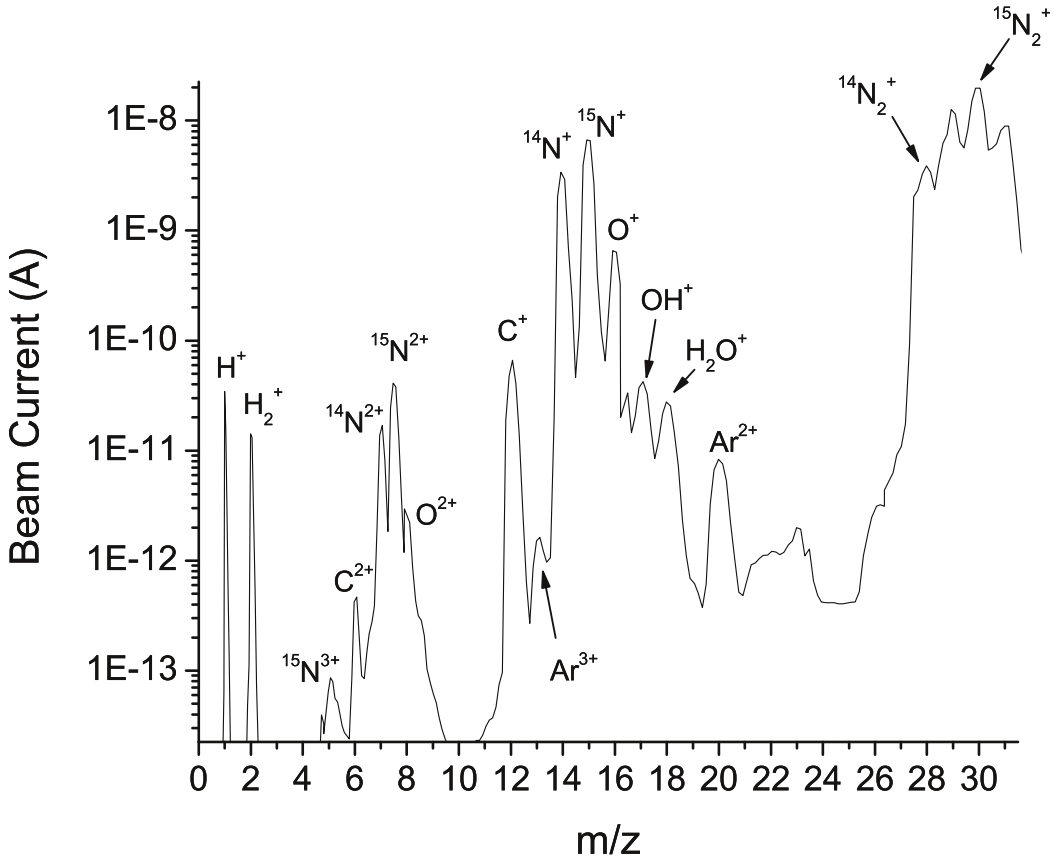


Figure 3.6: Magnet scan from ECR2 with nitrogen-15 gas as source supply at a source pressure of 0.5 mtorr. The beam is extracted at 4.6 kV.

### 3.2.2 EBIT

The EBIT is the beamline's original and most versatile ion source [172,173]. It was developed as the EBIT II at Lawrence Livermore National Laboratory where the first EBIT was built as well [174]. A drawing of the EBIT can be seen in Fig. 3.7. A high density electron beam

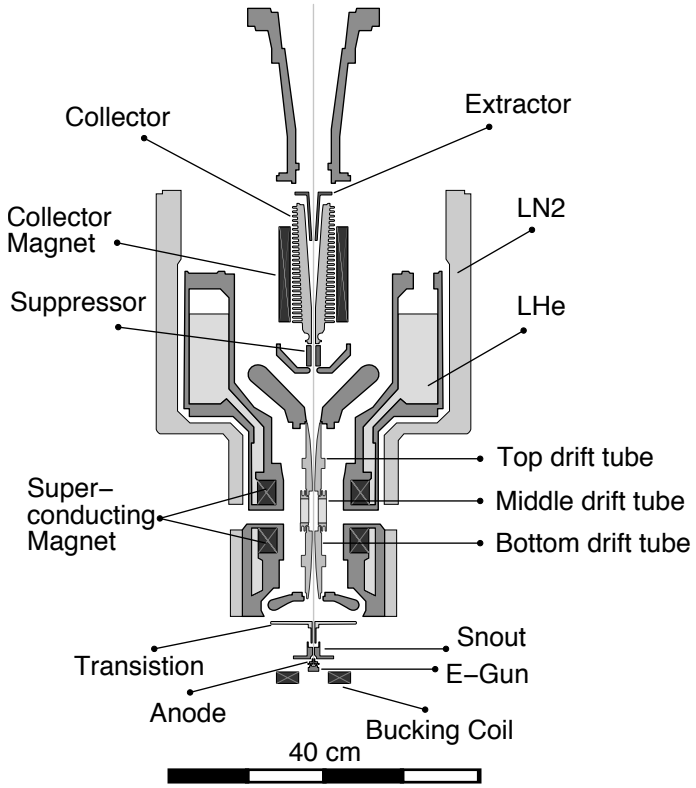


Figure 3.7: Schematic of the Electron Beam Ion Trap [173].

continuously removes electrons off of trapped ions. The positive ions are electrostatically trapped in radial direction by the electron beam itself. Voltages on the top and bottom drift tube confine the ions along the beam axis. In order to achieve the necessary beam densities that are required to generate highly charged ions, superconducting Helmholtz coils are used to generate a magnetic field of 3 Tesla. The electron beam is compressed to $\approx 50\,\mu m$ in diameter and reaches current densities of up to $2000\,A/cm^2$. Electron beam energies of up to 30 keV enable the creation of helium like xenon and bare ions up to about $Kr^{36+}$. Behind the drift tube sections, the electron beam is captured by a collector plate and ions are extracted from the source at a potential of up to $\approx 7\,kV$. Depending on the charge state, ions of various potential and kinetic ion energy are available for ion implantation (see Fig. 3.8).

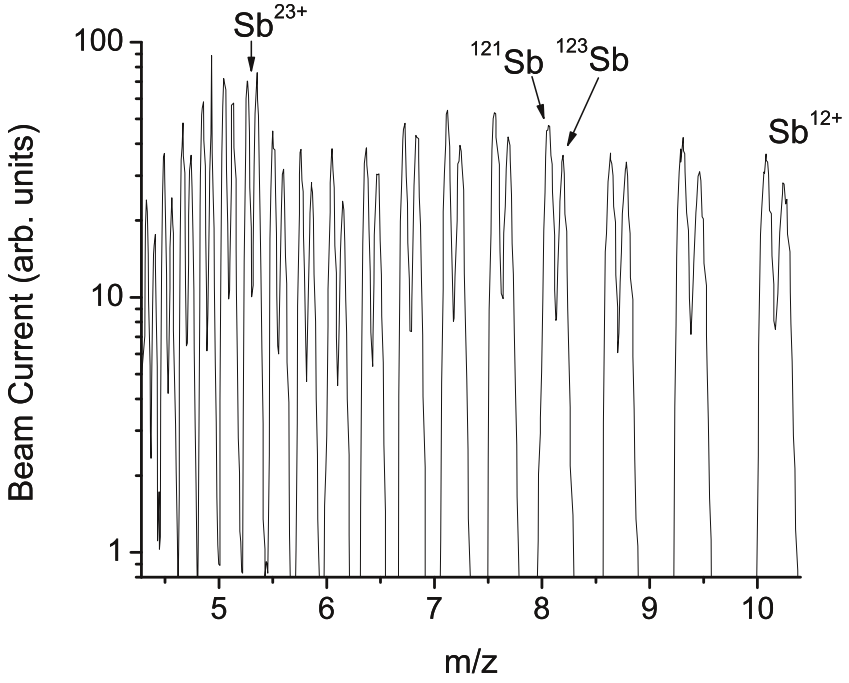


Figure 3.8: Magnet scan showing antimony peaks of various charge states generated with the EBIT source. The beam was extracted at a voltage of 7.5 kV.

## 3.3 Analyzing Magnet - Ion selection

The ion sources produce ion species varying in charge state and element type. All species are extracted from the ion source at the same extraction voltage $U_{ext}$. In order to select the ion species of choice form the overall ion beam, a 90° analyzing magnet is used. For non-relativistic ion velocities $v$ the kinetic ion energy $E_{kin}$ is given by:

$$E_{kin} = qU_{ext} = \frac{1}{2}mv^2 \quad \Rightarrow \quad v = \sqrt{\frac{2qU_{ext}}{m}} \tag{3.1}$$

A particle of mass $m$ and charge $q$ injected into a magnetic field (with $\mathbf{v} \perp \mathbf{B}$) travels on a circular path with radius $r$ which can be described by the Lorentz and centripetal force:

$$qvB = m\frac{v^2}{r} \tag{3.2}$$

In practice, the extraction voltage is set to a fixed value to achieve the desired kinetic ion implant energy for a certain charge state. The beamline geometry, aperture positions and the extend of the magnetic field set boundary conditions, so that only ions which travel on a certain trajectory with radius $r_0$ can pass the analyzing magnet. From equations 3.1 & 3.2 one obtains that only particles of the same mass over charge ratio pass the analyzing magnet and reach the implant chamber.

$$\frac{m}{q} = \frac{B^2\, r_0^2}{2\, U_{ext}} \tag{3.3}$$

From equation 3.1 also follows that particles of same mass to charge ratio which pass the analyzing magnet have same velocities. Rewriting equation 3.3 lets one determine the necessary magnetic field to bend a certain ion species at a given extraction voltage.

$$B = \sqrt{\frac{2}{r^2}\, U_{ext}\, \frac{m}{q}} \tag{3.4}$$

In order to increase the range of kinetic energy and charge state at which ions can be implanted, the previous power supply (Hewlett Packard 6031A Systems Power Supply: 0 - 20 V, 0 - 120 A, 1000 W) controlling the electromagnet is replaced by a new one (Lambda Genesys Powersupply: 0 - 33 V, 0 - 330 A, 10 kW). Now the maximum magnetic field is not limited by the supplied magnet current anymore but rather by the cooling power to the magnet. In order to prevent overheating, water is constantly passed through the coils which generate the magnetic field. Temperature sensors at the magnet outlet act as monitors and control an interlock system. The magnet is operated up to a displayed water temperature of 80 °C

and a peak magnet current of 230 A. This allows bending and selection of ion species with $U_{ext} \times \frac{m}{q} < 220$ - 230.

During the swap of the power supplies the outdated magnet scanning program is replace by a more user friendly one written in LabVIEW. The magnet scans are obtained by sweeping the current through the electro-magnet and recording the beam current from a Faraday cup in the implant chamber. The magnetic field is recorded with a Gauss meter (F.W. Bell Gaussmeter Series 9900). For peak identification the magnetic field is converted to mass over charge values.

## 3.4 Implant Chambers

The beamline has two implantation chambers (see Fig. 3.2). The first one is a 6 inch cube that contains a Faraday cup mounted on a linear motion feedthrough and a sample holder on a goniometer (x, y, z, $\pm 90°$ rotation). Both are electrically isolated so that beam currents can be monitored and samples biased. The $1 \times 2\,\text{inch}^2$ travel range of the sample holder allows multiple samples to be mounted and implanted without breaking the vacuum. The aperture in-front of the 6 inch cube and the Faraday cup entrance are both 3.5 mm in diameter. A plate with a 1 mm and 300 µm hole can be moved in-front of the sample holder, so that three different ion beam spot sizes are available for implantation. The chamber also features the option of connecting the sample to a copper braid connected to a liquid nitrogen reservoir. This allows ion implantations at below room-temperature.

The second implant chamber is a 8 inch cube that holds the scanning probe microscopy setup. The setup is described in detail in chapter 4.

## Acknowledgments

The author thanks Qing Ji, Jani Reijonen, Mark Regis and Arunabh Batra for supplying the ECR sources, discussions and help to get them to work properly.

# Chapter 4

# Contact SPM Setup

*This chapter describes the SPM setup used for the presented work, including all the upgrades and modifications made to the formerly existing system.*

## 4.1 General Description

A home build SPM system is used for sample imaging. The description of the previous system performance can be found in refs. [173] & [49]. It features a PI stage (Physik Instrumente - Model: P-733K016, S/N 000001) with $100 \times 100 \times 10\,\mu m^3$ travel range and a resolution of less than a nanometer. The stage is operated by a RHK Technology SPM100 controller that is connected to a PI high voltage controller (PZT-Servo Controller E-509.C3A, LVPZT-Amplifier E-503.00 and Display/Interface E-516). The RHK imaging software is used for data acquisition. For our work we use piezo-resistive cantilevers which are supplied by Rangelow et al. [109,175] and mounted under a 10° angle to the surface.. The Wheatstone bridge was fully integrated in the cantilevers and is biased at 1 V. The signal from the SPM tip is amplified twice before it is send to the RHK SPM100 controller; first by an INA 110 instrumentation amplifier in vacuum and then by a Stanford Research Systems low-noise preamplifier (Model SR560) outside the vacuum chamber. The SPM stage and the tip are mounted in an 8 inch cube that is attached to the beamline (see Fig. 3.2). A schematic of the circuit diagram with all the SPM components can be seen in Fig. 4.1, a CAD drawing in Fig. 4.2. It shows the piezo-motion stage onto which the sample holder is mounted. The SPM tip is mounted on a flexure stage for coarse positioning. Linear motion feedthroughs (Mitutoyo 0 - 2", .0002", No.297-201-01) are used to address the flexure stage. A viewport mounted

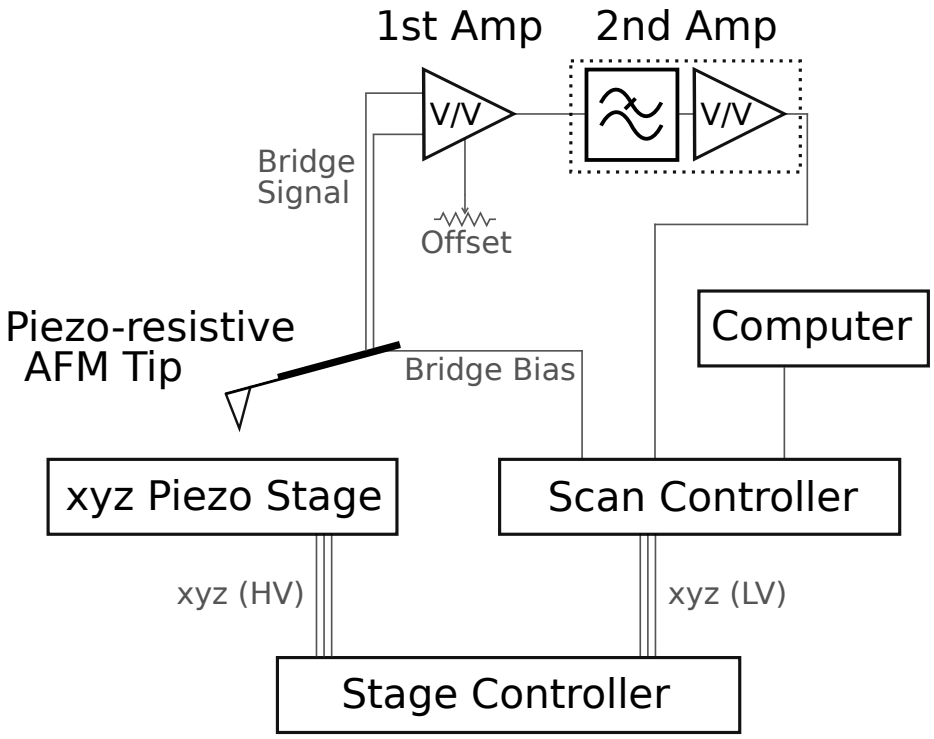


Figure 4.1: Schematic of the SPM setup.

into one of the 8 inch flanges offers optical access for coarse tip positioning. Samples can be electrically connected via push pins for fast and easy exchange. The formerly existing setup is modified to reduce excessive tip wear, increase the vibration isolation and enable easier coarse adjustment of the tip position which will be described in the following.

## 4.2 Three Axis Flexure Stage

The piezo-resistive SPM tips were mounted on a two axis flexure stage initially. This allowed the coarse approach of the tip to the sample and the tip movement in and out of the ion beam path. The ion beam enters the implantation cube through a 1 mm aperture and the sample is mounted on the piezo-stage with 100 by 100 $\mu m^2$ x-y travel range. Thus the sample needs to be mounted within the area of the sample holder which is hit by the beam spot. This is easily achievable, as long as the exact implant location on the sample is not that crucial, e.g. generation of a implant pattern at a random sample position. Compared to that, the implantation of a certain sample location as it is required for the doping of silicon devices is much harder. Since the tip could be moved in one lateral direction only, combined with

the limited travel range of the piezo-stage, this required the sample to be mounted within 100 µm. In addition, occasional drifts of the coarse stage during pump down procedures made this very inconvenient. Thus a third axis was added to the flexure stage to enable a full coarse alignment procedure with a few mm travel range in each direction. Despite that, only one sample at a time could be mounted since the coarse motion stage moves the tip and not the sample. Latter case would enable multiple sample exposures without breaking vacuum, as it is the case for a new non-contact SPM currently under construction.

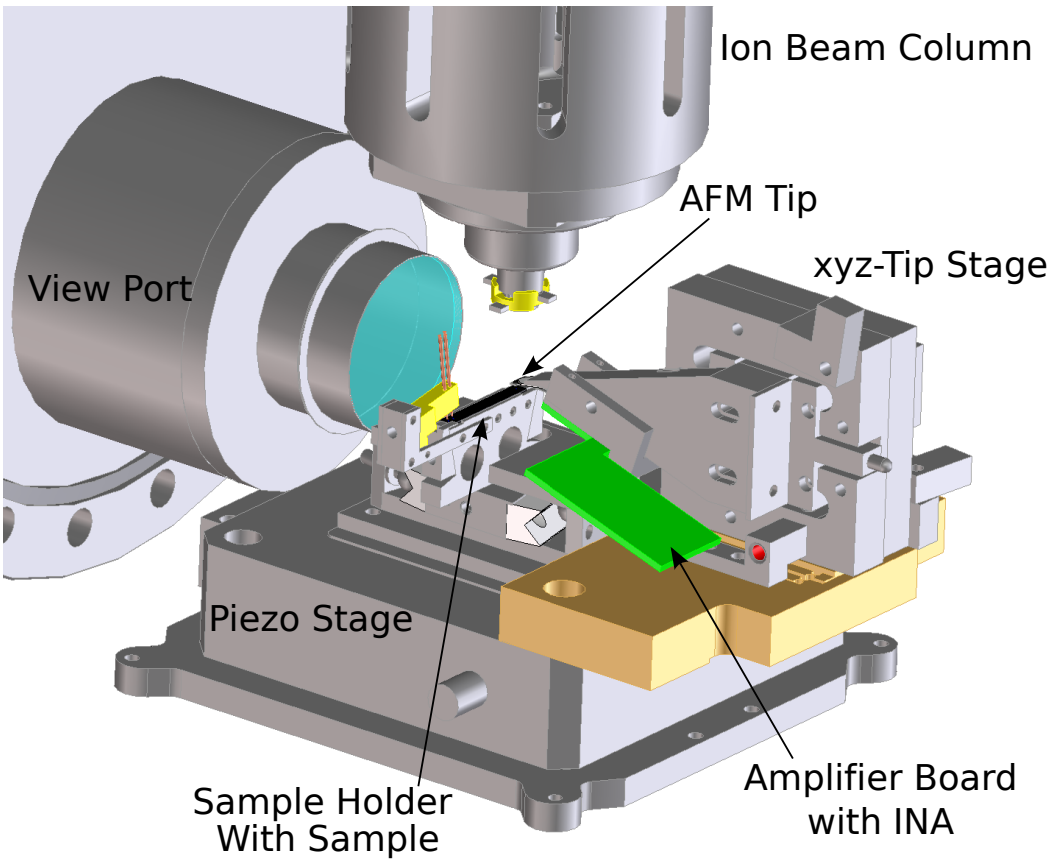


Figure 4.2: CAD drawing of the SPM system. The last aperture (1 mm in diameter) right before the SPM tip is not shown in order to prevent blocking the view onto the SPM tip in this sketch. The aperture is located in a cylindrical rod which is cut under an angle of 45° to act as a mirror to get a close up look along the beam path through the optical viewport. The sample is shown in black on the sample holder and has a length of 25 mm.

## 4.3 Vibration Isolation Table

The SPM as part of the ion beamline is not operated in an ideal environment and surrounded by a lot of vibration sources. The influence of the closest turbo pump on the noise characteristic of the SPM was shown previously [173]. An ion pump is added next to the turbo pump to enable pumping with reduced vibration generation. Further the 8 inch cube with the SPM system is put on a vibration isolation table which is equipped with four air supplied legs (Newport VW-3030-SP). To isolate the cube from the beamline section, a soft bellow is used for connection. This reduces the vibrational influence of the closest turbo pump so that the ion pump could actually stay turned off most of the time. A noise power spectrum with the SPM tip kept in contact at a similar force setpoint used during image acquisition is shown in Fig. 4.3. The clear influence of the vibration isolation table on the noise level can be seen easily.

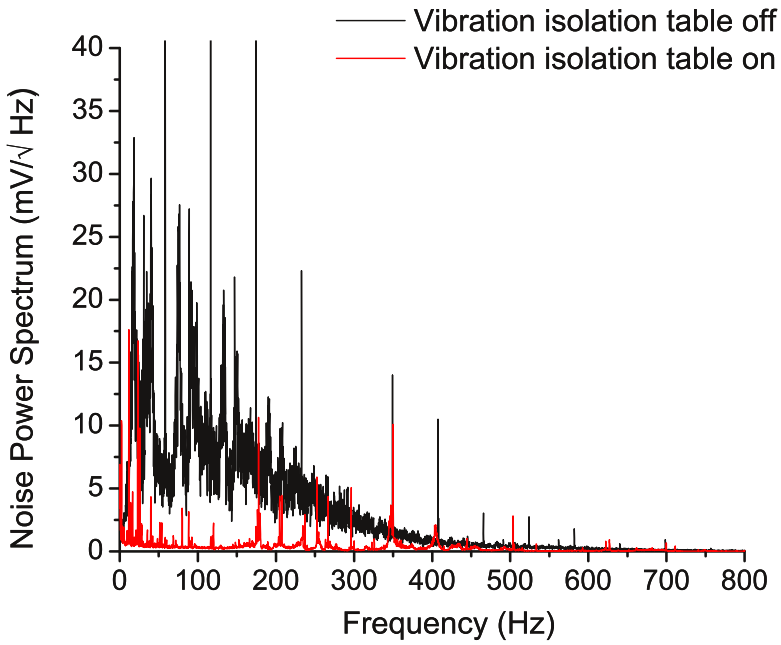


Figure 4.3: Influence of vibration isolation table on the noise power spectrum.

## 4.4 Increase of Cantilever Deflection Sensitivity

The main issue with the existing setup was excessive tip wear down to the tip cone of the tip as can be seen in [173]. This is problematic for the accurate placement of ions. The tip apex is not well defined anymore and one cannot determine the exact SPM cantilever position and thus the collimated ion beam location in respect to the sample from SPM scans. Another concern with these high tip wear rates are nitrogen implantations into diamond substrates where the photoluminescence of the color centers is measured afterwards. SPM scans of the sample area to determine the proper implant location will contaminate the sample with tip material which might interfere with the optical measurements then. Due to the fixed internal voltage setpoint range of the RHK system, noise sources needed to be eliminated and the amplification of the cantilever signal addressed.

The existing components of the amplification stage in vacuum and the voltage box to offset the bridge signal in vacuum were taken apart and modified. The most significant improvement was achieved by addressing various grounding issues. Those prevented the amplification of the signal by the Stanford pre-amplifier previously. Since the noise was also magnified and not only the signal no effective gain increase was achieved. By addressing the grounding problems, an amplification increase of the Wheatstone bridge signal was made possible. The final and current settings are an amplification of the signal by 500 in vacuum by the instrumentation amplifier and by a factor of 20 by the Stanford pre-amplifier. The latter also functions as a low pass filter (12 dB at 300 Hz).

The calibration of an SPM piezo characteristic and the tip cantilever bridge signal sensitivity can be done via force distance (FD) curves and the use of well known sample features. Fig. 4.4 shows two FD-curves taken with the SPM setup after the upgrade. They are taken on an SPM grating sample for z-direction calibration. The specs value of the feature step height is 200 nm. The FD-curve in black/red is taken in a trench region, the one in green/blue on a step region. The absolute starting point above the sample is the same for both FD-curves. With the known step height, the driving voltage of the z-piezo stage (x-axis) can be converted into a length scale. For that a point on each FD-curve is chosen, where the tip is in contact with the sample and one measures the same bridge signal from the SPM cantilever. That ensures the same tip bending and the difference in piezo driving voltages on the x-axis for those two contact points corresponds to the 200 nm step height. In this case 200 nm correspond to 0.400 V piezo stage controller driving voltage ($V_{driving}$). The slope of the FD-curve with the tip and sample in contact then yields the cantilever response sensitivity ($\alpha$) of the

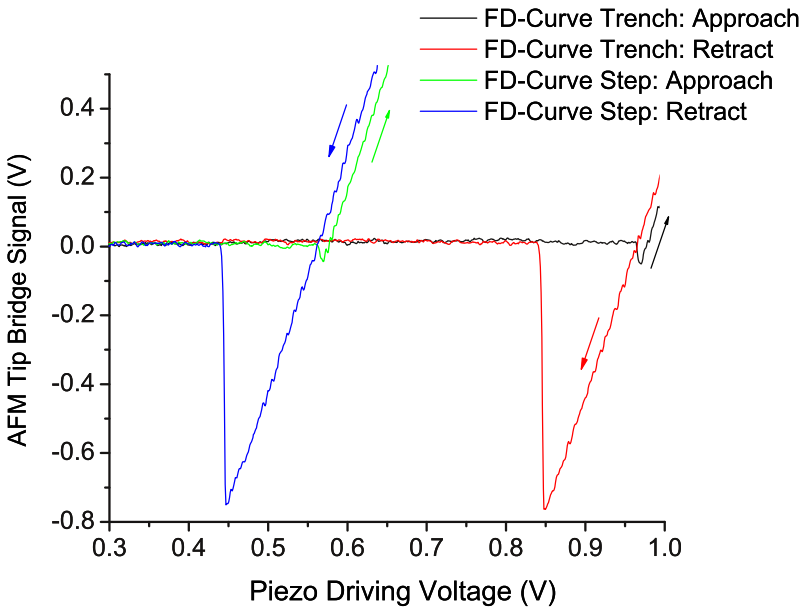


Figure 4.4: Two force distance curves taken with the SPM on a grating sample (200 nm step height for z-direction calibration). The force distance curve in black/red was taken in a trench region, the green/blue one on a step region.

SPM system. In this case the value is 71.9 $\mathrm{nm/V_{bridge\ signal}}$ or 13.9 $\mathrm{mV_{bridge\ signal}/nm}$. This is a factor of 5560 larger than the value of 2.5 µV/nm reported in ref. [173] and comparable to SPM systems that use a laser and photo diode setup to measure the cantilever deflection (typical around 100 - 200 $\mathrm{nm/V_{deflection}}$). This sensitivity improvement consists of an amplification increase by a factor of 1000 and the use of more responsive SPM cantilevers with increased Wheatstone bridge output. Thus at the same voltage setpoint of the Wheatstone bridge signal for the feedback loop and a tip with the same spring constant $k$, the force applied by the tip to the substrate is decreased by 5560 and excessive tip wear is avoided.

$$F = \frac{V_{set}}{\alpha} k \tag{4.1}$$

As mentioned, the value of the cantilever sensitivity is comparable to optical SPM systems. Unfortunately, the applied force onto the sample is still relatively high after the upgrade though the excessive wear problem is resolved. Regular SPM tips for laser/photo-diode readout come in a variety of spring constants of the cantilever body. The thinner the cantilever body the smaller the spring constant, assuming the other dimensions stay the same. A cantilever will reflect the laser spot always the same amount for a given cantilever deflection and

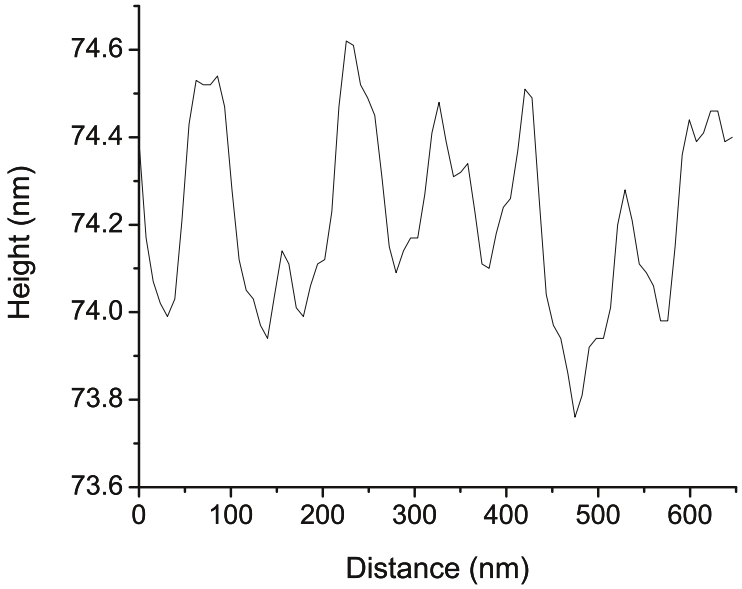


Figure 4.5: Cross section of an SPM scan across the flat surface of one of our silicon transistors. The height resolution of the SPM system is below 1 nm. The scan was taken with the system attached to the beam line while being in high vacuum and the vibration isolation system activated.

independent of its thickness and thus will not change the deflection sensitivity of the SPM system. In order to reduce the applied force onto the tip and sample, one an easily change to an SPM tip with a smaller spring constant. A wide range of spring constants are commercially available (e.g. 0.01 - 50 N/m) and by simply choosing a different tip, the applied force can be reduced by a few orders of magnitude. Unfortunately the case is not as easy for the piezo-resistive SPM tips that are supplied which are designed for tapping/non-contact mode and thus stiffer by design. A reduction in tip spring constant would entail a new fabrication run. The issue can be partially improved by cantilever post processing where notches are cut into the cantilever sides to reduce the spring constant. Despite the significant increase in cantilever sensitivity to a value comparable to commercial laser setup SPMs, the applied force onto the tip is still fairly high. A typical setpoint of the cantilever signal during imaging is around 100 mV for which a stable imaging condition is achieved. For a spring constant of 10 N/m of our tips this would translate to a force of 72 nN applied to the tip which is still too much for contact mode operation. During the conducted experiments it was found that the tip wear was not excessive as previously experienced and to a level one would expect for such

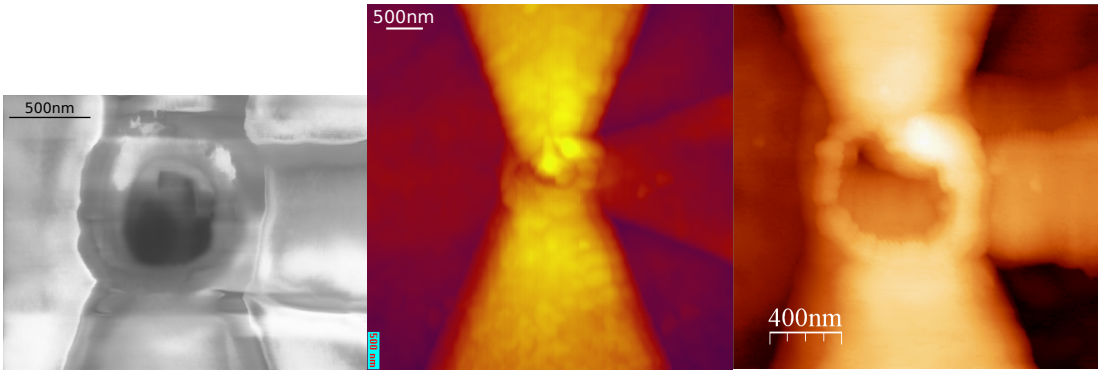


(a) SEM (b) Our SPM (c) Non Contact SPM - Ilmenau

Figure 4.6: Comparison of SEM, our SPM and Ilmenau non-contact SPM image quality of same device.

a force value. However, this was still too high for desired image qualities, although an overall good $z$-resolution of below 1 nm is achieved by the SPM system as can be seen in Fig. 4.5. A comparison of three images of the same device taken with a SEM system, our contact SPM system and a non-contact SPM system can be seen in Fig. 4.6. The better image quality with the non-contact SPM due to a pointier unworn tip is clearly visible.

## 4.5 Summary & Outlook

In summary, the elimination of electrical and vibrational noise sources before and at the first amplification stage of the Wheatstone bridge signal lead to an improved system. The bridge signal could be increased by a few orders of magnitude, thus increasing the cantilever sensitivity $\alpha$ (bridge signal [V] per cantilever deflection [nm]). Due to a fixed set point voltage range of the RHK scanning hardware, this reduced the applied force of the cantilever onto the surface according to equation 4.1 and thus the tip wear. Further, the addition of a third coarse stage enabled a convenient alignment procedure of the tip to the area of interest.

During the course of this work, the decision was made to build a second SPM system (non-contact type). This also gives the opportunity to improve some more fundamental design elements of the SPM system which will allow a more versatile implant process. To enable high precision ion implants, a higher sample through put and a more convenient implant procedure in the future the following SPM upgrades will be implemented:

- Non-contact mode SPM with piezo-resistive SPM tips to reduce tip wear and improve

image quality.

- Implementation of a sample coarse stage to enable access to a larger implant area. This will allow implantation of multiple samples without breaking vacuum.

- Relocation of the implant apertures from the SPM cantilever body into the tip cone. This will become clearer later on but is mentioned here already for completeness (see section 6.5). Due to beam divergence the beam spot will be broader once it hits the sample surface if the final aperture is far away from the surface. Even for small beam divergences the amount of broadening can not be neglected for typical SPM tip lengths and would negate the use of implant apertures down to a few nanometer.

## Acknowledgments

The author thanks Frederic Gicquel for the flexure stage design and CAD drawing, Andreas Schuh for taking a reference image with a non-contact SPM at the Technical University of Ilmenau and Arun Persaud for helpful discussions.

# Chapter 5

# Setup of a new Source for Metal Ion Beam Creation

*In this chapter the development of a new ion source setup for low charge state metal ions is discussed. It functions as a complementary source to the electron beam ion trap (EBIT) with the advantages of a more convenient and cheaper running procedure.*

## 5.1 Motivation

In order to perform deliberately placed donor implants with the SPM setup, an ion source delivering the desired donor ion species is required. So far this was done with the EBIT which can produce highly charged ions of various kind, like phosphorus, antimony and bismuth [50, 172, 176]. The various precursors were supplied to the ion source in form of $PF_3$ gas or from an oven attached to the source in which solid metal substances were heated up. Due to the high electron beam densities in the EBIT source, all introduced species are decomposed to their individual components, e.g. phosphorus and fluorine in the case of $PF_3$ [172]. Despite the great capabilities and design parameters which this source offers, the high maintenance requirements are a big drawback for day to day work. This is mainly due to the liquid helium cooled superconducting Helmholtz coils. A lot of implant tests can be done with noble gas ions of similar mass as the desired donor species, e.g. xenon or argon. For these ions, which can be easily extracted from an electron cyclotron resonance (ECR) source attached to the implantation setup, similar damage profiles and ion ranges in the target material can be expected. In light of the assembly of a second ion implantation setup with a new non-contact mode SPM, setting up the ECR sources for donor species production is an appealing goal to

have two fully working and complementary ion implantation beamlines.

The high potential energy inherent to highly and multiply charged ions provides additional energy for single ion detection independent of the ion kinetic energy. In sensitive detection schemes, e.g. µm sized FETs and 100 nm scale FinResistors (see chapter 7), single ion impact detection can be implemented without using secondary electron emission. There, the electronic and nuclear stopping power at a given kinetic energy leads to large enough signals for reliable SII detection. The low charge states created by the two ECR sources are sufficient for the implant work goals, when extracted at an appropriate high voltage. Ion beams are extracted easily from the two ECR sources if the source material is supplied in gaseous atomic or molecular form. Among the tested gases, but not limited to them, are $H_2$, He, $N_2$, Ar and Xe.

Although the sources create medium charge states (up to $Xe^{7+}$ for ECR1) the nitrogen molecules are not broken up easily and the molecular species is predominant. This is in contrast to the EBIT, where molecular species basically do not exist. This fact enables certain implants though, that address the creation of isolated dimers in a host system. After the molecule hits the surface it splits up and the two atoms come to rest close to each other after after losing their kinetic energy. Achieving close-by atoms with atomic implant species would require a very high dose which can be disadvantageous.

On the other side, the low conversion into atomic species leaves only fractions of the supplied source gas for atomic implants. The higher the charge state the less ions are created which can become inconvenient if one tries to reach a higher implant dose and energy at maximum extraction voltage. This not only plays a role during the creation of charged species from gaseous source supplies, but may also affect the creation of metal ion species with similar approaches as mentioned for the EBIT system, which is explored in the following.

## 5.2 General Aspects

In the ideal case, an ion source puts out only species deliberately introduced into the source chamber. Leaks, contaminations or memory effects (previously used source gases incorporated into the chamber wall) are present though and need to be considered. The output of an ion source can be characterized with mass analyzers. As described in chapter 3.3, for this we use a 90° analyzing magnet in our setup. It belongs to the class of velocity filters and separates species of equal mass over charge (m/z) ratios. This can lead to overlap of different species at the same m/z value. Some species will not be suitable for ion implantation if one desires

a high purity implant or are not even detectable if dominated by the overlapping species. Table 5.1 shows the m/z values for both antimony isotopes up to charge state 7+. Quite a few antimony species fall into m/z ranges of interfering species, as e.g. water (contamination) or nitrogen which is used for implants into diamond and which can also originate from leaks. Charge states higher than 7+ will not be produced in significant amounts and also dominated

| Charge State | m/z ($^{121}$Sb) | m/z ($^{121}$Sb) | Interfering Species |
|---|---|---|---|
| 1+ | 121 | 123 | |
| 2+ | 60.5 | 61.5 | |
| 3+ | 40.33 | 41 | $Ar^+$ |
| 4+ | 30.3 | 30.8 | $^{15}N_2^+$ |
| 5+ | 24.2 | 24.6 | |
| 6+ | 20.2 | 20.5 | $Ar^{2+}$ |
| 7+ | 17.3 | 17.6 | $OH^+$, $H_2O^+$ |

Table 5.1: Mass over charge ratios m/z for different charge states of the isotopes $^{121}$Sb & $^{123}$Sb. The table also includes species that are coinciding or have overlapping peak bases that dominate the Sb species at the respective m/z positions. The natural abundance of antimony-121 to -123 is 57.4 % to 42.6 % respectively.

by other species. For the present ion implantation beamline that leaves only the 5+ charge state as an implant candidate since it is not dominated by other generated ion species and can be implanted at high enough ion extraction voltages resulting in desired kinetic ion energies. Due to the magnetic field limitation of the 90° analyzing magnet, not all m/z values can be bent, characterized and used for implantation (see chapter 3.3). One option is to reduce the extraction voltage but this makes no sense in terms of desired kinetic ion energy and einzel lens design values. Those points rule out the singly and doubly charged antimony ions. Although argon was not deliberately introduced into ECR2, peaks at respective m/z values appeared over time, which was also observed with different sources. In the following the most commonly used approaches for the introduction of metal ions are explored to create antimony ions with our ECR sources. These include the utilization of oven techniques, gaseous compounds and insertion techniques [177].

## 5.3 Oven Technique

The first attempt was to use the same oven that was used for the EBIT source. There, it served as a reliable tool to heat up small quantities of elementary antimony pieces and introduce it into the trap region. Unfortunately this approach turned out to be not success full with ECR1. The low plasma density did not allow a sufficient interaction time with the generated antimony atoms to form antimony ions. As a result the gas injector cube which was positioned in line with the oven at the other side of the ECR source got coated with all the evaporated antimony. The high electron beam density and the fact that the ions got trapped inside the EBIT source contributed to its successful application there.

## 5.4 Volatile Organic Compound Technique

The ECR sources work well if the species of choice is supplied in gaseous form as for e.g. nitrogen. Thus, the introducing of metal ions via volatile organic compounds (VOC) seems an appealing approach which is also used by others [178–183]. VOCs are available from common main suppliers of chemicals and vary in metal species and organic composition. This results in different vapor pressures and boiling points. Those substances are usually carcinogenic and toxic, so special care needs to be taken. Here, Antimony(III)-isopropoxide ($Sb(OCH(CH_3)_2)_3$, 98 %) was chosen as a precursor. Its chemical structure can be seen in Fig. 5.1. The boiling point is 53 - 54 °C at 0.33 milibar (0.25 torr) [184]. The liquid is filled in a high vacuum sealed glass tube which is connected to a needle valve attached to the ECR1 source. Further the section between the needle valve and the chemical compound can be pumped seperately. This allows the glass tube volume to be pumped below the vapor pressure so that the majority of the supplied atmosphere consists of the VOC. In Figs. 5.2 & 5.3 magnet scans for an Antimony(III)-isopropoxide beam at low and high m/z values can be seen. The scan with argon gas supplied to the source was taken as a reference prior to switching to the volatile compound. The calculated m/z values for $Sb^{5+}$ & $Sb^{4+}$ are also displayed. A clear difference between the two scans can be seen. The argon peak intensities obviously drop since its not supplied anymore and species such as hydrogen, carbon, oxygen, water and hydro-carbon species are increased. All of the atomic species are building blocks of the VOC

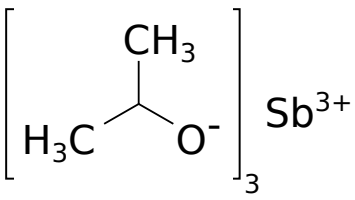


Figure 5.1: Chemical structure of Antimony(III)-isopropoxide.

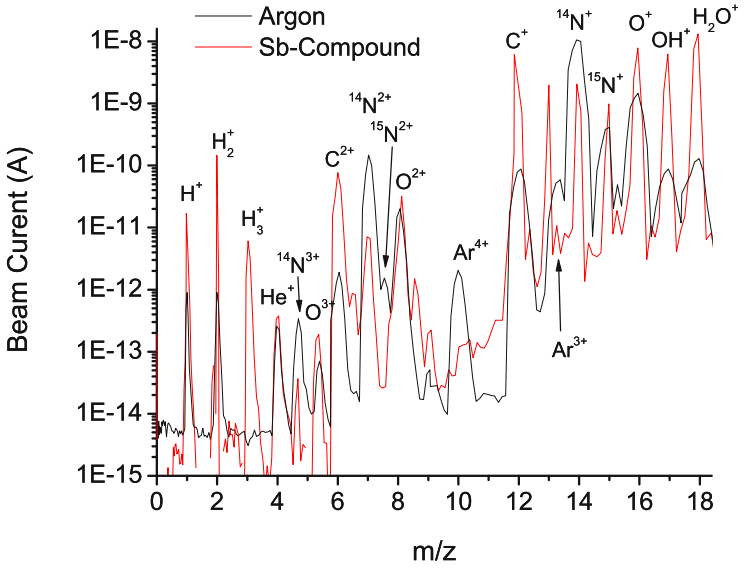


Figure 5.2: Magnet scans for argon (black) and volatile antimony gas (red). The beam extraction voltage was 5.0 kV.

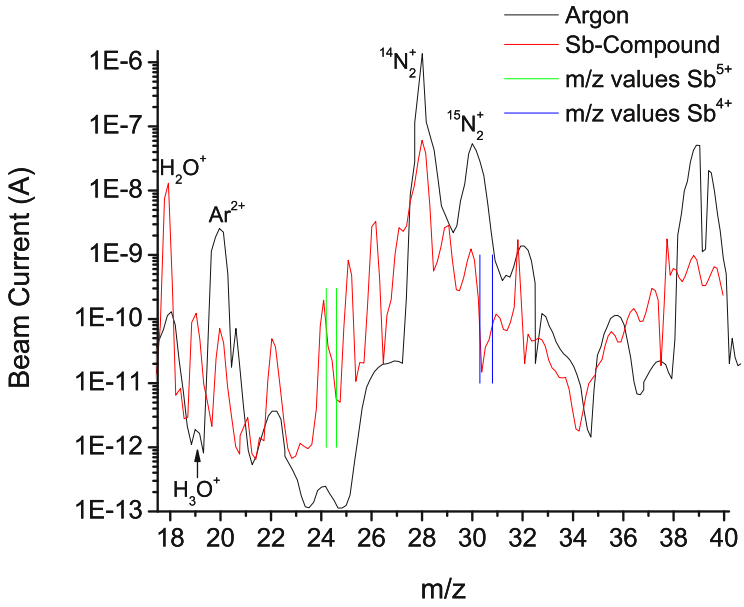


Figure 5.3: Magnet scans for argon (black) and volatile antimony gas (red). The beam extraction voltage was 5.0 kV. The expected peak positions for $^{121}Sb^{5+}$ & $^{123}Sb^{5+}$ are shown in green and for $^{121}Sb^{4+}$ & $^{123}Sb^{4+}$ in blue.

and could be decomposition products with molecular species originating from recombination processes. However, it can not be be ruled out that at least parts of the water and other carbon contaminations are introduced with the VOC or caused by a increased desorption rate from the chamber wall compared to the operation of the source with argon gas. The VOC has a purity of 98 % with unknown rest products. Water has a vapor pressure of 17.5 torr at 20 °C, which is much higher compared to the VOC. Thus it is possible that similar amounts of VOC and water were supplied to the source. Suppling water directly into the source results in a similar spectrum in terms of water and its fingerprint species. Besides the increase of ion species which could all originate from the decomposition of the VOC, no indication for the presence of $Sb^{5+}$ & $Sb^{4+}$ ions could be found. The region at $m/z \approx 24$ seems to be dominated by some hydro-carbon species that increases the initially low background dramatically. The peak has a shoulder at the high magnetic field side but non of them match the expected positions of antimony. Further, if antimony was dominating that area, indications for the $Sb^{4+}$ species should be visible too, since it should be present at a higher amount.

Again, it seems that the plasma density and the µ-wave power under which the source is operated are not sufficient to decompose the VOC in all its atomic components. Since it has not been possible to look for the singly charged antimony ion species at these extraction voltages, it is unknown whether the VOC is broken down at all or simply not enough multiple charged ions are created to raise above background level.

## 5.5 Insertion Technique

The last technique tested is the insertion of solid antimony pieces directly into the source chamber. By choosing high-purity raw material the introduction of unwanted species as with VOCs can be prevented. Antimony pieces with 99.999 % metal content are obtained and tested in two different ways. A bigger piece ($\approx 11$ mm in diameter, 4 cm in length) is mounted on a high vacuum linear motion feed-trough on ECR1, so that it can be moved in and out of the plasma area inside the source. Due to the design of the ECR2 source this is not possible there. Thus, its inner part is filled with $\approx 1$ mm sized shots along the chamber wall. In both cases nitrogen-14 is leaked to the source plasma creation.

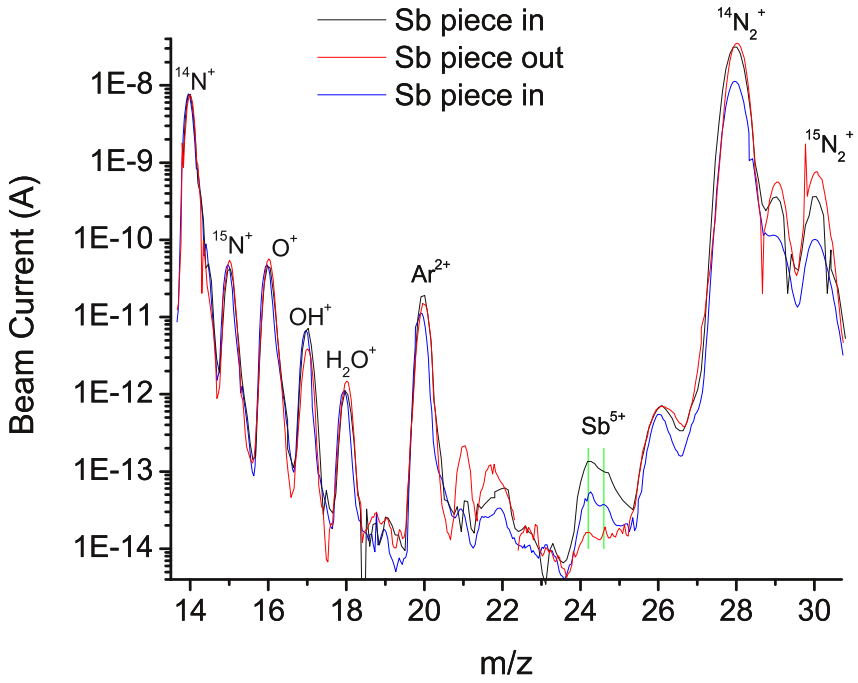


Figure 5.4: Magnet scans for the antimony piece inserted (black), retracted (red) and inserted again (blue). The x-axis is converted to mass over charge ratios (m/z). The expected peak positions for $^{121}Sb^{5+}$ & $^{123}Sb^{5+}$ are shown in green. The beam extraction voltage was 4.0 kV.

### Retractable Antimony Rod - ECR1

Fig. 5.4 shows magnet scans for the antimony piece inserted and retracted from the nitrogen plasma. The expected peak positions for the antimony isotopes are included in the graph too. Upon insertion of the antimony piece, a double peak appears at the calculated m/z values for $Sb^{5+}$. Their intensity ratio is in good agreement with the natural abundance ratio of both isotopes. The reason for the change in peak intensities for the nitrogen molecules (and $m/z = 21 \,\&\, 22$) but not for the species below $m/z = 20$ after metal insertion is not known. The magnet scan indicates that $Sb^{5+}$ is generated, although at low beam intensities. The peak intensities for lower charge states should be significantly higher and could be utilized if a higher magnetic field was available.

### Antimony Shots - ECR2

Since this source has a better design value for atomic to molecular ion species, it is also tested for the creation of antimony ions. As mentioned, for this source the antimony material is put into the source body which allows no direct in-situ comparison of magnet scans with and without antimony. Parts of the obtained magnet scan can be seen in Fig. 5.5, running a nitrogen plasma again. The m/z values for $Sb^{5+}$ are displayed in green again. As in the

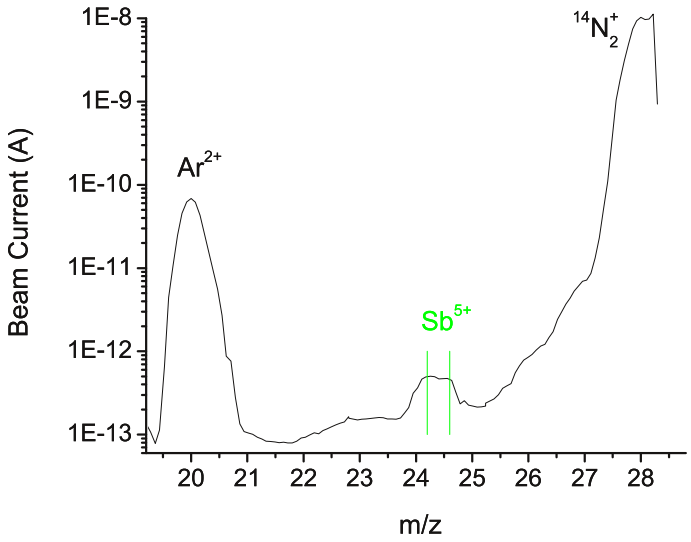


Figure 5.5: Magnet scan with new ECR source and antimony shots lying inside the source. The extraction voltage was set to 9.5 kV.

previous case, a double peak is visible at the right m/z positions indicating the creation of antimony ions.

The source was also operated at a different teststand with a more capable analyzing magnet. A magnet scan can be seen in Fig. 5.6. Nitrogen is again the source gas at a pressure of 6.8 mtorr in the source. The microwave power is 330 W and the extraction voltage is set to 5.0 kV. The most dominating peaks from previous magnet scans are again visible, i.e. atomic and molecular hydrogen, singly and doubly charged atomic nitrogen, oxygen and water finger prints and the molecular nitrogen species (m/z=28, 29 & 30). At higher mass over charge ratios impurities and other species can be seen; among them are argon (m/z=40), $CO_2$ (m/z=44), Fe (m/z=56) and acetone finger prints (m/z=58, 43). A clear double peak at mass over charge ratios 121 & 123 is visible, indicating the atomic singly charged antimony

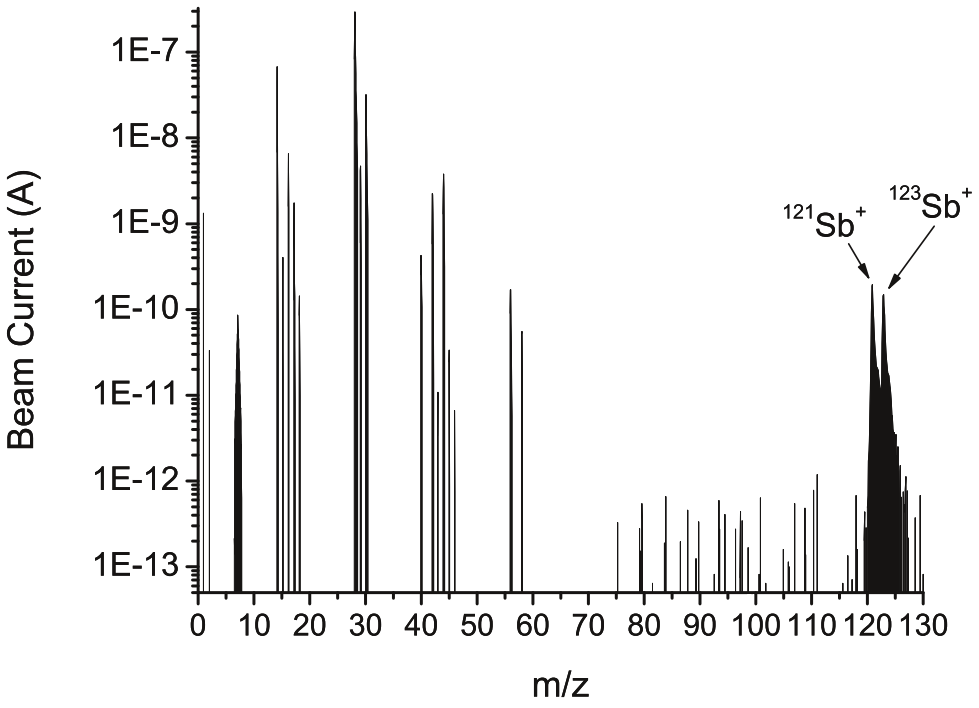


Figure 5.6: Magnet scan from ECR2 at an extraction voltage of 5.0 kV.

species. From the beam current obtained one would expect the presence of doubly charged antimony species. However, no systematic studies were done at this teststand and only the presence of the atomic antimony species confirmed.

## 5.6 Discussion & Outlook

Both ECR sources created antimony ions ($Sb^{5+}$) with the insertion technique as indicated by the magnet scans and the presence of double peaks at the proper positions. The kinetic ion energy of 47.5 keV is already sufficiently high for donor implantation into our silicon device structures.

From the work done here it seems more convenient to work with the singly or doubly charged ion species. For the present beamline this would require a redesign, including the upgrade to a more powerful magnet, a higher extraction voltage setup and switch to different einzel lens elements. Since a second beamline is being constructed for the new non-contact SPM with better ion implant precision, instead of changing the old setup, the new beamline will be designed for the implantation of lower charge states at higher extraction voltage (few

tens of kV). This allows to have two complementary fully functional ion implantation setups available at the same time.

# Chapter 6

# IBIC - SPM Tip Alignment

*This chapter describes the first integration of SPM tips, ion beams and electrical device structures and the controlled alignment of the ion beam to a defined surface feature. Ion beam induced changes in the source drain currents of field effect transistors are recorded versus SPM tip and ion beam position enabling radiation response testing of nm-scale devices with nm-resolution in the future.*

## 6.1 Motivation

The precise implantation of ions requires a controlled way to position the ion beam on the sample surface. Here, this is done as outlined in [49]. Apertures in SPM cantilever are used to collimate a stationary ion beam to a small spot size. Optionally, a second aperture can be used to pre-collimate the ion beam onto the SPM cantilever to prevent overspill and exposure of surrounding areas (see Fig. 6.1). This approach allows to scan the sample first and

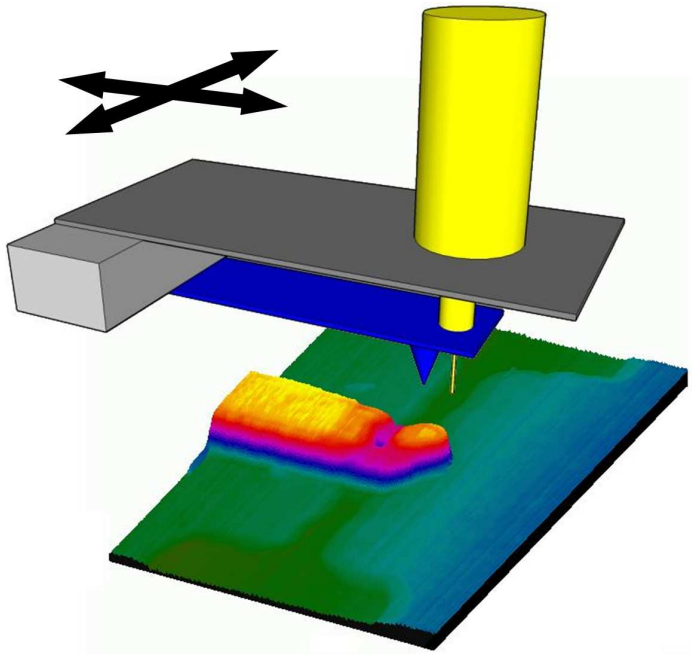

Figure 6.1: Sketch of a SPM tip with integrated ion beam [47]. A pre-collimator (dark grey) mounted above a cantilever (blue) collimates a stationary ion beam (yellow) onto the cantilever body, where a final aperture collimates the ion beam to desired ion beam sizes which can be placed on the sample depending on the SPM tip position.

then position the SPM tip in a way so that the ion beam aligns with the desired implant location. Previously, only patterns with relative alignment between spots had been demonstrated, e.g. [46, 49, 50]. If one tries to place single dopants or dopant arrays on the surface one needs the alignment of implant spots relative to the sample surface too. Although some patterns were formed next to alignment marks on the sample, this does not give an in-situ feedback since the sample has to be taken out of the implant chamber, developed or annealed and looked at again. To demonstrate the ability to place the ion beam at desired surface

positions, channel areas of field effect transistors are used as local detectors. The impinging ions can create a response in the channel current, via e.g. defect or electron hole pair creation in the target material, which then can be detected electrically. This approach is common in ion beam induced charge (IBIC) mapping with MeV ion beams. This technique can be used as a tool to investigate the uniformity of charge transport in bulk semiconductors, and the influence of extended features such as grain boundaries, precipitates and twins on charge transport [185–187]. The following sections describe the first controlled and aligned ion implantation of a device structure that also acts as a local detector using the SPM tip approach.

## 6.2 Device Fabrication

The general chip layout of all devices presented in this work can be seen in figure 6.2. On the left side, three large metal pads are visible which are used to contact the device, e.g. via wire-bonding. Metal lines go all the way across the chip to the actual device location where they connect to source, drain and gate regions. The visible numbers are device identifiers (name/ID and channel dimensions) which are incorporated into the fabrication process.

Figure 6.2: Optical microscope image showing the typical chip layout of the used devices, in this case a FinResistor (see chapter 7.3). The standard chip size is $25 \times 2\,\mathrm{mm}^2$.

FinFETs[1] are fabricated in 250 nm thick SOI which consists of 50 nm natural silicon on buried oxide with an overgrown 200 nm $^{28}$Si epi layer ($^{28}\mathrm{Si} > 99.9\,\%$). A 100 nm thick low temperature oxide layer is deposited to serve as a hard mask for the silicon etch. Source/drain pads and channel (fin) regions are defined by electron beam lithography. Channel widths range from 30 - 250 nm. After the silicon etch, a 10 nm thick gate oxide is grown on the sidewalls ($\approx$ 70 nm on top of fin). In situ phosphorus-doped polycrystalline silicon is deposited as the gate electrode material with a thickness of 140 nm. Gates of 280 nm length are patterned by e-beam lithography and poly silicon dry etching. Self-aligned arsenic implants (25 keV, $2\times10^{15}/\mathrm{cm}^2$) are used to form source/drain regions. Low-temperature chemical-vapor deposited silicon dioxide (LTO) is used as an interlayer dielectric (capping layer for the fin region) with a

[1] A detailed description of the device fabrication can be found in refs. [188] & [189].

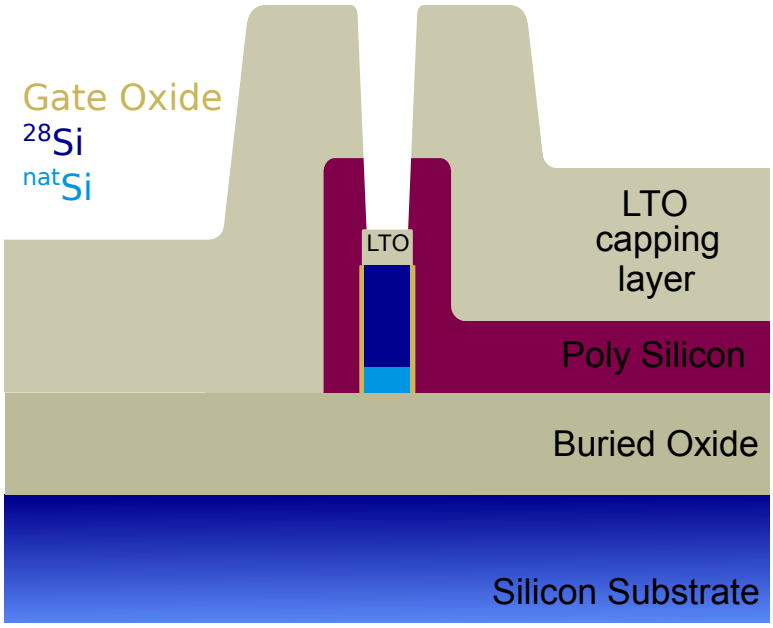


Figure 6.3: Layout of a FinFET device (after hole drilling process). The cross section is along the y-axis through the gate electrode and cuts perpendicular through the silicon fin (see Fig. 6.4).

thickness of 300 nm. Contact regions are etched and tungsten is used for metal contacts. Devices are annealed in forming gas ($N_2/H_2$ - 90 %/10 %) at 400 ° for 20 min to passivate defects at the $Si/SiO_2$ interface and to improve the metal-semiconductor contact quality. A sketch of the device can be seen in Fig. 6.3. It displays a cut through the center of the channel in direction of the gate electrode. Source and drain contact areas are not displayed and the current direction is perpendicular to the plain. Fig. 6.4 shows a SEM picture of the FinFET before LTO film deposition. The source and drain SOI leads from the metal contact pads (not displayed) to the channel region are visible, as is the phosphorus-doped polycrystalline silicon gate electrode wrapped around the fin of the device. In order for the low kinetic energy ions to reach the channel area, parts of the LTO layer and gate electrode needed to be removed. For that, a dual beam focused ion beam (FIB) system is used and a hole above the fin of the transistor is opened up. First, parts of the LTO layer are removed with a 30 keV $Ga^+$ ion beam. Then focused electron beam (5 keV) induced etching with $XeF_2$ etch gas is used to drill further into the remaining LTO parts and into the poly silicon gate electrode. The electron beam is turned off for the last part of the etch since $XeF_2$ alone does etch silicon but not silicon oxide [190, 191]. This should lead to an undamaged and exposed gate oxide layer

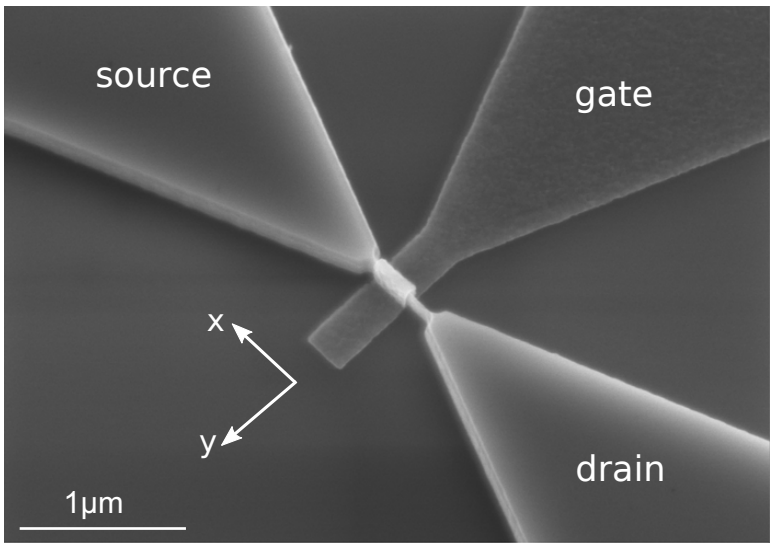


Figure 6.4: SEM image of a FinFET during device fabrication. The channel area which is etched into the SOI and the gate electrode wrapped around the fin are visible and not covered in LTO yet. [47]

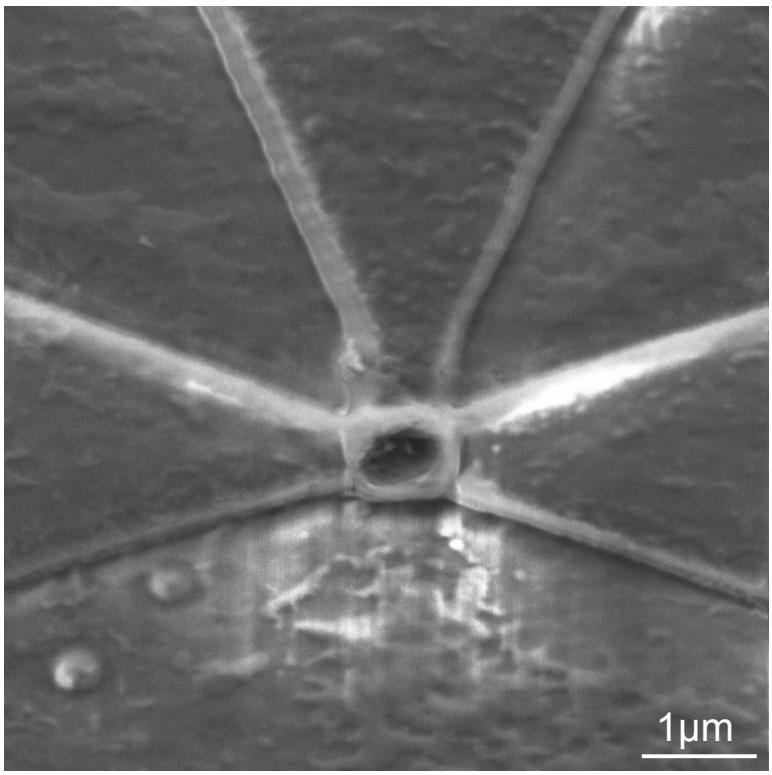


Figure 6.5: SEM image of a FinFET after device fabrication and FIB surgery.

on top of the fin (see Fig. 6.3). After FIB processing, the devices are annealed in forming gas ($N_2/H_2$ - 90 %/10 %) at 400 ° for 20 min to cure damage and recover device performance. A SEM image of the FinFET after FIB processing can be seen in Fig. 6.5. To what extend the side electrodes were left untouched, and the exact device structure after the FIB processing could not be resolved from the SEM images. Important is that the FinFETs do not show any gate leakage after FIB processing (see Fig. 6.6) and channel currents respond to ion impacts.

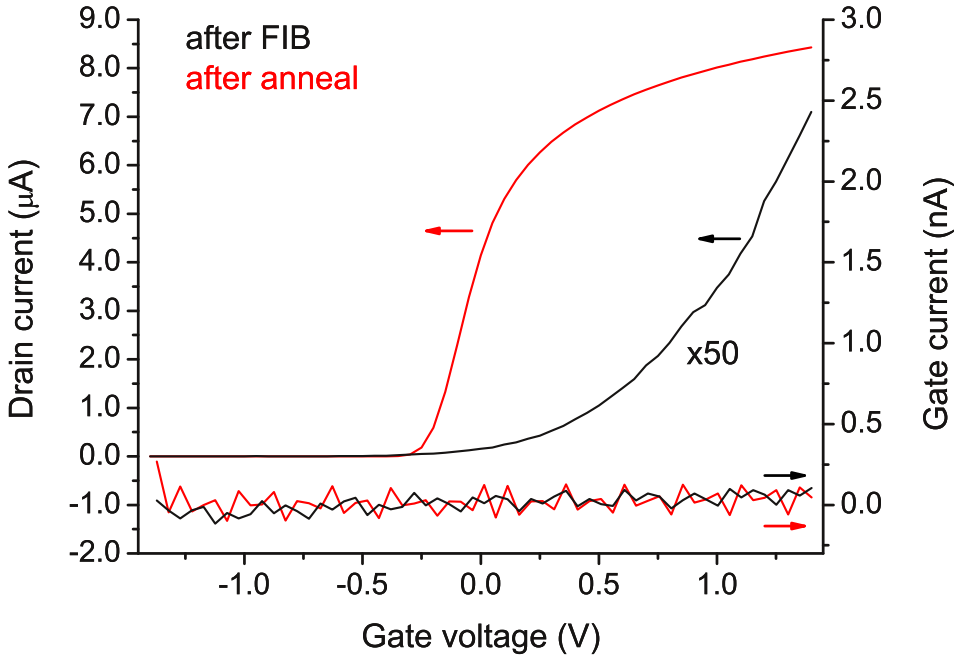


Figure 6.6: IV-curve of FinFET after FIB processing and after forming gas anneal ($V_d$ = 0.2 V) [47].

Electrical device performance is recovered after the anneals (see IV-curve in Fig. 6.6) and is similar to pre-FIB values. Note that the data after FIB processing is multiplied by a factor of 50. Gate leakage currents are below 200 pA.

## 6.3 Measurement description

The FinFETs are mounted in the ion implantation chamber with the SPM setup. Argon ions are produced with the ECR1 source and $Ar^{3+}$ (36 keV) and $Ar^{2+}$ (20 keV) ions are extracted and focused onto the sample. At those energies the ions have a mean lateral range of 44 nm and 26 nm in silicon dioxide respectively (see Fig. 6.7) which means that most of the ions get stuck in the LTO layer and do not reach the device layer. This is sufficient for the purpose of demonstrating these first aligned ion implantation tests. Despite the shallow implant depth, the device is sensitive enough to those ion impacts, changes the electrical device characteristic and can be used as a local sensor. Pulsing of the ion beam is achieved by applying a voltage

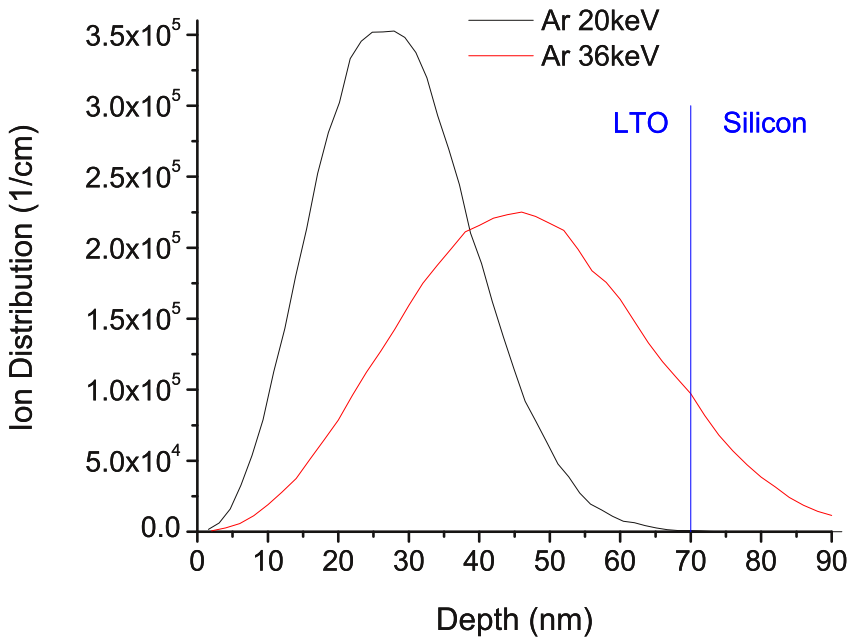


Figure 6.7: SRIM simulations for argon ions implanted into the FinFET device structure at 20 and 36 keV [116]. The y-axis corresponds to the conversion factor to obtain the ion concentration (atoms/cm$^3$) at each given depth for a certain implanted ion fluence (atoms/cm$^2$).

onto a deflector plate parallel to the ion beam trajectory. The devices are operated at above threshold at a gate bias $V_g = 1.0\,V$, a drain bias $V_d = 0.8\,V$ and with the source grounded, resulting in drain currents of approximately 10 µA. The drain current signal is recorded after amplification with a current amplifier (Stanford Research 570) and all measurements are performed at room temperature. Implant apertures are drilled in the cantilever body of an

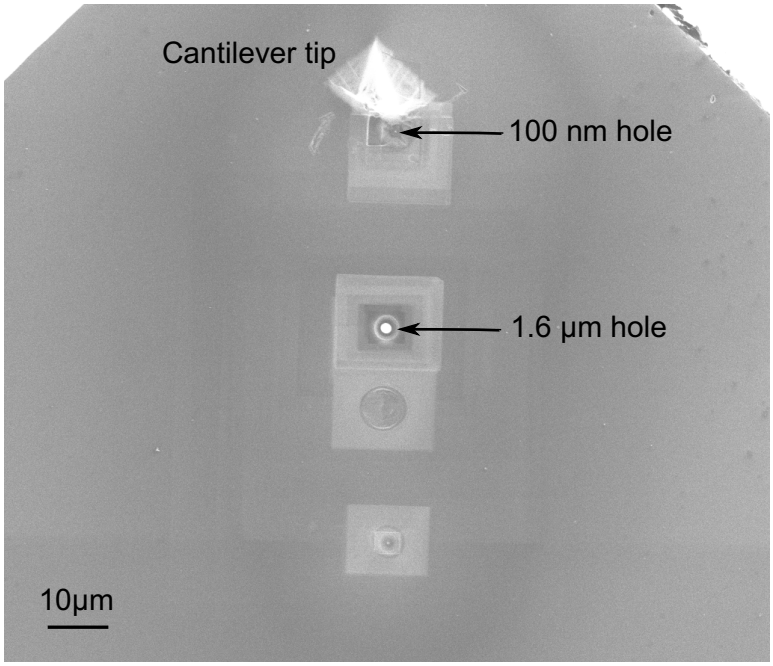


Figure 6.8: SEM image of the SPM tip with 1.6 µm and 100 nm holes.

SPM tip. The locations of the 1.6 µm and 100 nm holes in respect to the SPM tip can be seen in Fig. 6.8. The tip is aligned to the device region with the coarse stage (see Fig. 6.9) and then the sample scanned with the xyz piezo stage. An SPM image can be seen in Fig. 6.10. The hole in the FinFET could not be resolved nicely with the SPM system due to tip blunting in contact mode. Then an offset in x- and y-position is applied so that one of the drilled holes in the SPM cantilever aligns with the hole in the FinFET (x-direction is along the source-drain electrodes and the y-direction is along the gate electrode, see Fig. 6.4). The offset distances and directions are obtained from the SEM image (see Fig. 6.8). The tip is then moved along each spot of a square point grid. At each spot, the drain current is measured over time and the argon ion beam is turned on for a few seconds after a short dwell time in which no ions hit the sample. The SPM tip position and drain currents are recorded at each position. The SPM and ion beam exposures are controlled via a Labview program [193]. The total change in the drain current within each interval is plotted versus x- and y-position of the SPM tip to generate the maps of current responses.

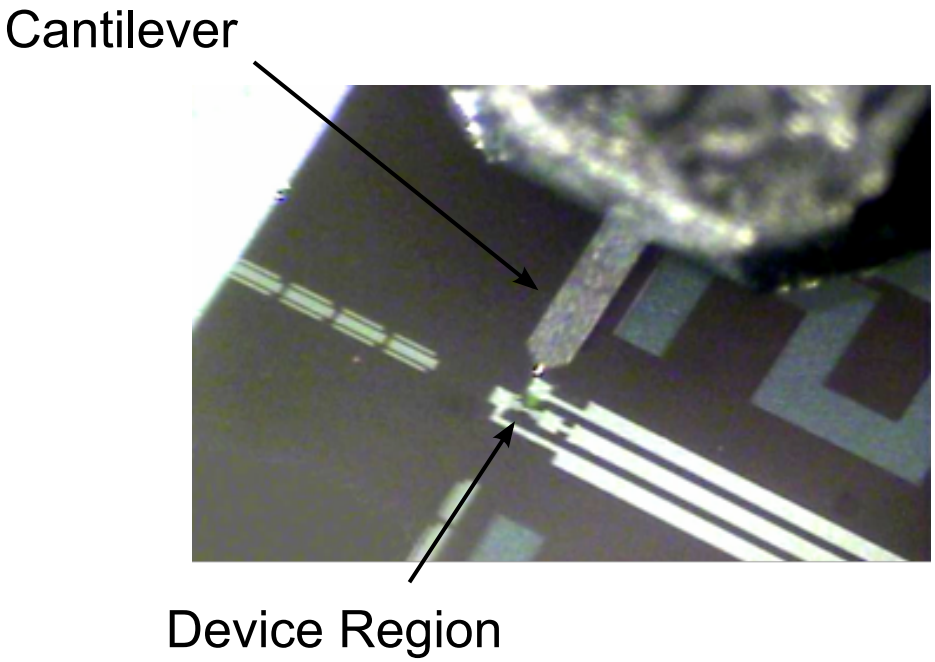


Figure 6.9: Optical image taken through the viewport of the implantation cube during the coarse alignment of the SPM tip.

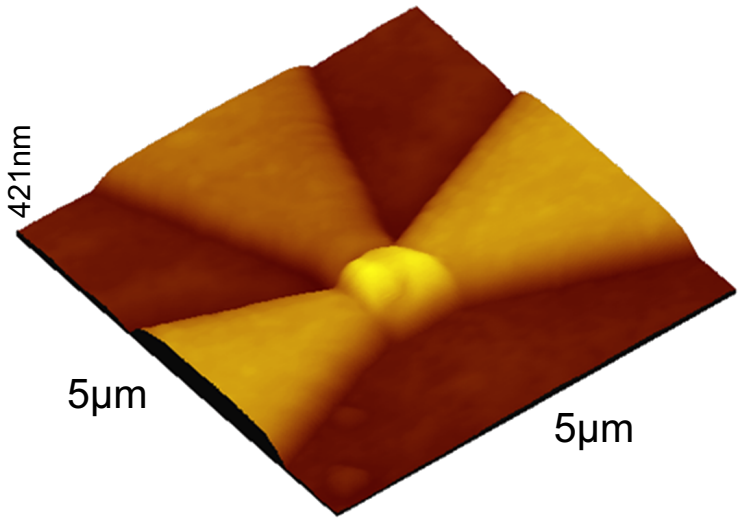


Figure 6.10: SPM image of the FinFET [47, 192].

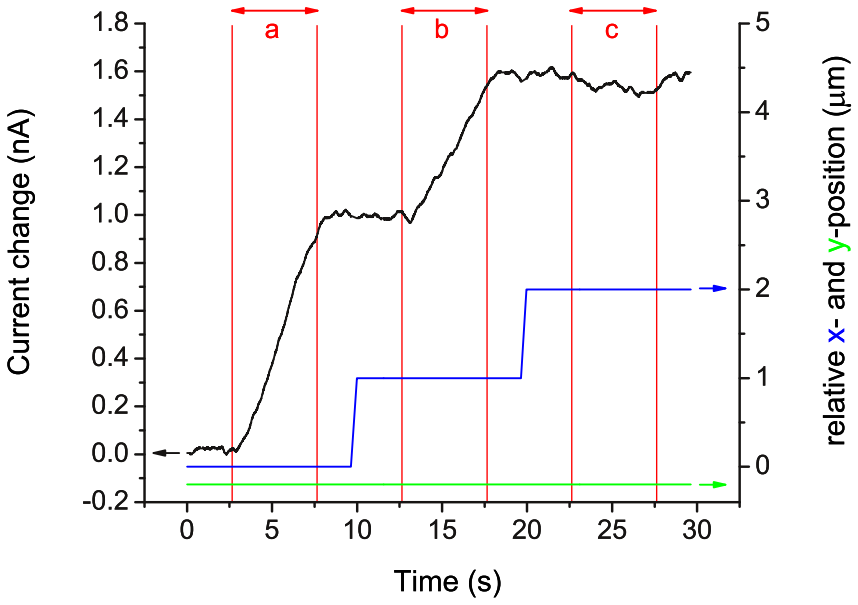


Figure 6.11: Example of the absolute change of the source-drain current depending on the x- (blue) and y-positions (green) of the SPM tip. The sample gets exposed to the ion beam in the labeled intervals. [47]

## 6.4 Results

First, the 1.6 µm hole is used to collimate the 36 keV argon beam to test the response of the device current. The data of three consecutive exposure spots of the scanning sequence is displayed in Fig. 6.11. The argon ions hit the FinFET during intervals which are indicated with arrows. The y-position is kept constant and the x-position is changed by 1 µm in between spots. Intervals (a) and (b) show an increase in drain current. No such increase, just the fluctuation of the channel current, can be seen in interval (c). In cases (a) and (b), the tip is at a position in which ions hit areas that resulted in an increase in drain current (LTO layer above fin). This is due to the fact that ion hits can form positively charged defects in oxides which alter transistor currents [194]. Those positive oxide charges reduce the threshold voltage of the device and lead to an increase in the effectively applied gate voltage and thus increase the device current. The three data sets were obtained when the beam was initially aligned to the gated source-drain region and moved away from that active region. Ions that hit areas that are not changed by the FIB process and that are still covered with the LTO capping layer have no effect on the channel current. They create defects too far away to have

any detectable influence. A full map of channel current changes versus ion beam positions is shown in Fig. 6.12. Data from $21 \times 21$ spots are recorded in a $20 \times 20\,\mu m^2$ area. The exposure time is 5 s for each spot. On average, $\approx 600$ ions/s/$\mu m^2$ hit the sample (calculated from current reading of the sample and area of aperture in the SPM cantilever). The peak at the locations that show changes in the source-drain current is clearly visible. The beam spot is larger than the distance between consecutive spot locations, therefore, nearest neighbor spots contain responses from the same device area. The beam diameter is fairly large compared to the dimensions of the source-drain channel. In order to obtain more accurate maps of the channel region, we collimate the beam with a second hole in the SPM cantilever which is $\approx 100$ nm in diameter.

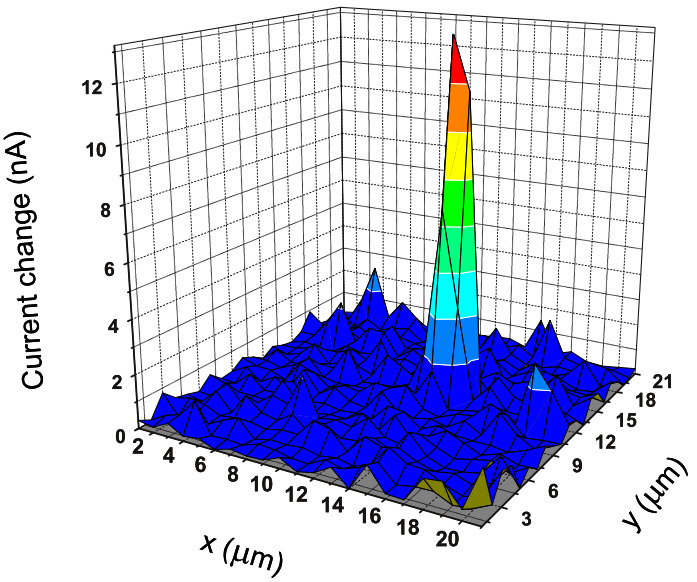


Figure 6.12: IBIC map obtained with an argon beam collimated by a 1.6 µm hole in the SPM lever. [47]

Fig. 6.13 shows one of the IBIC maps obtained with 20 keV argon ions. The exposure time is set to 30 s per spot and the beam fluence rate is $\approx 1500$ ions/s/$\mu m^2$. The distance between spots is 200 nm and $16 \times 16$ spots are exposed within a $3 \times 3\,\mu m^2$ area. The ratio of signals from areas which respond to the ion beam to surrounding areas is smaller than in Fig. 6.12. The fluence rate of the 20 keV ions is 2.5 times higher than for the 36 keV ions. Accounting the differences in fluence rates and the deposited energy per ion in the silicon oxide, the

total deposited energy per unit area is similar for both ion energies (SRIM simulation [116]). With an average creation energy for electron hole pairs of 18 eV in silicon oxide [195], similar responses of the device current to both ion beams are expected. The smaller response can be

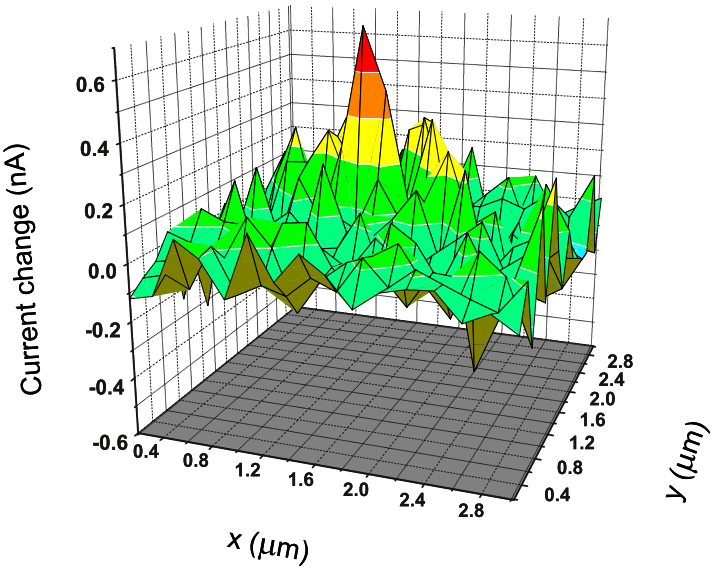


Figure 6.13: IBIC response recorded with an argon beam collimated by a 100 nm hole in the SPM lever. [47]

explained by the difference in the hole sizes in the cantilever and thus beam spot sizes hitting the device. In the case of the smaller hole, only parts of the total area which leads to changes in the device current are exposed, whereas beam spots collimated with the larger hole expose most of the entire ”active” area at once. In both circumstances, four beam positions resulted in a channel current response. The large hole beam spots are overlapping whereas the small hole beam spots are separated. From that, the active area can be estimated to be around 400 - 600 nm in side length.

## 6.5 Discussion

The estimated area that responds to ion impacts is larger than we would have expected from the fin dimension of $100 \times 280\,\mathrm{nm}^2$. Relatively high ion fluence rates are needed to observe changes in the channel current. This leads to the conclusion that the 70 nm thick gate oxide indeed stayed (mostly) intact during the FIB process as intended and that most of the low kinetic energy ions stopped far away from the device and did not reach the channel. Thus, impinging ions have created positively charged defects too far away to efficiently affect the device currents. To prevent this, future device generations will be made more sensitive to ion impact sensing. The unwanted step of post device processing via focused ion beams is and will be avoided by designing the devices differently, with the additional option to incorporate the ion implantation step during the device fabrication. These experiments with the FinFETs and current SPM setup are just a prove of principle and helped to get aware of certain issues that need to be addressed for future high precision implants with few nanometer accuracy.

First off, scanning the device with the SPM system and then shifting the SPM cantilever by the tip-aperture distance acquired from a cantilever SEM, so that the ion beam lines up with the exact implant location will be challenging. This requires that one knows the tip to hole distance very accurately (within nanometer) from the SEM image and that the tip apex does not change its shape during the SPM imaging process. Using a non-contact SPM system will help in that respect. Further, the location of the hole next to the SPM tip is not ideal. Drilling the hole through the tip cone will be helpful. Thus, the distance between aperture and the tip apex will be minimal and necessary tip-aperture corrections in the range of micrometers prevented. This will also bring the hole closer to the sample and avoids implant uncertainties due to the divergence of the ion beam. For a beam divergence of only $0.5\,^\circ$ and an aperture sample distance of 5 µm this would yield a broadening of the ion beam by 44 nm on the sample, which would negate the benefit of using few nanometer sized implant apertures.

One thing to consider is that one could actually not use the imaging function of the SPM system at all for aligned implantations. The area susceptible to ion impacts could be mapped out by the use of noble gas ions. After this step, the tip could be moved to the desired implant area based on this map of device current responses alone and not based on the SPM image. There, the donor ion could be implanted then. The additional damage caused by the nobel gas ions in the device would be healed during the anneal which is necessary to electrically activate the donor(s) in the silicon matrix.

In summary, the experiments demonstrate nicely the previously outlined capability of scanning probe aligned ion beams [49,50]. The full sequence of device imaging and implantation of device regions is shown for the first time with this technique. This is an important step towards the goal of precision ion implantation and can act as an in situ calibration method or radiation response testing technique of nm scaled devices in the future.

## Acknowledgments

The author thanks Cheuk Chi Lo for supplying the devices, Andreas Schuh for writing the labview code to record the ion beam response of the FinFETs and Thomas Schenkel for the FIB processing of the cantilevers and FinFETs.

# Chapter 7

# Detection of Single Ion Impacts in Silicon Device Structures

*This chapter demonstrates the detection of single ion impacts in silicon FETs and silicon wires at room-temperature via changes in device currents. The device sizes range from a couple of micrometers to sub-micrometers. This validates the detection method and allows its application to devices with potential single spin readout capability.*

## 7.1 Motivation

As outlined in chapters 1.1 and 2.5, the ability to place single ions could enable the study of single dopant effects in conventional CMOS devices [36–39] or the fabrication of new single atom device structures. One way to achieve this task of single dopant placement is via scanning transmission microscope patterned hydrogen terminated silicon surfaces [63, 64]. After locally desorbing hydrogen atoms from the surface via STM, phosphorus atoms from adsorbed phosphene molecules are incorporated into the silicon lattice below the surface. Deeper donor placement requires the overgrowth of the devices surfaces. A more common and versatile method to place (single) ions into devices is ion implantation [44–46, 55, 56, 58–60]. One can implant into partially fabricated or finished device structures followed by a rapid thermal annealing step to electrically activate those donors.

Timed ion implantation through apertures will yield a Poisson distribution of the implanted donor atoms. As a result many devices need to be screened to find the singly implanted ones via characteristic device behavior. If one tries to implant arrays of single donor atoms, then timed ion implantation becomes not viable anymore. The chance for the timed implant to yield a device with desired implant pattern will drop exponentially with array size. At that point the ability to place single atoms becomes essential.

First proof of principle experiments are conducted with µm sized planar FETs to demonstrate the detection of single ion impacts via changes in the channel current of transistors at room-temperature. After the successful demonstration of single ion hit detection, sub µm-sized silicon wires (FinResistors) are fabricated in SOI to validate an increased single ion hit response. Further, they can act as geometrically well defined detectors for SPM precision implant tests (as in chapter 6) and are candidates for single spin readout via EDMR experiments using spin dependent recombination [141, 196–198] or trapping [145, 199].

The work on the single ion impact detection method as described here, can also be used to estimate the single ion implant compatibility of other device geometries. Donor atoms in field effect transistors are not the only device layouts of interest. Device structures like quantum dots are other promising candidates and may be fabricated in the same material systems. The application of the here demonstrated sample behavior allows the planning and design of other single ion implantation compatible device layouts.

## 7.2 Single Ion Impact Detection Mechanisms

In order to implant single ions one at a time, one must detect each of the single ion impacts (SII) with a high fidelity. This task is even made more difficult by the fact that, for reasons of ion placement accuracy and shallow implant depth, ions low in kinetic energy are desired. The lower the kinetic ion energy the smaller the range straggle in the host lattice and thus the more precise the implant location is known. Depending on the ion species and desired implant depths the implant energies are around a few tens to below 100 keV. At those energies single ion detection is considerably harder compared to impact detection of high kinetic ions (MeV), e.g. via the detection of secondary electrons [200–202]. Single ion detection at low kinetic energies has been demonstrated via the generation and collection of electron-hole pairs at low temperatures [45, 57–59] and also via the collection of secondary electrons [44, 55, 56]. Both approaches entail certain challenges that would need to be overcome to make them compatible with our device layout and implant strategy. The collection of electron-hole pairs would require the cooling of the devices and SPM stage during the implantation process. Further a modification of the device layout might be necessary to be sensitive enough to single ion hits. For the secondary electron detection approach, the electrons would need to be collected on the bottom side of the SPM cantilever. Another option would be to guide them away from the ion impact region, along the gap between sample and cantilever, to a detector next to the cantilever. For reasons of ion placement precision (see section 6.5), the implant aperture will need to be placed close to the apex of the SPM cantilever tip most likely. In that case one would need to collect the secondary electrons through the implant aperture on the other side of the cantilever. Both approaches to detect single ion impacts constitute experimental challenges.

To circumvent the described obstacles, a new method is explored here which detects single impacts of ions low in kinetic energy via changes in device currents at room-temperature. This is an extension of the known fact that single high energy (MeV) ions can alter electrical device performances [201–207]. As mentioned in chapter 1.3, we use device currents in our silicon FETs in order to measure the spin state of donor ions via electron paramagnetic resonance measurements (see figure 1.2). The idea is to use the same currents to detect single ions impacts. By doing so, no or moderate changes only need to be made to our device layout. Since our devices would act as the single ion detectors themselves, no exterior setup is needed that would complicate our implant strategy with SPM aligned ion beams.

## 7.3 Device Layout and Fabrication

In this section the fabrication of the two device types are described.

### Planar µm-sized FETs in bulk silicon

FETs are fabricated on natural silicon (100) wafers with undoped (n-type, >1 kΩcm) substrates for the formation of accumulation mode (a-FET), and p-type (≈1 Ωcm) substrates for the enhancement mode (n-FET) devices, respectively. Global alignment marks (LTO/SiGe) are formed on top of the silicon substrates followed by deposition of a wet-oxide. Source-

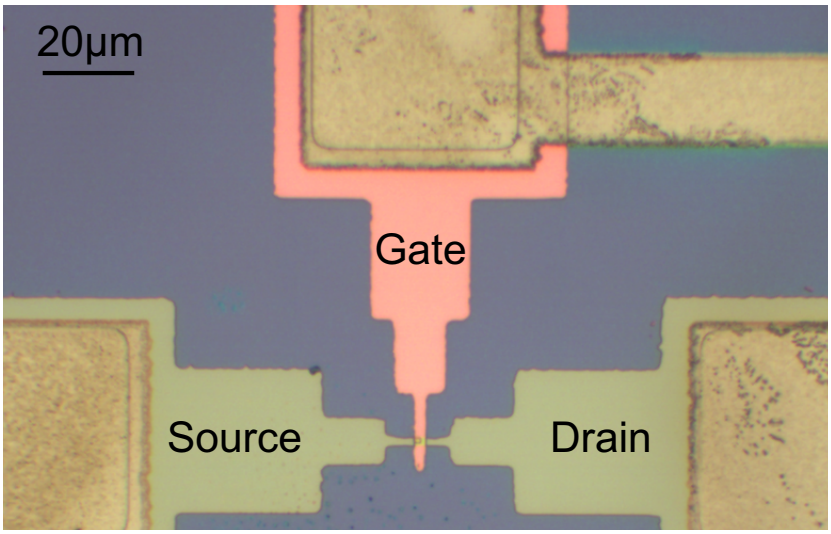


Figure 7.1: Optical image of device region of an a-FET.

Drain areas and $2 \times 2\,\mu m^2$ channel areas are defined by an oxide etch step. A 20 nm gate oxide is grown and in situ phosphorus doped poly-silicon is deposited and patterned as the gate electrode with a thickness of 160 nm. A high dose arsenic implant ($5 \times 10^{15}/cm^2$, 40 keV) is then performed to form degenerately n-type doped source/drain regions. LTO is used as an interlayer dielectric layer with a thickness of 300 nm. Contact regions are etched and tungsten is sputter deposited to complete device metallization. A $N_2/H_2$-forming gas anneal at 400 °C for 20 min is performed to passivate defects at the $Si/SiO_2$ interface and to improve the metal-semiconductor contact quality. Following electrical testing, devices are processed in a dual beam focused ion beam (FIB) system. Here, apertures with areas of 0.1 - 1 $\mu m^2$ are opened in the passivation layer and poly-silicon gate to allow implantation of low energy dopant ions into transistor channels. As for the devices in chapter 6, a 30 keV $Ga^+$ ion beam is used to remove parts of the LTO layer. The remaining LTO is removed by electron beam

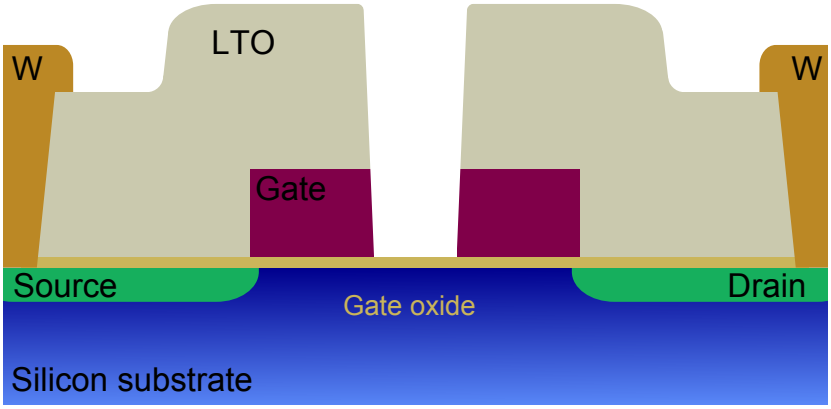


Figure 7.2: This figure shows the device layout of the used FETs after FIB processing. The cut of the cross section is along the source-drain region of the device. The LTO and gate electrode layers are removed exposing the gate dry oxide on top of the device channel. Tungsten metal electrodes contact the $n^+$-regions.

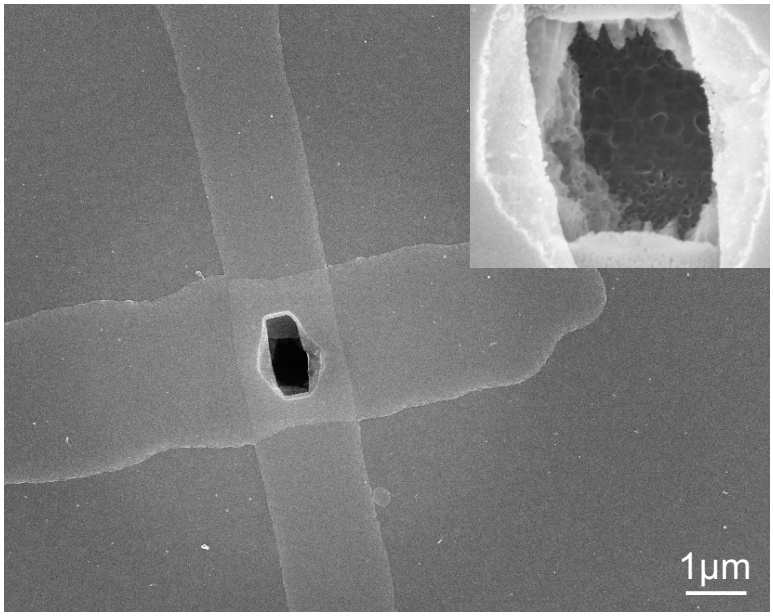


Figure 7.3: SEM image of an a-FET device with a channel area of $2 \times 2$ µm$^2$ during FIB processing. The hole drilled through the LTO layer into the gate electrode can be seen clearly. The source drain channel is oriented vertically and the gate electrode comes in from the left side. The inset shows the drilled hole at a higher resolution.

assisted etching with 5 keV electrons and $XeF_2$ [191]. The use of e-beam assisted etching avoids excessive damage to channel regions caused by Ga ions and forward scattered silicon recoil atoms. Following the removal of the LTO and parts of the poly-silicon layer, the electron beam is turned off, and etching by $XeF_2$ gas alone leads to the formation of apertures in the poly-silicon gate. Since $XeF_2$ does etch silicon but not $SiO_2$ [190] the gate oxide acted as an effective etch stop for this process. Following FIB processing, devices undergo another forming gas anneal at 400 °C for 30 min. Electrical testing validate device integrity, and FETs are then mounted in our setup for ion implantation with scanning probe alignment. Figure 7.4 shows an in situ scanning probe image of an a-FET in its final processing stage with source, drain, and gate electrodes as mounted in the implant chamber. The device is then ready to be tested for ion impact responses.

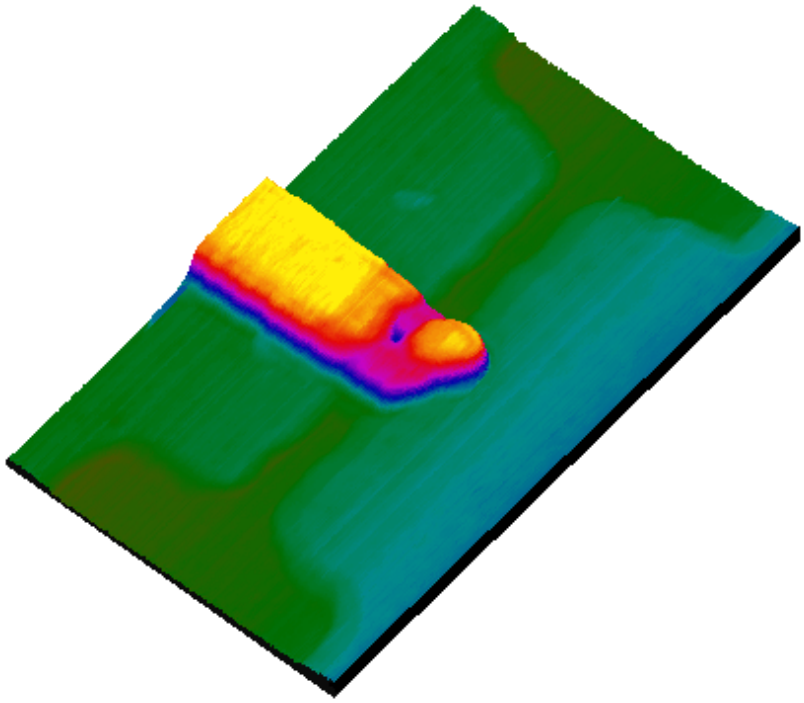

Figure 7.4: In=situ scanning probe microscope image of a µm scaled a-FET with $2 \times 2$ µm$^2$ channel region. The scan size is $10 \times 18$ µm$^2$ and the full z-scale is 1.35 µm. Source-Drain regions are shown in dark green. The hole which was drilled via FIB processing can be seen in the gate electrode above the channel area. [46]

### Sub µm-sized FinResistors in SOI

The FinResistors fabrication process follows an adapted recipe from the FinFETs. The main modifications are an final etch step to lay free the fin of the device and an unconnected but nearby terminated gate electrode. This enables post processing capabilities to gate the device, e.g. via FIB assisted deposition of metal films (from the terminated gate to the fin) where only a small area can be covered with metal in a convenient time frame. An optical microscope image showing the device area of the FinResistor can be seen in Fig. 7.5, the device layout in Fig. 7.6. Two of the metal electrodes make contact to $20 \times 20$ µm$^2$ SOI pads. Those pads

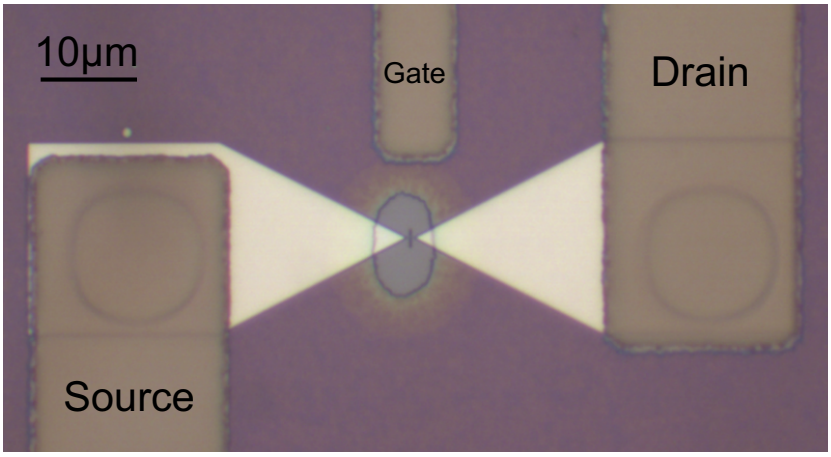


Figure 7.5: Optical microscope image of the larger device area.

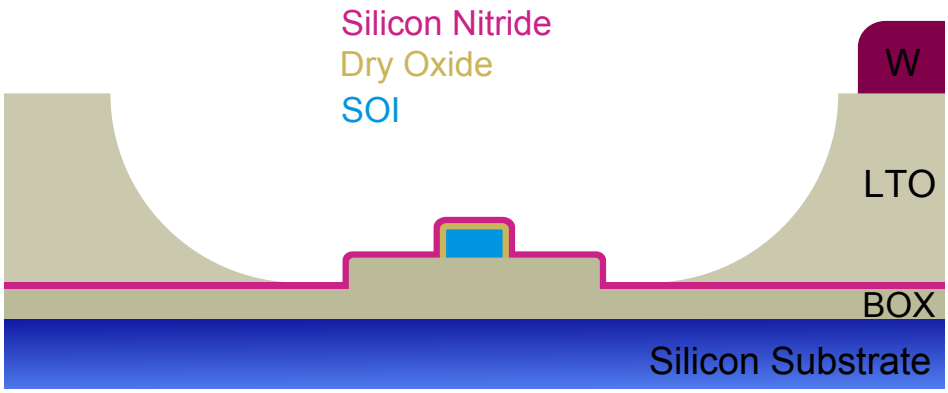


Figure 7.6: Device layout of a FinResistor. The cut of the cross section is along the spare electrode to the center of the device right through the silicon fin (see Fig. 7.5). The current direction is perpendicular to the plane.

narrow down to the center of the image and are connected via a small silicon channel. The third electrode is not connected for those devices and acts as a spare electrode for eventual future needs. In the case of a field effect transistor this (then connected) electrode serves as the gate electrode. The etched hole into the interlayer dielectric layer (LTO) is clearly visible in the center, making the FIB processing step as it is needed for the FETs unnecessary. The exposed silicon fin of the device can be reached easily by ions low in kinetic energy.

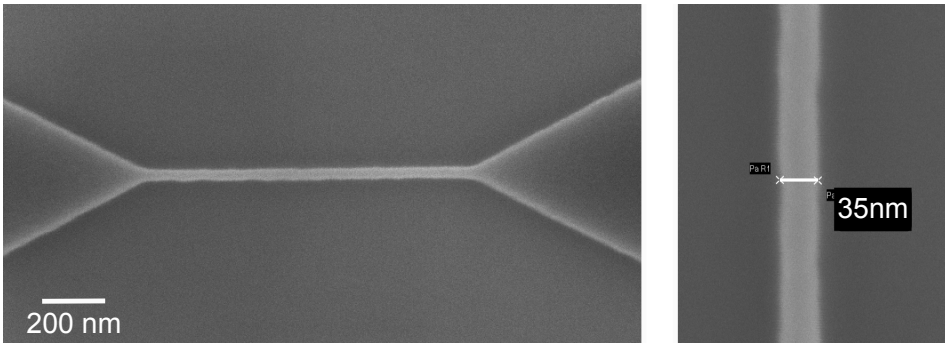


Figure 7.7: SEM picture of a FinResistor during device processing after the SOI etch. The image shows the silicon fin and the ends of the triangles that lead to the $20 \times 20$ µm$^2$ contact pads. The smallest FinResistors that were obtained are $\approx 35$ nm in width.

The FinResistors are fabricated in 50 nm SOI on a 100 nm buried silicon oxide layer on silicon substrate. The SOI is implanted with 40 keV $^{121}$Sb ions at a fluence of $3 \times 10^{11}$/cm$^2$. Global alignment marks for optical and e-beam lithography are etched into LTO/SiGe (100/550 nm) layers. The fin and connecting $20 \times 20$ µm$^2$ sized contact pads are written into negative e-beam resist followed by a dry etch step to transfer the patterns into the SOI layer (see Fig. 7.7). Fin widths range from $\approx 35$ - 200 nm. The SOI structures are overgrown with a 10 nm thick dry oxide layer. A second e-beam lithography step defines 300 nm wide rectangular structures in a new layer of e-beam resist (see Fig. 7.8a). The resist structures block certain areas of the fin from the following n$^+$-implant ($^{75}$As, 25 keV, $2 \times 10^{15}$/cm$^2$) to keep that area (n$^+$-) dopant free and to protect the dry oxide layer. In order to easily find this area of the fin, a short wet etch is performed to transfer the area blocked by the e-beam resist into the BOX material (see Fig. 7.8b). A 10 nm thick layer of silicon nitride is deposited onto the whole structures following the removal of the rectangular e-beam resist. A LTO layer of 300 nm thickness is deposited followed by etching holes to the $20 \times 20$ µm$^2$ contact pad areas. Following an etch to remove the nitride layer, a 320 nm thick layer of tungsten is sputter deposited onto the whole wafer and metal electrodes are patterned via a tungsten etch step.

Then, µm-sized holes are wet etched into the LTO layer to expose the fin. As a last step, the devices are annealed at 400 ℃ for 20 min in forming gas before they are diced up into individual chips. The final devices can be seen in Fig. 7.9 & 7.10 which show insitu SPM scans of a device with a 100 nm wide fin.

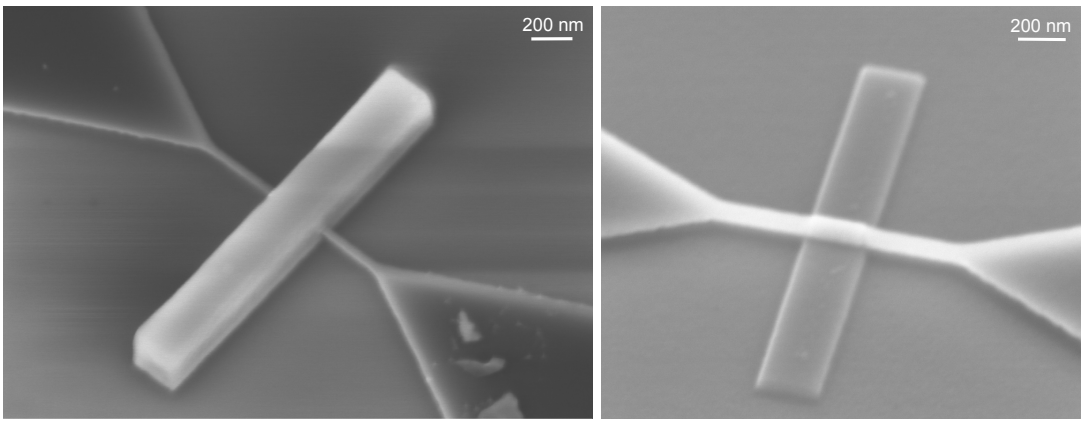


(a) After $n^+$ implantation. (b) Final device.

Figure 7.8: SEM image of FinResistor during and after device fabrication. During the $n^+$ implant, photo-resist covers parts of the fin to create the "active" region. Following a short oxide etch and removal of the photo-resist the position of the $n^+$ free region can be easily located. Extending wings in the BOX material and a slightly thicker fin due to the still intact dry oxide indicate the region which was covered during the arsenic implantation.

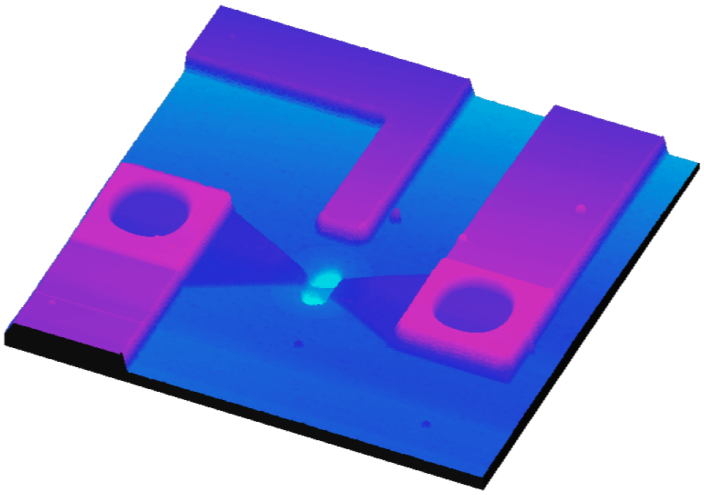

Figure 7.9: SPM image of a FinResistor device showing the (final) device region as in Fig. 7.5. The scan area is $90 \times 90\,\mu m^2$. The full z-scale is 920 nm. The source & drain electrodes, the spare electrode and the fin region can be clearly seen.

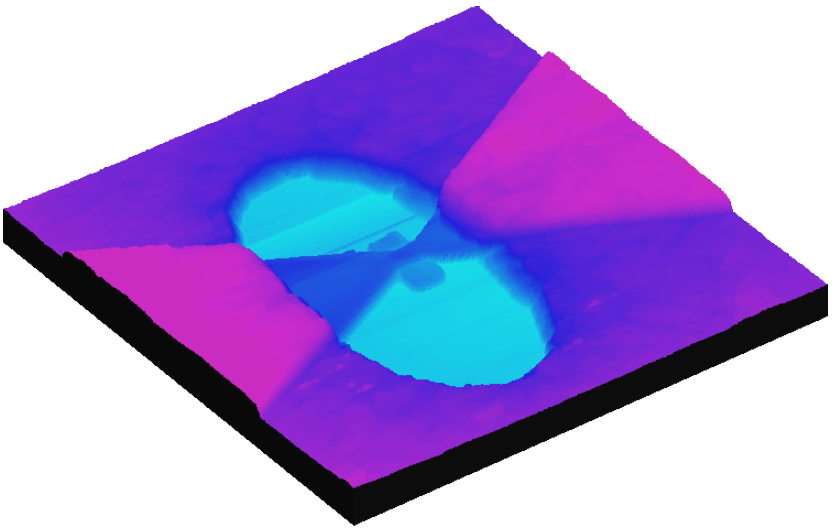

Figure 7.10: SPM image of a FinResistor after device fabrication. The scan area is $15 \times 15\,\mu m^2$ and the full z-scale is 422 nm.

## 7.4 Results

### Planar µm-sized FETs

To study the ion impact response of the planar devices, antimony and xenon ions are extracted from two ion sources. With the ECR1 source, $Xe^{6+}$ ions at 50 keV kinetic energy are generated and $Sb^{14+}$ 70 keV ions with the EBIT source to ensure shallow implantation depths. The

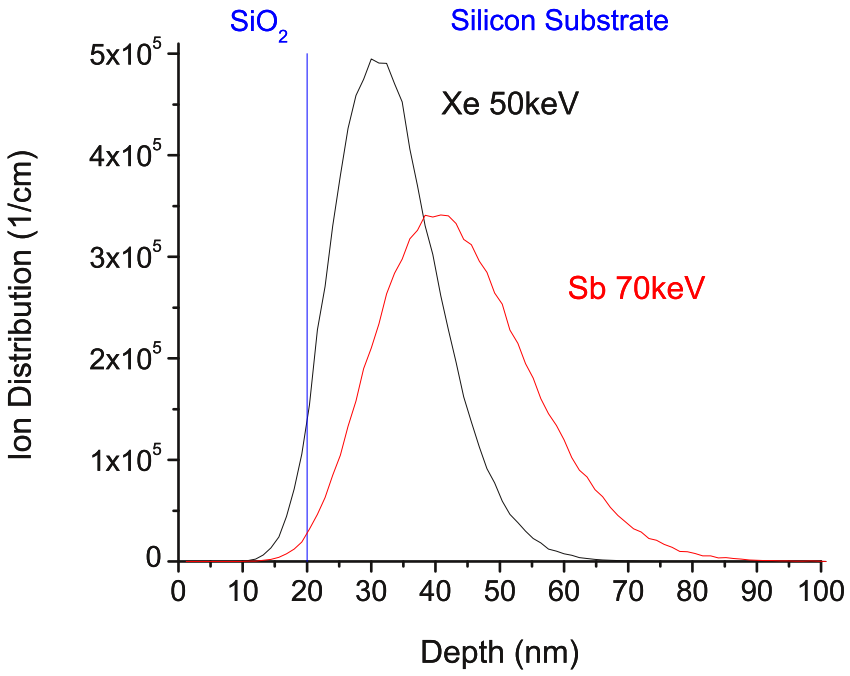


Figure 7.11: Monte Carlo simulations (SRIM code [116]) for antimony and xenon ions into 20 nm of silicon oxide on silicon substrate.

expected implant depth for both ion species can be seen in Fig. 7.11. A full removal of the LTO and gate electrode is assumed during the FIB process of opening up the implant holes. Except a few ions the majority of them reaches the silicon substrate. The devices are biased above threshold ($V_{gate} = 1.1\,V$ , $V_{sd} = 0.1\,V$ with source grounded) at a source/drain current of $\approx 200\,nA$. The device current is amplified with a current amplifier (Stanford Research 570) and the signal then displayed and recorded with a digital oscilloscope. After the ion beam is created and adjusted to a certain beam density ($\approx$ few $pA/mm^2$), the ion beam is operated in pulsed mode. A high voltage signal is applied to a deflector plate again which moves the ion beam on and off the target, which is kept at room-temperature. The pulse sequence is

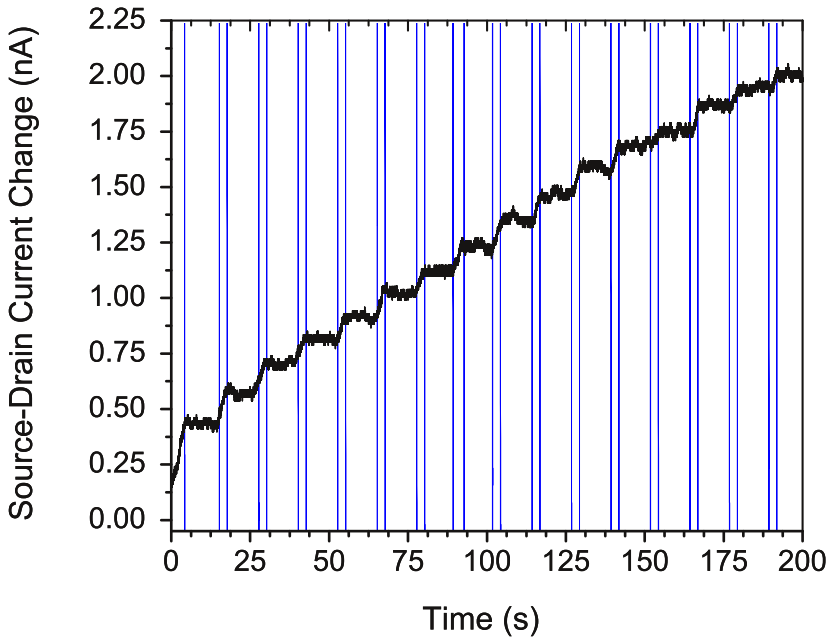


Figure 7.12: Device current (adjusted by offset of $\approx 200\,\mathrm{nA}$) versus time. The a-FET is exposed to the antimony ion beam during the 3 second long intervals [60].

controlled by a self-written LabVIEW program. Fig. 7.12 shows the channel current of an a-FET device during one of the pulse sequences. The sample is exposed to the antimony ions for 3 seconds at a time, indicated by the blue interval lines. The beam density is chosen so that $\approx 3$ ions/interval reach the channel area. An increase of the device current is visible during each of the intervals. This is attributed to the formation of positive charge traps in the oxide layer [194], which reduce the threshold voltage of the device and increases the effectively applied gate voltage.

In order to verify single ion hits, the average number of ions per interval needs to be decreased. The beam current density and interval length is adjusted, so that less than one ion per interval is expected on average. In this case, the average number of xenon ions per interval is reduced to $\approx 0.2$. This means that only during certain intervals one or more ions hit the device channel, whereas a lot of intervals do not feature ion impact events at all. During those intervals the current should remain unchanged. Under these conditions the probability for no event is $\approx 82\,\%$, for one ion hit $\approx 16\,\%$ and for multiple ion hits $\approx 2\,\%$. Fig. 7.13 shows another device current trace versus time with the adjusted beam intensity and pulse length.

During most of the intervals the current stays constant. Only during the highlighted intervals a current change can be observed. The effect on the overall current is $\approx 2 \times 10^{-4}$ in each interval. Based on the expected ion hit probabilities and similar values of the current change for both events, the current changes that we see are most likely caused by single ion impact events.

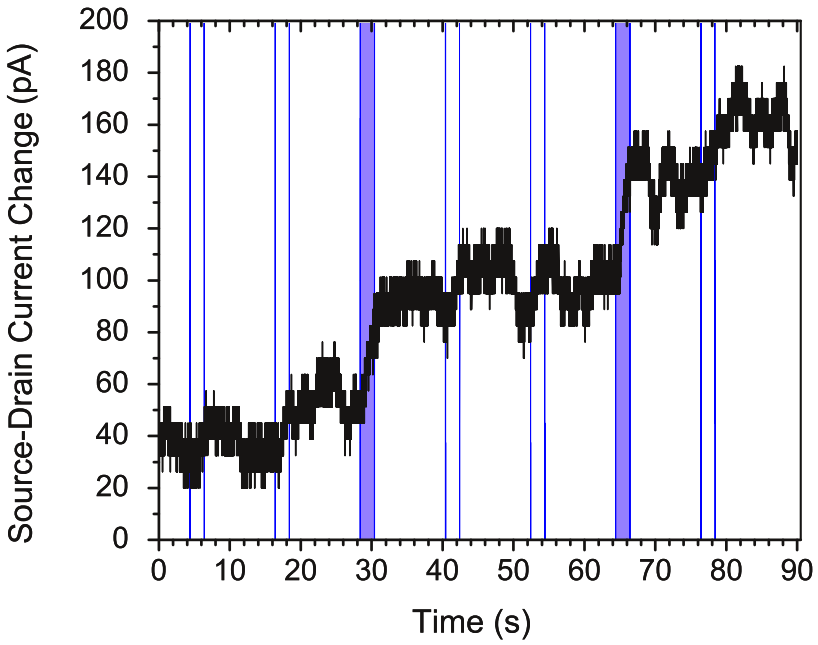


Figure 7.13: Device current (adjusted by offset of $\approx 200\,\text{nA}$) versus time. The $2 \times 2\,\mu\text{m}^2$ sized n-FET is exposed to the 50 keV $Xe^{6+}$ ion beam during 2 second long intervals. Current changes in the order of $10^{-4}$ of the total current can be seen in the highlighted intervals [60].

As can be seen in Fig. 7.12 the device current sensitivity to ion impacts decreases over time. This is also observed for other ion impact energies and charge states. Due to the small current change for these µm-sized devices, a difference of single versus multiple ion hits could not be distinguished from the step heights at the given noise level.
The need for opening up implant holes through the gate electrode holds the risk for device damage. Thus, all devices are annealed for damage repair and dopant activation. This is done with a rapid thermal annealing (RTA) system (AG Associates Heatpulse 210 System). The annealing conditions are 900 °C for 20 s in argon atmosphere, followed by another 30 min $N_2/H_2$-forming gas anneal at 400 °C. A set of IV-curves can be seen in Fig. 7.14. The

leakage current at low gate voltages caused by FIB damage during the hole drilling process is recovered during the annealing step. The reason for the increased channel currents (above threshold) after FIB processing remains speculative.

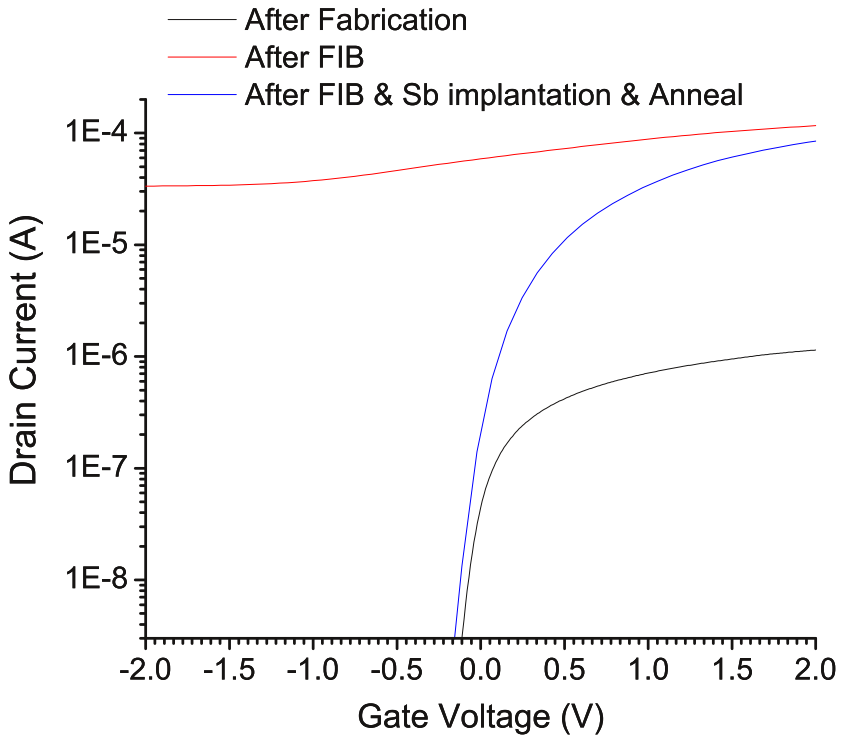


Figure 7.14: IV-curves for an a-FET in pristine condition, after FIB processing and implantation and after device annealing. The source-drain bias is set to 1.0 V [46].

### Sub µm-sized FinResistors

For the sub-µm devices a larger current change upon single ion impacts is expected. The devices are exposed to $Xe^{6+}$ ions at a kinetic energy of 48 keV which are extracted from the ECR1 source. The expected ion depth for these ions and our device geometry is displayed in Fig. 7.15. The devices are connected to a parameter analyzer (Keithley 4200 Semiconductor

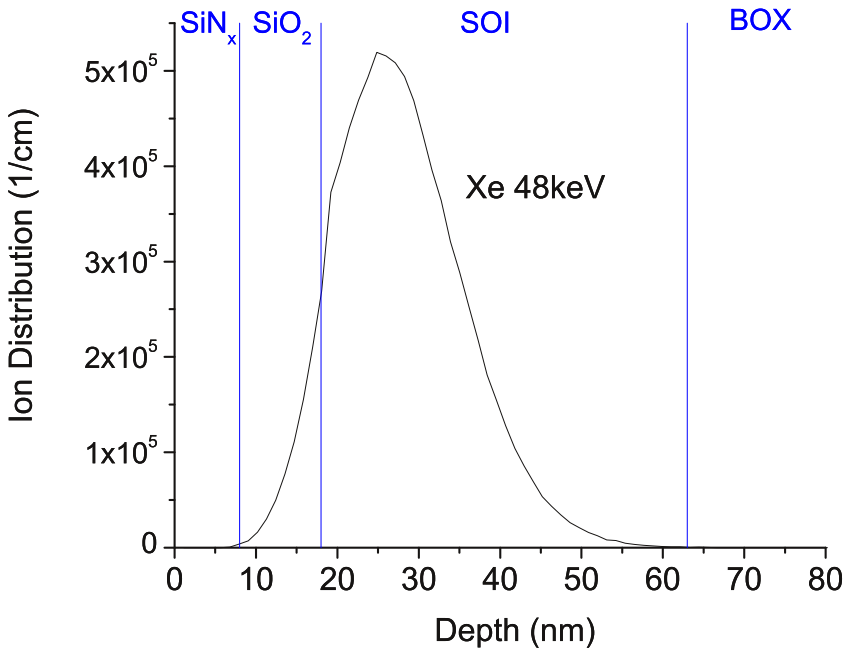


Figure 7.15: Monte Carlo simulations (SRIM code) for 48 keV xenon ions into a layer system of 8 nm silicon nitride on 10 nm silicon dioxide on silicon on insulator.

Characterization System) and source-drain voltages are applied. The source electrode is kept on ground. The sample mount which acts as a back-gate is connected to the beamline frame and thus electrically grounded, too. Due to the way the samples are mounted and the grounded back-gate, the IV-curves do not look symmetric as can be seen in Fig. 7.19. The devices are biased at $V_d = 3.0\,V$ during the detection of ion impacts. A device current trace over time for one of these devices can be seen in Fig. 7.16. The device current fluctuates between two values ($\approx$690 & 725 nA). This is caused by random trapping and releasing of charge carriers by usually a single (or few) defect center. This effect which is called random telegraph noise (RTN) is commonly observed at low temperature but also at room-temperature for deep trap centers [208]. The observed effect is $\approx 5\,\%$ (35 nA over 690 nA) and

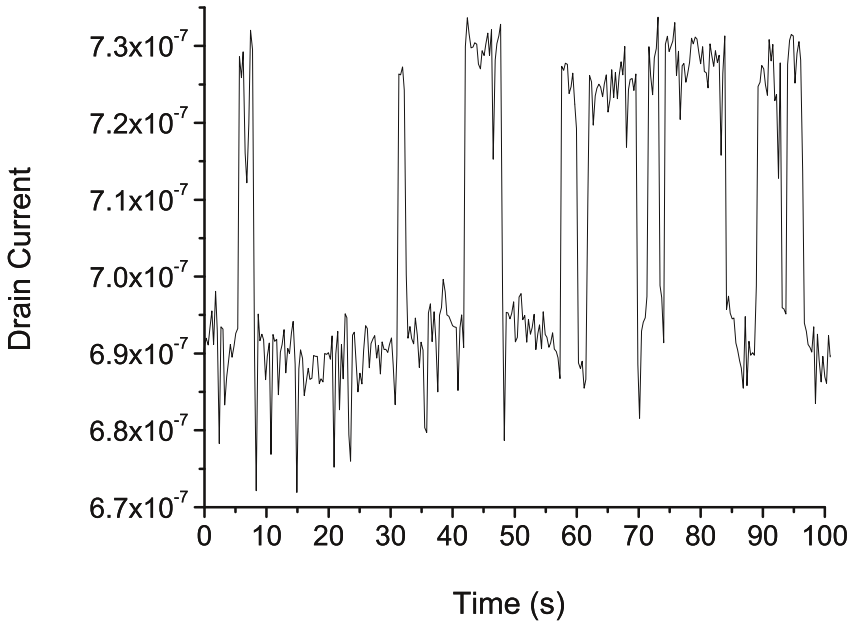


Figure 7.16: Drain current versus time before Xe hits for a 100 nm device. The value for the device current switches between two values, showing RTN behavior with a $\approx 5\,\%$ effect on the device current.

caused by most likely a single defect center at the silicon/silicon-oxide interface (grown oxide or buried oxide).

This indicates that the device currents are very sensitive to changes in their environment and thus single ion hit events. In contrast to the pulsed ion beam used for the planar devices, a constant ion beam of again $\approx$ few pA/mm$^2$ is used. The devices that the data is acquired from have a silicon fin with a width of 90 nm which is surrounded by 10 nm oxide and 8 nm silicon nitride on both sides. For a device geometry of $300 \times 130\,\mathrm{nm}^2$ one expects a single ion to hit the device area every 33 seconds on average. Ions hitting the $n^+$ area should not result in a signal change since the overall resistance of the device is dominated by the $n^+$ free area.

Fig. 7.17 shows three current traces. They were taken in sequence and the ion beam exposes the sample during the second curve only (curve in red, between the 30 and 400 second time stamp). Both other current traces are shown as reference. Big changes in the device current can be observed. In this sequence, the current drops overall initially. After a while, the current steps change direction and an increasing current is observed. The very first ion hits into the device which happened prior to the displayed sequence increased the device

current. Defect centers created in the silicon channel reduce the electron mobility and thus the conductivity and device current. Accumulation of charge in the oxide surrounding the

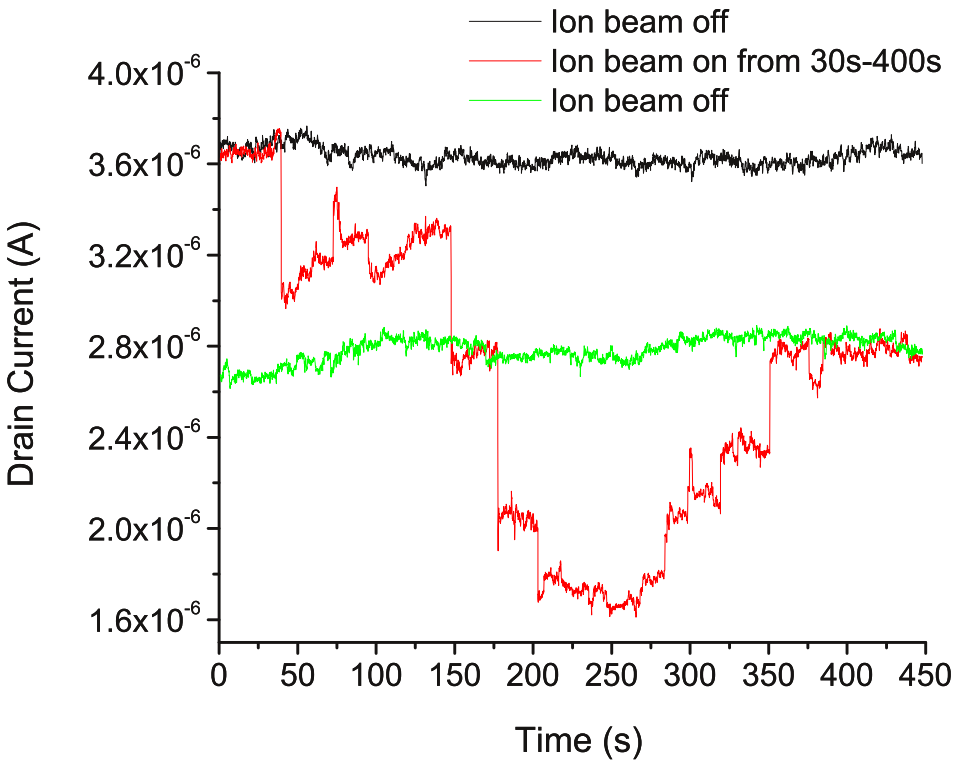


Figure 7.17: Drain current versus time for one of the 100 nm sized devices.

channel can cause a current increase similar to the case of the planar devices inducing a 2DEG. Both effects result in opposite device current changes and are competing with each other. A reduction of the channel mobility by defect creation in the silicon can be offset by the trapped oxide charge accumulation over time and vice versa. No apertures smaller than the silicon fin, were used to map out the response in device currents and thus the ion impact locations are not known here. The knowledge of the exact single ion implant locations should help to interpret the changes in device currents. An ion which hits the device in the center, penetrates the oxide layer and comes to rest in the silicon channel after creating defect centers there would affect the device current differently than an ion that hits the edge of the fin and mostly travels along the vertical oxide film creating positive charges oxide traps there. The use of implant apertures smaller than the device geometry would help in this regards to map out the device response. The main focus of the conducted experiments here with randomly impinging ions is

to demonstrate the sensitivity of these devices to single ion impact events which was achieved as can be seen clearly in Fig. 7.18. Assuming two ion hits can be resolved from each other if they hit with 0.5 seconds separated from each other at the given data acquisition resolution (which is a very modest assumption), one can calculate the probability of two or more ions hitting the sample within a 0.5 second interval. For the calculated beam density of 1 ion per 33 seconds as mentioned earlier, the average number of ions one expects for a 0.5 second time interval is 0.0152. From the Poisson distribution follows that the probability for two or more ions hitting the device area within these 0.5 seconds is $\approx 1 \times 10^{-4}$. That means that every 10,000 intervals or every 5000 seconds, two or more ions would hit the device area within 0.5 seconds and could not be resolved. Going through a similar calculation, one obtains that the chance for having one of those multiple hit intervals in the displayed 370 seconds where the sample is exposed to the beam is $\approx 6.8\,\%$, for two multiple hit intervals $\approx 0.25\,\%$ and for more than two multiple hit intervals $\approx 6 \times 10^{-5}\,\%$. From that, the majority of the current steps are caused by single ion impact events and the differences in the channel current response seen in Fig. 7.18 come from differences in defect creation for individual ions, e.g. variations in impact locations, or partial cancelation of the two competing effects on the channel current, rather than multiple ion hits.

Fig. 7.19 shows IV-curves for the pristine and exposed device. A difference is clearly visible with the device showing an elevated current conditions at same bias conditions. The total number of ion hits expected from the exposure time and beam current density is $\approx$ 21, whereas from the current traces $\approx$ 25 current steps are counted which matches well and lies within all measurement uncertainties and statistical distribution. Recovering the device performance by damage repair upon annealing in e.g. forming gas was not attempted.

## 7.5 Discussion & Outlook

In this chapter, a new single ion impact technique was explored and tested for compatibility with our device layouts and ion implant approach. Device currents are used to monitor impacts of low kinetic energy ions at room-temperature and clear single ion impact events are detected as can be seen in Fig. 7.18. Due to the similar mass of xenon and antimony, similar damage levels and device responses are expected for antimony ion implantation so that the demonstration with the noble gas atoms is legitimate. The work validates the sensitivity of similar sized devices of different device architecture (e.g. quantum dots) and thus their potential for single ion doping. The ion implantation step can be either incorporated in

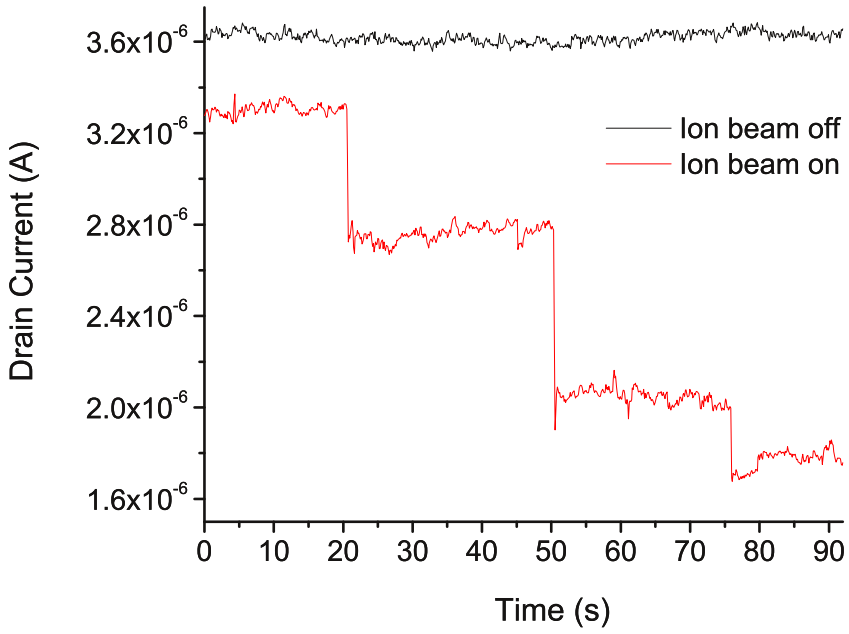


Figure 7.18: Channel current versus time showing ion impact events. The relative current change for the three impact events is ≈18, 26 and 10 %.

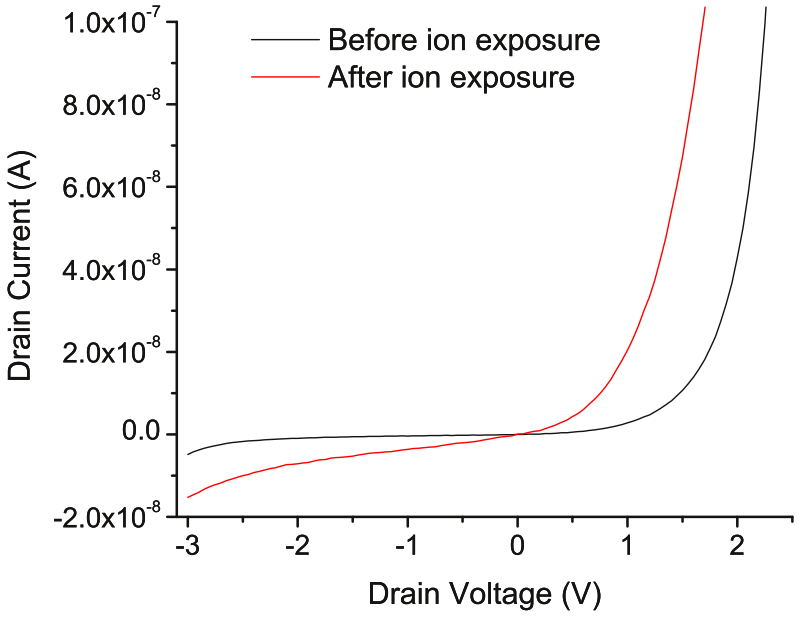


Figure 7.19: IV-curves before and after exposure to xenon ions.

the device fabrication process or conducted on final devices, even if this requires a post processing step to open up implant holes. The single ion impact response of a device will depend on the exact device geometry and implant parameter. The use of smaller implant apertures and the knowledge of the exact impact location will allow a better study of impact responses to the device current. This can be done with scanning probe aligned ion beams where the ion beam is stepped over the device area as shown in chapter 6. The FinResistor devices shown here offer the possibility of nuclear donor spin readout via spin dependent recombination [141, 196–198] or trapping [145, 199] during illumination. Thus besides the proof of single ion impact compatibility, they can be used in electrically detected magnetic resonance experiments to read out spin states of the present antimony-121 ions (background doped during device fabrication) or deliberately implanted other donor species.

## Acknowledgments

The author would like to thank Arunabh Batra with whom the ion implantation work was performed on the planar devices, Cheuk Lo for providing the planar devices for SII testing and his help with the fabrication of the FinResistors, Scott Duhey for the electron beam lithography work and Thomas Schenkel for opening up the implant holes of the planar aFETs via focused ion beams.

# Chapter 8

# Creation of Nitrogen-Vacancy Center Arrays in Diamond

*This chapter addresses the formation of few NV center arrays. Nitrogen ions are implanted through dynamic shadow masks (SPM cantilever) into diamond samples. Upon sample annealing the formed NV center arrays are examined by photoluminescence microscopy. Preliminary results on nitrogen channeling effects during ion implantation and work on an ion detection technique similar to chapter 7 are presented.*

## 8.1 Introduction

As mentioned in chapter 2.6, the NV centers is a promising qubit candidate, mainly due to its long coherence times at room-temperature [165], easy optical readout and the ability to be manipulated on sub-nanosecond time scales [159]. The defect centers have been used to demonstrate simple quantum algorithm operations [88], the formation of quantum registers [162, 209–211] and make appealing building blocks for large array structures using magnetic dipolar coupling as well as for microcavity arrays using optical coupling schemes [212–214]. Initial studies of NV center were all conducted on already present and randomly distributed centers in natural diamond samples. As efforts evolve to implement those different coupling mechanisms to build up large scale quantum computer architectures, the precise and reliable positioning of NV centers next to each other or to device structures becomes more and more important. One option is to introduce vacancy defects into nitrogen rich diamond samples, e.g. 1b-diamond which contains up to 300 ppm of residual and mostly substitutional nitrogen [215]. The creation of vacancy centers can be done by electron irradiation [155, 216] or ion implantation with e.g. helium or gallium [217, 218] which leaves the option of using focused ion beam systems or apertures for the local creation of NV centers. During an annealing step with temperatures above 600 °C the vacancies become mobile [219] and move through the diamond lattice where they can find a nitrogen atom and form the NV center. However, a high background concentration of nitrogen atoms reduces the spin-spin relaxation time [220]. This can be avoided by implanting nitrogen ions into high-purity diamond samples with nitrogen contents of a few ppb or even below. There the main decoherence source is residual $^{13}C$ in the diamond lattice, which can be further eliminated by isotopically enriched diamond with nuclear spin free $^{12}C$ [165]. During the nitrogen implantation process, nitrogen atoms and the vacancies are induced at the same time. The use of high energetic nitrogen ions [54, 68] increases the formation efficiency of NV centers due to the increased creation of vacancy defects [71, 72], but also decreases the placement precision due to increased range straggling. The implantation of nitrogen atoms or molecules low in kinetic energy [69–76] reduce the range straggling and can be used for high precision placement of NV centers.

A different approach is to use NV center containing nanodiamonds [33, 35, 221, 222]. The particles which contain a distribution of NV centers can be optically preselected and suitable candidates can be placed on sample surfaces at desired NV center locations [223, 224].

Here, the placement process of low kinetic energy nitrogen ions and NV pattern formation with our scanning probe system is explored and demonstrated as first reported with µm-sized

implant spots by our group [46], which was followed up recently by [78].

## 8.2 Experimental

The samples used here are mostly high-quality chemical vapor deposition (CVD) diamond samples obtained from Element Six [225]. Those single crystal (100) samples contain less than 5 ppb residual nitrogen concentration. The only exception is for an initial test implant for which diamond on silicon samples (DOS) from SP3 [226] are used, which can bee seen in Fig. 8.2a. The DOS sample consists of a $\approx 1\,\mu m$ thick diamond film (grain size $\approx 100\,nm$) on regular single crystal silicon substrate with unknown nitrogen background concentration. Prior to the implantation, all samples are cleaned in acetone and isopropanol. A cleaning step in piranha solution for 10 min at 120 °C & DI water rinse followed for the CVD samples. The samples are implanted with nitrogen-15 ions with 7 & 8 keV kinetic energy with mean projected ranges of 10.7 & 12.0 nm respectively (SRIM simulations [116]). Nitrogen-15 is chosen for easier differentiation from residual nitrogen in other experiments and a magnet scan can bee seen in Fig. 8.1. By doing so the chance to study a NV center formed by one of the residual nitrogen atoms present in the diamond sample with a created vacancy defect is limited. The natural abundance ratio of both nitrogen isotopes is 272, dominated by nitrogen-14. Multiple holes are drilled into SPM cantilevers to act as implant apertures. Having differently sized apertures in the same cantilever enables to form multiple implant arrays at the same time. Due to the timed implant the fluence for each implant spot stays the same but the overall number of implanted nitrogen atoms and thus active NV centers per spot will vary. In order to find the implant patterns, alignment marks, e.g. deposited structures that can be found via SPM scans are of great convenience. For these implants no alignment are used and the overspilling mm-sized implant spot surrounding the area blocked by the cantilever is used to find the implant area (see Fig. 8.2a). Rapid thermal annealer (AG Associates - Heatpulse 210) are used for the post implantation annealing step. The photo-luminescence (PL) images are taken with three different optical microscope setups:

#### PL Setup 1

The first setup is a wide-field total internal reflection (TIRF) microscopy system with Olympus IX-81/Andor EMCCD camera at the Molecular Foundry at LBNL (Biological Nanostructures Facility). It features lasers of different wavelengths, a halogen lamp and filter settings for the

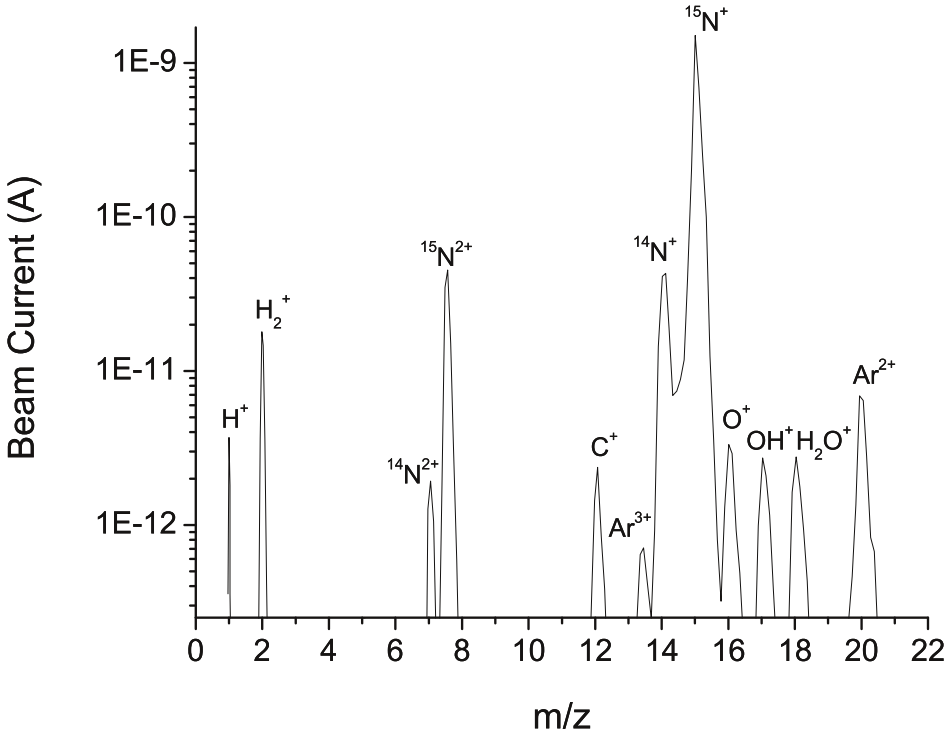


Figure 8.1: Magnet scan from ECR1 with nitrogen-15 gas as source supply. The beam is extracted at 7 kV.

selection of excitation and collection wavelength regions. In this case a 488 nm laser and a 573 - 613 nm collection filter is used.

**PL Setup 2**

The second setup is a confocal Raman microscope system from Witek in the Imaging and Manipulation of Nanostructures Facility at the Molecular Foundry at LBNL. A 532 nm, 100 mW laser is used as an excitation source. The objective is a Nikon LU Plan Apo 100x (NA = 0.95, WD = 0.40) for use in air. The maximum scan range is $100 \times 100\,\mu m^2$. In contrast to the other two setups this one features a spectrometer and no hardware filters between the sample and photo detector. During a scan a PL spectrum is acquired at each point of the scan area. The application of software filters lets one view the scan area within desired wavelength ranges in real time or post data acquisition.

### PL Setup 3

The last setup is a confocal system home build by Alex Hegyi in Prof. Yablonovitch group at UC Berkeley. It consists of a 1 mW, 532 nm laser and an IDQuantique photodetectors (id100-50-ULN) behind a 532 nm longpass filter cutting off right behind the laser line. A 100x lens (NA=1.4, Nikon CFI Plan Apochromat NCG) with Nikon immersion oil type NF is used. The maximum scan range is $20 \times 20\,\mu m^2$.

## 8.3 Results

Fig. 8.2a shows a PL image of an implant into a DOS sample acquired with PL Setup 1. The implant species is $^{15}N^+$ at an implant energy of 8 keV and a total fluence of $5.5 \times 10^{12}$ ions/cm$^2$. The sample is annealed in argon atmosphere at 800 °C and 850 °C for 5 min each before the image is taken. During the implantation the tip is not moved and the edge of the mm-sized ion beam can be seen. The blocked area of the cantilever that is moved into the ion beam is clearly visible. Two implant spots $\approx 20\,\mu m$ below the center of the image center and within the cantilever can be found.

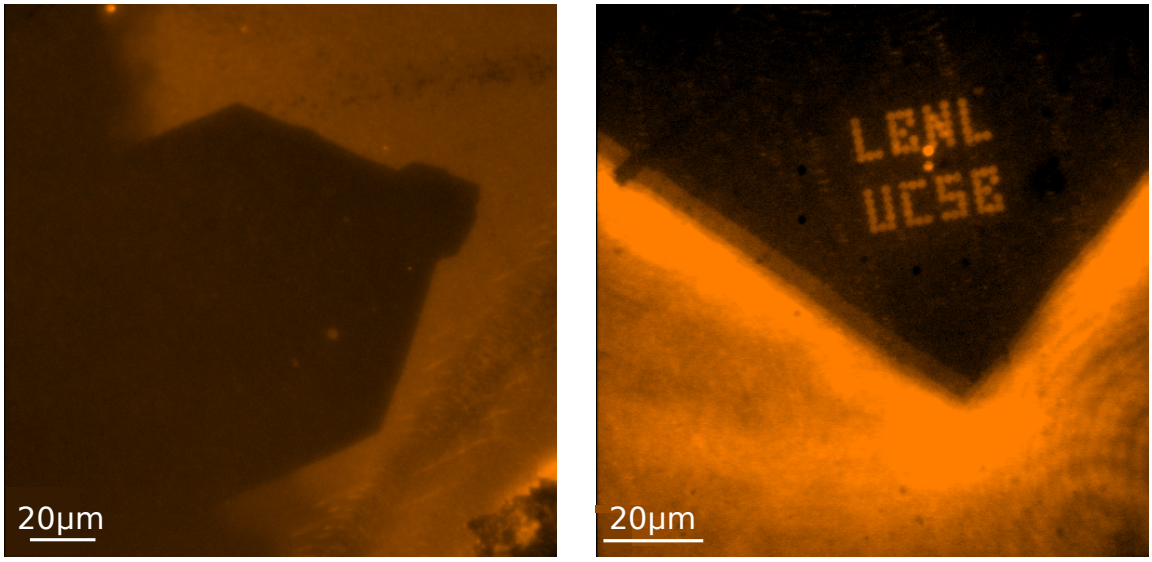


(a) Blocked cantilever area at the edge of the mm-sized ion beam implant spot on a DOS sample.

(b) Blocked cantilever area with NV center array.

Figure 8.2: PL images of nitrogen implanted diamond areas.

For the implant that can be seen in Fig. 8.2b a different tip is used, which has apertures of $\approx 1.5\,\mu m$ and $\approx 80\,nm$ in diameter drilled into it. After the SPM cantilever is broad into contact with the diamond surface (high-purity CVD type), the ion beam is tuned and the cantilever moved around following a point list with dwell times of 60 sec per spot. This results in a fluence of $5.9 \times 10^3$ ions/$\mu m^2$ ($^{15}N^+$ at 7 keV) per implant spot. The array consists of a "LBNL" and "UCSB" writing and two additional brighter implant spots in between which are formed during the initial ion beam tuning. Due to an adjustment of the cantilever position during the tuning procedure, two tuning spots are formed. After ion implantation the sample is annealed in argon atmosphere at 850 °C for 10 min. The end of the cantilever with the NV center array of the micron-sized implant spots can be seen clearly in the PL image (PL Setup 1). The second and smaller aperture is located closer to the cantilever tip than the micron-sized one. That pattern could not be found and resolved with this microscope setup. The expected number of nitrogen-15 atoms for the smaller implant spots is $\approx$ 30. For a 7 keV nitrogen implant a NV center conversion efficiency of $\approx 2\,\%$ is expected [71]. Thus on average less than one NV center is expected per spot, which means that more than 50 % of the implant spots will not show up (see Fig. 2.6 for $\lambda = 0.6$). Due to the overall large amount of implant spots the pattern should be still resolvable, but for the following reason this was not achieved. First off, the purity of the argon atmosphere during the anneal in the RTA systems was not good enough, so that residual oxygen graphitized parts of the sample surface most likely. This removed parts of the implanted nitrogen as well and lowered the number of remaining nitrogen and NV centers per spot. This can be avoided by annealing the diamond in a reducing atmosphere containing hydrogen as e.g. forming gas [227]. Another reason is that the location of the smaller hole was too close to the edge of the cantilever. During the generation of the array and the movement of the tip, at least parts of the array (edges) were not blocked by the cantilever body anymore and exposed to the outside of the ion beam. Another reason is that despite the low residual nitrogen background of those high-purity CVD samples, the background is not uniformly low enough across the sample to resolve single NV centers. For other implants (not part of this work) this was circumvented by the use of alignment marks and prescreening of the sample for promising implant locations.

To prevent the loss of the implant array, a different cantilever and aperture locations are used to form another NV center array in a different high-purity CVD diamond sample. Two overlaid SEM image of the cantilever can be seen in Fig. 8.3 showing the overall cantilever shape and three holes with diameters of $\approx 1.6\,\mu m$ and $\approx 100\,nm$. The point list for the array

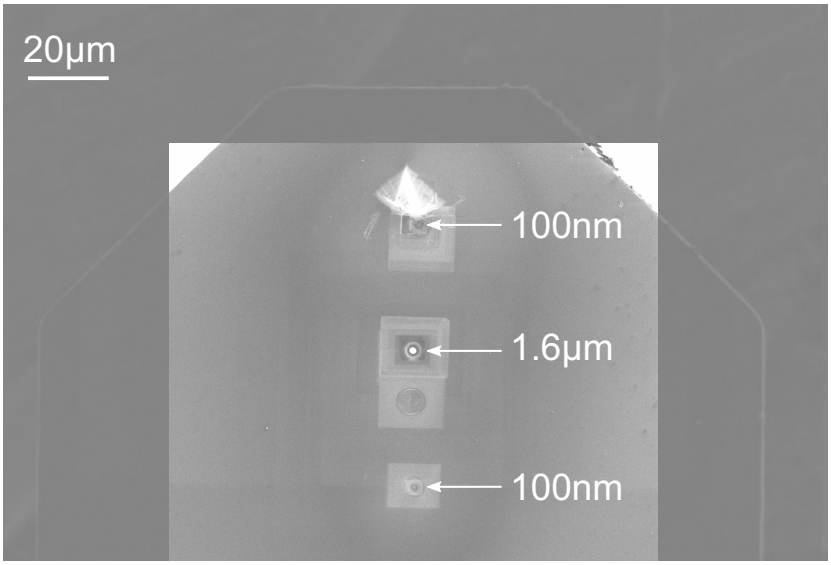


Figure 8.3: Two overlaid SEM images of the AFM cantilever used for the nitrogen array implants shown in Fig. 8.5 & 8.6.

consist again of the "LBNL" writing and a line of dots varying in fluence with equidistant dot spacing. For the lettering a fluence of $3.5 \times 10^4$ ions/µm$^2$ is used; for the line of dots $1.5 \times 10^5$, $1.0 \times 10^2$, $1.0 \times 10^3$, $2.0 \times 10^4$ and $1.5 \times 10^5$ ions/µm$^2$. The two spots with the highest fluence terminate the line with equally spaced dots to make the location of their positions easier. The implant species is again $^{15}N^+$ at 7 keV kinetic energy. After implantation the sample is annealed in argon atmosphere at 850 °C for 17 min. A photoluminescence spectrum taken with PL Setup 2 at the position of one of the µm-sized implant spots of the "LBNL" writing can be seen in Fig. 8.4. It shows the zero-phonon line of the NV centers ($\lambda = 637$ nm) and its phonon broadened contributions at higher wavelengths. A PL image in the wavelength range from 634.2 to 640.9 nm, which is highlighted in the PL spectrum is displayed in Fig. 8.5.

The "LBNL" writing created with the 1.6 µm aperture can be clearly seen. The tuning spot is located below that and further down, parts of the linear dot array with varying fluences is visible as well. More interesting than the µm-sized implant spots are the ones created with the 100 nm aperture. Due to the diffraction limit of the optical microscopes used, the PL spot sizes are larger than the implanted area containing the NV centers. In Fig. 8.6 a PL image (taken with PL Setup 3) shows the second pattern formed with the aperture closest to the cantilever end. The last three letters of the "LBNL" writing and the tuning spot are visible. The varying background PL intensity can be observed as well. The two brighter spots in the diagonal line of the letter "N" are caused by a software glitch during the implantation process.

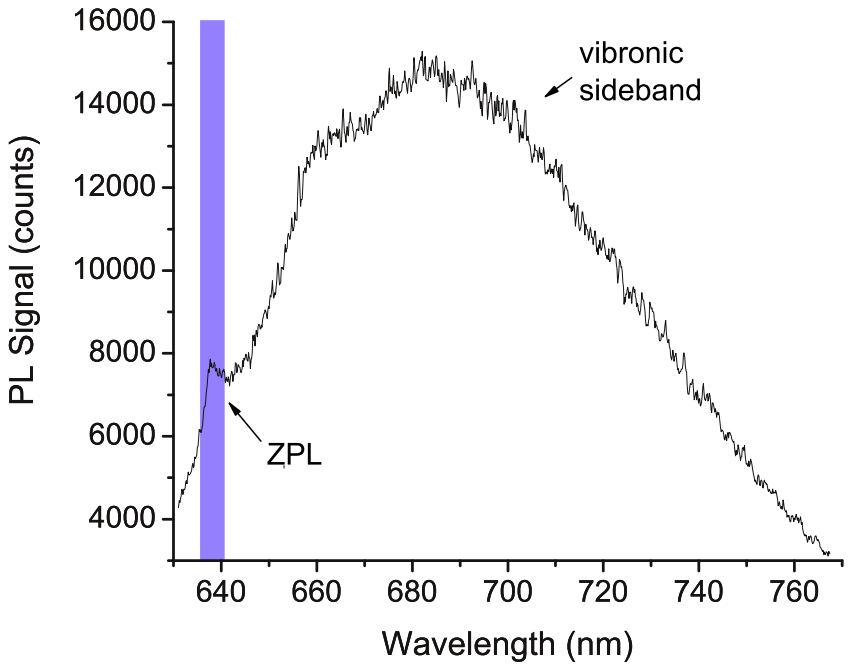


Figure 8.4: Collected PL spectrum at the position of one of the µm-sized NV center spots of Fig. 8.5 showing the zero-phonon line peak of the NV center at 637 nm and the phonon broadened emission peak at higher wavelengths. The highlighted area is the displayed data range in Fig. 8.5.


Figure 8.5: PL image of a µm-sized NV center array obtained with PL Setup 2. The displayed wavelength range is the highlighted range around the ZPL of the NV center (see Fig. 8.4: 634.2 to 640.9 nm).

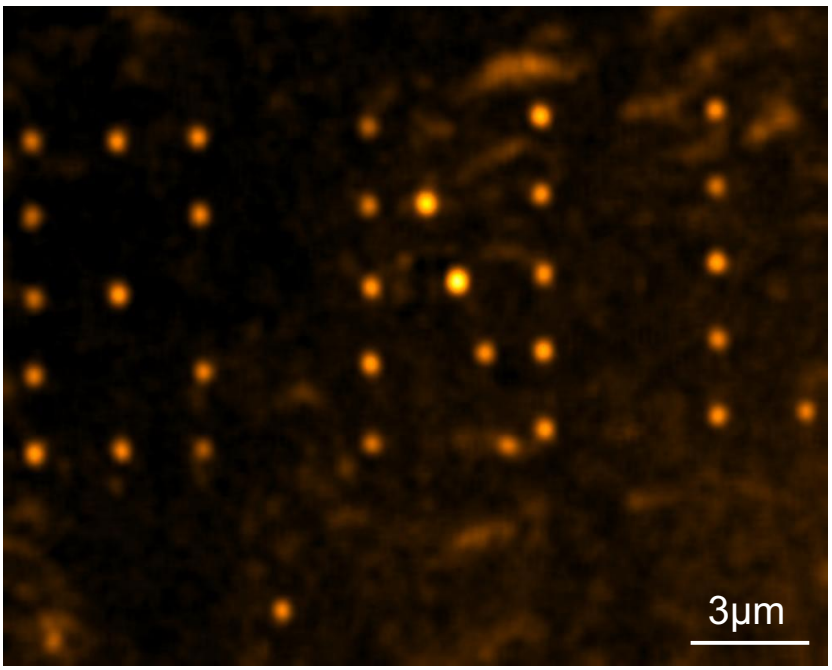


Figure 8.6: PL image of ≈ 100 nm sized NV center implant spots taken with PL Setup 3.

The scanning routine got stuck at those two points for a longer period of time than aimed for (again 60 s per spot). At the lower right corner of the same letter two spots can be seen, with the right one being part of the implanted array. The left one is either part of the PL background or a residual NV center. The expected number of implanted nitrogen ions per spot is 275. Assuming a 2 % conversion efficiency [71] this yields an average number of 5.5 NV centers per spot. Extrapolating from a similar implant pattern and taking into account the difference in fluence and aperture size, we expect $\approx$ 7 - 11 NV centers per spot.

## 8.4 Discussion & Outlook

As with donor based approaches in silicon, the precise positioning capability of these color centers next to each other or to device structures is of great importance. Here, the versatility of ion beam aligned implantation via scanning probe microscopes is shown. Initially, the technique was developed to place donor atoms in silicon but can be easily applied to the formation of NV centers in diamond. The same implant strategy of non-invasive SPM imaging and finding the area of interest followed by the ion implantation can be utilized.

However, the conversion efficiency from implanted nitrogen atoms to desired negatively charged NV centers is small [46, 70, 77], whereas an electrical activation of donors close to 100 % can be achieved [134]. For low kinetic energy ions which are favored for their small range straggle during the implantation process, the conversion efficiency is only a few percent [71, 72]. Nevertheless, by adjusting the implant dose and aperture size, arrays with on average $\approx$ 1 NV center per spot can be achieved as it was demonstrated with on chip e-beam apertures and spin qualities studied [70]. The same approach works when using apertures in SPM cantilevers. The possible reduction of the implant apertures in the cantilever body down to a few nanometer [53], make the discussed approach very attractive for placing NV centers into diamond devices. Further, the same placement approach can be used for creating other color centers than the NV center by simply changing the implant species to e.g. nickel or silicon.

In order to place single NV centers, all described mechanisms for SII detection (see chapter 7.2) are valid candidates and a similar dopant impact detection mechanism as demonstrated in this work (see chapter 7) could be implemented for the color center in diamond materials system. Combining the implant process with single ion detection schemes makes little sense at the moment because the Poissonian NV center formation will negate the accu-

rately known number of implanted ions. However, once the knowledge about the NV center formation efficiency has grown and an increase achieved, the detection of single nitrogen atoms will be valuable for the placement of single NV centers. Hydrogen terminated diamonds show surface currents which could be used similarly to the device currents shown in this work to detect impact events. Alternatively, thin conductive layers as e.g. graphene could be placed on the surface to pass electrical currents which could be interrupted by impinging ion impacts. Sheet resistance and hall mobility changes of graphene on $SiO_2$ caused by ion irradiation have been demonstrated by others [228]. First progress for a similar study with graphene on diamond was made and the preliminary results shown in the following.

A $4 \times 4\,\mathrm{mm}^2$ sized diamond (Element-6 [225], (100) orientation) with a residual nitrogen level of less than 1 ppm is cleaned in acetone, isopropanol and piranha solution. Few µm-sized graphene patches are deposited on the diamond similar to the technique described in [229]. A highly ordered pyrolytic graphite (HOPG) sample is pre-patterned via an optical lithography and reactive ion etch step. The HOPG sample is mounted in a hydraulic press apparatus and brought into contact with the diamond and released afterwards. Metal electrodes (5 nm Cr / 45 nm Au) are deposited via a lift-off step. Optical microscope images during the device fabrication can bee seen in Fig. 8.7. Raman microscopy measurements indicated few-layer graphene spots but the exact number of layers could not be obtained. The successful electrical contacting to one of the few-layer patches is shown in Fig. 8.8.

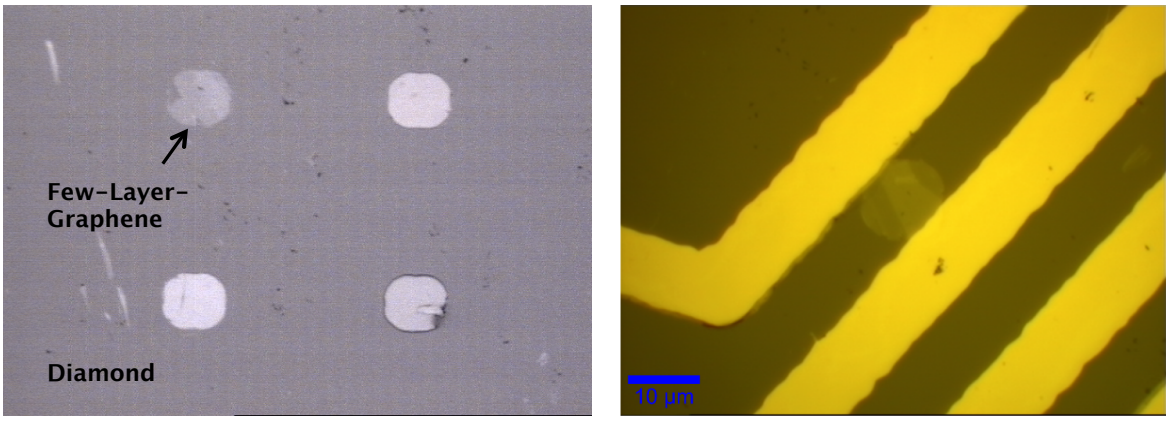


(a) Few-layer on graphene after deposition.

(b) Electrically contacted few-layer graphene patch (in center).

Figure 8.7: Optical microscope images during device fabrication.

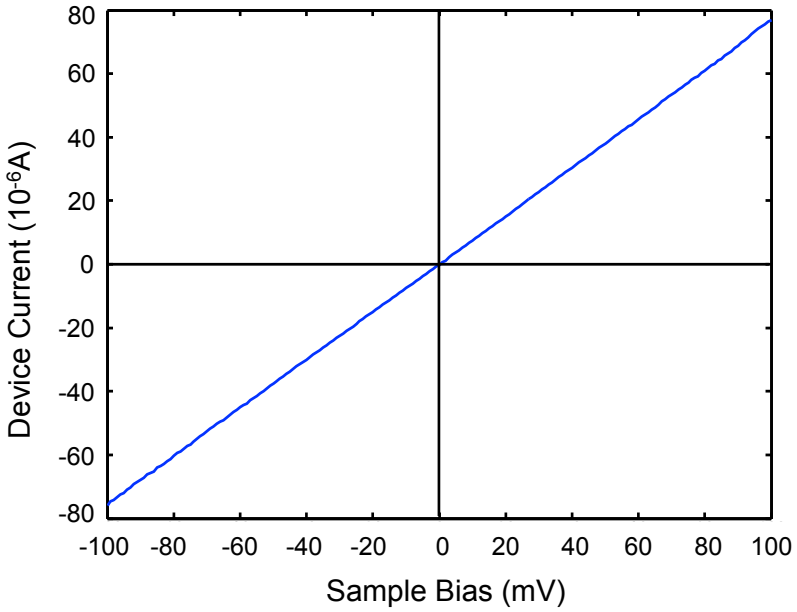


Figure 8.8: IV curve of the electrically contacted few-layer graphene patch seen in Fig. 8.7b.

Due to the high electric constant of diamond and sample thickness, we could not make use of the electrostatic forces between the HOPG piece and sample substrate which can result in single layer graphene on silicon [229]. As a next step, a graphene transfer similar to [230] will be utilized to coat the diamond sample with a single graphene layer. Then the graphene mobility can be recorded versus nitrogen ion dose and the maximum graphene spot size for potential SII detection extracted.

Another aspect that needs to be considered for reliable NV center placement is the implantation accuracy. NV centers make appealing building blocks for large array structures using magnetic dipolar coupling as well as for microcavity arrays using optical coupling schemes [212–214]. As efforts evolve to implement those different coupling mechanisms to build up large scale quantum computer architectures, the question arises of how reliably NV centers can be positioned next to each other or to device structures. One important aspect here is that different coupling schemes have different tolerances for the placement and placement error of NV centers. E.g. a spacing of up to about 100 nm might be possible for nearest neighbor coupling of NV centers via magnetic dipolar coupling in ultrapure diamond [165] and the NV placement accuracy in an array or pattern should ideally be much smaller than the NV spacing. As mentioned before, a common technique for formation and placement of NV centers in diamond is via implantation of nitrogen ions [54, 68–77], followed by annealing

to temperatures above 600 °C. The spatial placement uncertainty is then given by the ion beam spot size on the sample, ion range straggling and diffusion of the nitrogen atoms during annealing. The ion beam spot size can potentially be around a few nanometer, either with the use of focused ion beam tools or implant apertures [53, 66, 78]. Intuitively, the higher the kinetic ion energy the higher the range straggling which makes ions low in kinetic energy the choice for precision ion implantation. In order to quantify the ion range straggling, secondary ion mass spectroscopy (SIMS) measurements are performed on low kinetic energy implants. Previously, SIMS measurements have only been reported for nitrogen-14 implants at high kinetic ion energy (300 keV) [231]. For this, we use Element-6 [225] diamonds with (100)

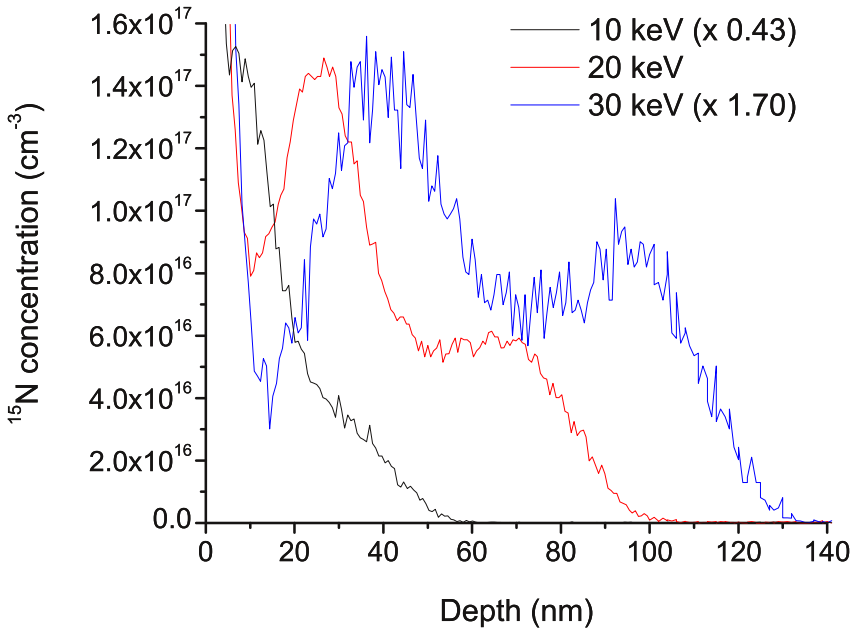


Figure 8.9: Nitrogen depth profiles for different nitrogen implant energies [70].

surfaces and different nitrogen purities (<5 ppb and <1 ppm grade). Sample cleaning involves ultrasound bath steps with acetone, isopropanol and DI water and a boiling acid step in a nitric and sulfuric acid mix. For the depth distribution study, nitrogen-15 ions of different charge states (1+ to 3+) are extracted at kinetic energies of 10, 20 and 30 keV with the ECR1 source. The samples are exposed to millimeter sized ion beams, so that enough material gets exposed for convenient depth profiling of doses ranging from $0.5 - 1.0 \times 10^{12}\,\mathrm{cm}^{-2}$. SIMS measurements are performed by Evans Analytical Group LLC [123].

The individual SIMS profiles for each implant condition on the same 5 ppb grade sample

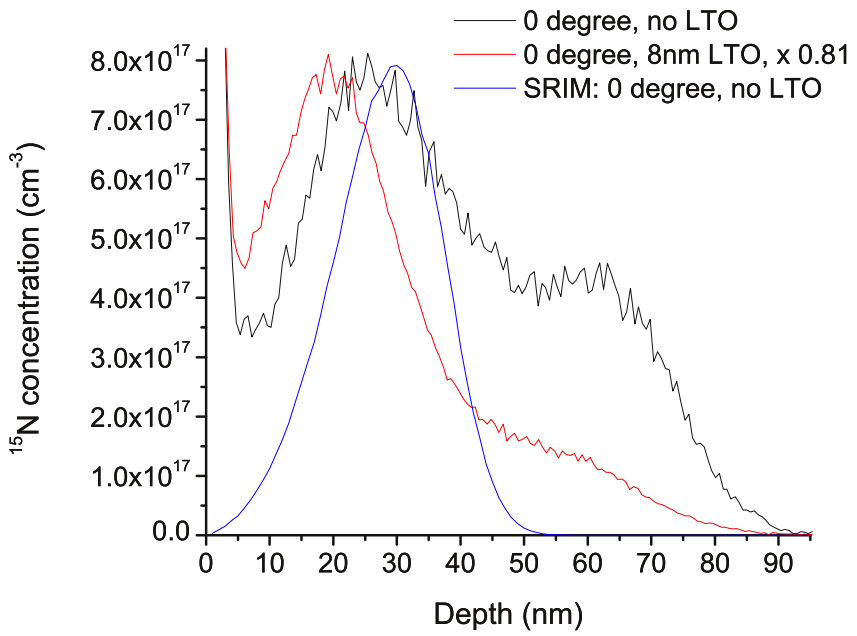


Figure 8.10: Depth profiles for a 20 keV nitrogen implant with and without LTO screening layer and SRIM simulations [70].

are shown in Fig. 8.9. Each profile consists of two peaks. The position of the shallower peak (random implantation peak) in each profile is close to the predictions of Monte-Carlo simulations of ion trajectories using the Stopping and Range of Ions in Matter (SRIM) code (see Fig. 8.10) [116]. For better comparison all profiles are scaled so that the peak heights of the random peaks line up. The deeper second peak is due to ion channeling of the nitrogen ions in the crystalline diamond matrix. The effect of ion channeling (minimum yields and critical angles) in diamond has been studied by backscattering experiments with high energetic (MeV) protons only [232–234]. Our SIMS data shows that the FWHM of the random peak is comparable with the implantation depth itself. In this low kinetic ion energy range, the channeled peak is located a little more than twice as deep as the random peak. Further, an increase of the channeling effect with ion energy is visible similar to the case of boron implants in silicon at comparable ion energies [235]. Common techniques for reduction of ion channeling effects are the implantation through an amorphous screening layer or implantation under an angle off normal to the sample surface. Here, an 8 nm thick low temperature oxide (LTO) layer is used. The influence on the channeling effect, which got reduced, can be seen in Fig. 8.10. The ion energy for all implants and simulations is 20 keV and the ion fluence is

$5 \times 10^{12}\,\mathrm{cm}^{-2}$. The profiles with and without LTO layer are taken on the same <1 ppm grade sample. For the SRIM simulation the following parameters are used: density of 3.52 g/cm3, displacement energy of 37.5 eV. The simulation predicts the random peak at roughly the same depth. The SRIM peak is narrower than the random peak from the experimental data though and misses the channeled peak completely. For the profile of the implant through the LTO layer $x = 0$ equals the surface of the screening layer, not the diamond LTO interface. The shift of the peak towards lower depths could be due to a measurement error caused by inhomogeneous sputtering of the LTO and diamond layers during the SIMS measurement. There the same sputter rate is assumed for LTO and diamond for the depth calibration.

The experimental data shows ion channeling with varying contributions to the nitrogen range distribution depending on the kinetic ion implant energy. This physical phenomenon is not taken into account by the widely used SRIM code. In order to predict and describe nitrogen ion range straggling effects better, further depth profiles of ion implants and simulations to track the channeling effect are in progress. Further, the SIMS measurements can also be used to measure nitrogen diffusion during annealing steps which is cause for the third contribution to the overall placement uncertainty.

## Acknowledgments

The author thanks Alex Hegyi (UC Berkeley) for taking the PL image shown in Fig. 8.6 where the sample was used as a control sample for the verification of the setup's scanning functionality. Further thanks are to Caroline Ajo-Franklin, Jim Schuck and Adam Schwartzberg at the Molecular Foundry at LBNL for their help with the respective optical microscopes, Thomas Schenkel for opening up the collimation apertures in the cantilevers and to David Toyli, Greg Fuchs and David Awschalom (UC Santa Barbara) for helpful discussions and collaboration on the ion range straggling of nitrogen in diamond and related implant work. Last but not least, thanks go to Xiaogan Liang and Stefano Cabrini for helpful discussions, the fabrication of the first multilayer graphene test device (incl. data shown in Figs. 8.7 & 8.8) and training on the device fabrication.

# Chapter 9

# Summary & Outlook

In this work, the previously existing SPM was upgraded for reduced tip wear and increased imaging resolution. Further, improvement opportunities were identified for implementation in a non-contact SPM currently under construction. A new ion source setup for more convenient metal ion beam creation was build and tested for the new non-contact SPM beamline. Device imaging combined with controlled ion implantation into electrical device structures was demonstrated for the first time, showing the precision implantation capabilities of the scanning probe aligned ion beam technique. Additionally, the detection of single impact events of ions low in kinetic energy via changes in device currents was achieved in the same transistors that are also used in spin transport experiments [81, 82]. The versatility of the SPM as an implant tool was shown by the formation of NV center arrays in diamond for optical studies.

With the new non-contact SPM system and reduced tip wear for better lateral resolution, a preciser ion placement will be achieved. This, in combination with smaller implant apertures will allow further studies and mapping of single ion impact responses of sub 100 nm device areas. The implantation of single donor atoms instead of noble gas ions will allow the study of single dopant effects in device characteristics. The FinResistor devices are candidates for single nuclear spin readout measurements. In the limit, these devices which are sensitive to ion impact events can be then implanted with a single dopant atom. The implementation of a SII detection technique for nitrogen atoms in diamond similar to the work presented in chapter 7 is outlined in chapter 8.4. In order to quantify the range straggle and channeling behavior of nitrogen ions in single crystalline diamond during the implant process, follow-up experiments on the results shown in chapter 8.4 including improved simulations that take crystal orientations and thus the channeling effect into account are in progress.

# Bibliography


[1] E. A. Weiss. Information sought on "only a few computers are needed" statement. *Communications of the ACM*, 28:1, 1985.

[2] `http://www.snopes.com/quotes/kenolsen.asp`, accessed December 2010.

[3] `http://nobelprize.org/nobel_prizes/physics/laureates/1956/`, accessed December 2010.

[4] J. Chelikowsky. Silicon in all its forms. *MRS Bulletin*, 27(12):951, 2002.

[5] `http://www.pbs.org/transistor/science/events/silicont1.html`, accessed December 2010.

[6] `http://www.ti.com/corp/docs/company/history/timeline/semicon/1950/docs/54commercial.htm`, accessed December 2010.

[7] `http://www.worldometers.info/computers/`, accessed December 2010.

[8] `http://www.gartner.com/it/products/research/dataquest_qstats.jsp`.

[9] G. E. Moore. Cramming more components onto integrated circuits. *Electronics*, 38(8):114, 1965.

[10] G. E. Moore. Cramming more components onto integrated circuits. *Solid-State Circuits Newsletter IEEE*, 20(3):33, 2006.

[11] `http://www.intel.com/pressroom/archive/releases/2009/20090526comp.htm?wapkw=(Nehalem-EX'+Processor)`, accessed December 2010.

[12] ITRS report. Emerging research devices, 2009.

[13] J. Hutchby. Emerging research devices. In *ITRS Public Conferences*, San Francisco, July 2008.

[14] D. Deutsch and R. Jozsa. Rapid solution of problems by quantum computation. *P Roy Soc Lond A Mat*, 439(1907):553, 1992.

[15] D. R. Simon. On the power of quantum computation. *Proceedings of the 35th Annual Symposium on Foundations of Computer Science*, page 116, 1994.

[16] P. W. Shor. Algorithms for quantum computation - Discrete logarithms and factoring. *Proceedings of the 35th Annual Symposium on Foundations of Computer Science*, page 124, 1994.

[17] P. W. Shor. Polynomial-time algorithms for prime factorization and discrete logarithms on a quantum computer. *arXiv*, 9508027v2, 1995.

[18] L. K. Grover. A fast quantum mechanical algorithm for database search. *Proceedings of the twenty-eighth annual ACM symposium on Theory of computing (STOC)*, page 212, 1996.

[19] L. K. Grover. Quantum mechanics helps in searching for a needle in a haystack. *Phys. Rev. Lett.*, 79(2):325, 1997.

[20] R. van Meter, K. M. Itoh, and T. D. Ladd. Architecture-dependent execution time of Shor's algorithm. *arXiv*, quant-ph/0507023v2, 2005.

[21] T. D. Ladd, F. Jelezko, R. Laflamme, Y. Nakamura, C. Monroe, and J. L. O'Brien. Quantum computers. *Nature*, 464(7285):45, 2010.

[22] B. E. Kane. A silicon-based nuclear spin quantum computer. *Nature*, 393(6681):133, 1998.

[23] B. E. Kane. Silicon-based quantum computation. *Fortschr Phys*, 48(9-11):1023, 2000.

[24] F. Jelezko and J. Wrachtrup. Single defect centres in diamond: A review. *Phys Status Solidi A*, 203(13):3207, 2006.

[25] D. D. Awschalom, R. Epstein, and R. Hanson. The diamond age of spintronics. *Sci Am*, 297(4):84, 2007.

[26] F. Jelezko and J. Wrachtrup. Read-out of single spins by optical spectroscopy. *J Phys-Condens Mat*, 16(30):R1089, 2004.

[27] F. Jelezko, T. Gaebel, I. Popa, A. Gruber, and J. Wrachtrup. Observation of coherent oscillations in a single electron spin. *Phys. Rev. Lett.*, 92(7):076401, 2004.

[28] F. Jelezko, T. Gaebel, I. Popa, M. Domhan, A. Gruber, and J. Wrachtrup. Observation of coherent oscillation of a single nuclear spin and realization of a two-qubit conditional quantum gate. *Phys. Rev. Lett.*, 93(13):130501, 2004.

[29] J. R. Maze, P. L. Stanwix, J. S. Hodges, S. Hong, J. M. Taylor, P. Cappellaro, L. Jiang, M. V. Gurudev Dutt, E. Togan, A. S. Zibrov, A. Yacoby, R. L. Walsworth, and M. D. Lukin. Nanoscale magnetic sensing with an individual electronic spin in diamond. *Nature*, 455(7213):644, 2008.

[30] J. M. Taylor, P. Cappellaro, L. Childress, L. Jiang, D. Budker, P. R. Hemmer, A. Yacoby, R. Walsworth, and M. D. Lukin. High-sensitivity diamond magnetometer with nanoscale resolution. *Nature Physics*, 4(10):810, 2008.

[31] L. Childress, J. M. Taylor, A. S. Sorensen, and M. D. Lukin. Fault-tolerant quantum communication based on solid-state photon emitters. *Phys. Rev. Lett.*, 96(7):070504, 2006.

[32] `http://qcvictoria.com/New-Products`, accessed December 2010.

[33] L. A. Stewart, Y. Zhai, J. M. Dawes, M. J. Steel, J. R. Rabeau, and M. J. Withford. Single photon emission from diamond nanocrystals in an opal photonic crystal. *Opt Express*, 17(20):18044, 2009.

[34] A. Beveratos, R. Brouri, T. Gacoin, A. Villing, J. P. Poizat, and P. Grangier. Single photon quantum cryptography. *Phys. Rev. Lett.*, 89(18):187901, 2002.

[35] Y.-R. Chang, H.-Y. Lee, K. Chen, C.-C. Chang, D.-S. Tsai, C.-C. Fu, T.-S. Lim, Y.-K. Tzeng, C.-Y. Fang, C.-C. Han, H.-C. Chang, and W. Fann. Mass production and dynamic imaging of fluorescent nanodiamonds. *Nature Nanotechnology*, 3(5):284, 2008.

[36] R. W. Keyes. Effect of randomness in distribution of impurity atoms on fet thresholds. *Appl Phys*, 8(3):251, 1975.

[37] T. Mizuno, J. Okamura, and A. Toriumi. Experimental-study of threshold voltage fluctuation due to statistical variation of channel dopant number in mosfets. *Ieee T Electron Dev*, 41(11):2216, 1994.

[38] A. Asenov. Random dopant induced threshold voltage lowering and fluctuations in sub-0.1 µm MOSFET's: A 3-D "atomistic" simulation study. *Ieee T Electron Dev*, 45(12):2505, 1998.

[39] T. Shinada, S. Okamoto, T. Kobayashi, and I. Ohdomari. Enhancing semiconductor device performance using ordered dopant arrays. *Nature*, 437(7062):1128, 2005.

[40] A. Asenov, A. R. Brown, J. H. Davies, S. Kaya, and G. Slavcheva. Simulation of intrinsic parameter fluctuations in decananometer and nanometer-scale MOSFETs. *Ieee T Electron Dev*, 50(9):1837, 2003.

[41] M. F. Bukhori, S. Roy, and A. Asenov. Simulation of statistical aspects of charge trapping and related degradation in bulk MOSFETs in the presence of random discrete dopants. *Ieee T Electron Dev*, 57(4):795, 2010.

[42] S. Rogge. Single dopants learn their place. *Nature Nanotechnology*, 5(2):100, 2010.

[43] M. Hori, T. Shinada, K. Taira, N. Shimamoto, T. Tanii, T. Endo, and I. Ohdomari. Performance enhancement of semiconductor devices by control of discrete dopant distribution. *Nanotechnology*, 20(36):365205, 2009.

[44] T. Shinada, H. Koyama, C. Hinoshita, K. Imamura, and I. Ohdomari. Improvement of focused ion-beam optics in single-ion implantation for higher aiming precision of one-by-one doping of impurity atoms into nano-scale semiconductor devices. *Jpn J Appl Phys*, 41(3A):L287, 2002.

[45] D. N. Jamieson, C. Yang, T. Hopf, S. M. Hearne, C. I. Pakes, S. Prawer, M. Mitic, E. Gauja, S. E. Andresen, F. E. Hudson, A. S. Dzurak, and R. G. Clark. Controlled shallow single-ion implantation in silicon using an active substrate for sub-20-keV ions. *Appl. Phys. Lett.*, 86(20):202101, 2005.

[46] C. D. Weis, A. Schuh, A. Batra, A. Persaud, I. W. Rangelow, J. Bokor, C. C. Lo, S. Cabrini, E. Sideras-Haddad, G. D. Fuchs, R. Hanson, D. D. Awschalom, and

T. Schenkel. Single atom doping for quantum device development in diamond and silicon. *J Vac Sci Technol B*, 26(6):2596, 2008.

[47] C. D. Weis, A. Schuh, A. Batra, A. Persaud, I. W. Rangelow, J. Bokor, C. C. Lo, S. Cabrini, D. Olynick, S. Duhey, and T. Schenkel. Mapping of ion beam induced current changes in FinFETs. *Nucl Instrum Meth B*, 267(8-9):1222, 2009.

[48] J. A. van Donkelaar, A. D. Greentree, A. D. C. Alves, L. M. Jong, L. C. L. Hollenberg, and D. N. Jamieson. Top-down pathways to devices with few and single atoms placed to high precision. *New J Phys*, 12:065016, 2010.

[49] A. Persaud, S. J. Park, J. A. Liddle, T. Schenkel, J. Bokor, and I. W. Rangelow. Integration of scanning probes and ion beams. *Nano Lett.*, 5(6):1087, 2005.

[50] A. Persaud, J. A. Liddle, T. Schenkel, J. Bokor, T. Ivanov, and I. W. Rangelow. Ion implantation with scanning probe alignment. *J Vac Sci Technol B*, 23(6):2798, 2005.

[51] T. Schenkel, J. A. Liddle, J. Bokor, A. Persaud, S. J. Park, J. Shangkuan, C. C. Lo, S. Kwon, S. A. Lyon, A. M. Tyryshkin, I. W. Rangelow, Y. Sarov, D. H. Schneider, J. Ager, and R. de Sousa. Strategies for integration of donor electron spin qubits in silicon. *Microelectron Eng*, 83(4-9):1814, 2006.

[52] W. J. MoberlyChan, D. P. Adams, M. J. Aziz, G. Hobler, and T. Schenkel. Fundamentals of focused ion beam nanostructural processing: Below, at, and above the surface. *Mrs Bull*, 32(5):424, 2007.

[53] T. Schenkel, V. Radmilovic, E. A. Stach, S. J. Park, and A. Persaud. Formation of a few nanometer wide holes in membranes with a dual beam focused ion beam system. *J Vac Sci Technol B*, 21(6):2720, 2003.

[54] J. Meijer, S. Pezzagna, T. Vogel, B. Burchard, H. H. Bukow, I. W. Rangelow, Y. Sarov, H. Wiggers, I. Pluemel, F. Jelezko, J. Wrachtrup, F. Schmidt-Kaler, W. Schnitzler, and K. Singer. Towards the implanting of ions and positioning of nanoparticles with nm spatial resolution. *Appl Phys A-Mater*, 91(4):567, 2008.

[55] A. Persaud, F. I. Allen, F. Gicclueł, S. J. Park, J. A. Liddle, T. Schenkel, T. Ivanov, K. Ivanova, I. W. Rangelow, and J. Bokor. Single ion implantation with scanning probe alignment. *J Vac Sci Technol B*, 22(6):2992, 2004.

[56] A. Persaud, S. J. Park, J. A. Liddle, I. W. Rangelow, J. Bokor, R. Keller, F. I. Allen, D. H. Schneider, and T. Schenkel. Quantum computer development with single ion implantation. *Quantum Information Processing*, 3(1-5):223, 2004.

[57] M. Mitic, S. E. Andresen, C. Yang, T. Hopf, V. Chan, E. Gauja, F. E. Hudson, T. M. Buehler, R. Brenner, A. J .Ferguson, C. I. Pakes, S. M. Hearne, G. Tamanyan, D. J. Reilly, A. R. Hamilton, D. N. Jamieson, A. S. Dzurak, and R. G. Clark. Single atom Si nanoelectronics using controlled single-ion implantation. *Microelectron Eng*, 78-79:279, 2005.

[58] J. A. Seamons, E. Bielejec, M. S. Carroll, and K. D. Childs. Room temperature single ion detection with geiger mode avalanche diode detectors. *Appl. Phys. Lett.*, 93(4):043124, 2008.

[59] E. Bielejec, J. A. Seamons, and M. S. Carroll. Single ion implantation for single donor devices using geiger mode detectors. *Nanotechnology*, 21(8):085201, 2010.

[60] A. Batra, C. D. Weis, J. Reijonen, A. Persaud, S. Cabrini, C. C. Lo, J. Bokor, and T. Schenkel. Detection of low energy single ion impacts in micron scale transistors at room temperature. *Appl. Phys. Lett.*, 91(19):193502, 2007.

[61] T. Shinada, T. Kurosawa, H. Nakayama, Y. Zhu, M. Hori, and I.Ohdomari. A reliable method for the counting and control of single ions for single-dopant controlled devices. *Nanotechnology*, 19(34):345202, 2008.

[62] B. C. Johnson, G. C. Tettamanzi, A. D. C. Alves, S. Thompson, C. Yang, J. Verduijn, J. A. Mol, R. Wacquez, M. Vinet, M. Sanquer, S. Rogge, and D. N. Jamieson. Drain current modulation in a nanoscale field-effect-transistor channel by single dopant implantation. *Appl. Phys. Lett.*, 96(26):264102, 2010.

[63] M. Y. Simmons, F. J. Ruess, K. E. J. Goh, T. Hallam, S. R. Schofield, L. Oberbeck, N. J. Curson, A. R. Hamilton, M. J. Butcher, R. G. Clark, and T. C. G. Reusch. Scanning probe microscopy for silicon device fabrication. *Mol Simulat*, 31(6-7):505, 2005.

[64] M. Y. Simmons, F. J. Ruess, K. E. J. Goh, W. Pok, T. Hallam, M. J. Butcher, T. C. G. Reusch, and G. Scappucci. Atomic-scale silicon device fabrication. *Int J Nanotechnol*, 5(2-3):352, 2008.

[65] J. Meijer, T. Vogel, B. Burchard, I. W. Rangelow, L. Bischoff, J. Wrachtrup, M. Domhan, F. Jelezko, W. Schnitzler, S. A. Schulz, K. Singer, and F. Schmidt-Kaler. Concept of deterministic single ion doping with sub-nm spatial resolution. *Appl Phys A-Mater*, 83(2):321, 2006.

[66] W. Schnitzler, N. M. Linke, R. Fickler, J. Meijer, F. Schmidt-Kaler, and K. Singer. Deterministic ultracold ion source targeting the Heisenberg limit. *Phys. Rev. Lett.*, 102(7):070501, 2009.

[67] W. Schnitzler, G. Jacob, R. Fickler, F. Schmidt-Kaler, and K. Singer. Focusing a deterministic single-ion beam. *New J Phys*, 12:065023, 2010.

[68] J. Meijer, B. Burchard, M. Domhan, C. Wittmann, T. Gaebel, I. Popa, F. Jelezko, and J. Wrachtrup. Generation of single color centers by focused nitrogen implantation. *Appl. Phys. Lett.*, 87(26):261909, 2005.

[69] P. Spinicelli, A. Dreau, L. Rondin, F. Silva, J. Achard, S. Xavier, S. Bansropun, T. Debuisschert, S. Pezzagna, J. Meijer, V. Jacques, and J.-F. Roch. Engineered arrays of nitrogen-vacancy color centers in diamond based on implantation of CN-molecules through nanoapertures. *New J Phys*, 13:025014, 2011.

[70] D. M. Toyli, C. D. Weis, G. D. Fuchs, T. Schenkel, and D. D. Awschalom. Chip-scale nanofabrication of single spins and spin arrays in diamond. *Nano Lett.*, 10(8):3168, 2010.

[71] S. Pezzagna, B. Naydenov, F. Jelezko, J. Wrachtrup, and J. Meijer. Creation efficiency of nitrogen-vacancy centres in diamond. *New J Phys*, 12:065017, 2010.

[72] B. Naydenov, F. Reinhard, A. Laemmle, V. Richter, R. Kalish, U. F. S. D'Haenens-Johansson, M. Newton, F. Jelezko, and J. Wrachtrup. Increasing the coherence time of single electron spins in diamond by high temperature annealing. *Appl. Phys. Lett.*, 97(24):242511, 2010.

[73] G. D. Fuchs, V. V. Dobrovitski, R. Hanson, A. Batra, C. D. Weis, T. Schenkel, and D. D. Awschalom. Excited-state spectroscopy using single spin manipulation in diamond. *Phys. Rev. Lett.*, 101(11):117601, 2008.

[74] J. R. Rabeau, P. Reichart, G. Tamanyan, D. N. Jamieson, S. Prawer, F. Jelezko, T. Gaebel, I. Popa, M. Domhan, and J. Wrachtrup. Implantation of labelled single nitrogen vacancy centers in diamond using N-15. *Appl. Phys. Lett.*, 88(2):023113, 2006.

[75] G. D. Fuchs, V. V. Dobrovitski, D. M. Toyli, F. J. Heremans, C. D. Weis, T. Schenkel, and D. D. Awschalom. Excited-state spin coherence of a single nitrogen-vacancy centre in diamond. *Nature Physics*, 6(9):668, 2010.

[76] M. V. Hauf, B. Grotz, B. Naydenov, M. Dankerl, S. Pezzagna, J. Meijer, F. Jelezko, J. Wrachtrup, M. Stutzmann, F. Reinhard, and J. A. Garrido. Chemical control of the charge state of nitrogen-vacancy centers in diamond. *Phys Rev B*, 83(8):081304, 2011.

[77] J. Schwartz, P. Michaelides, C. D. Weis, and T. Schenkel. In situ optimization of co-implantation and substrate temperature conditions for nitrogen-vacancy center formation in single-crystal diamonds. *New J Phys*, 13:035022, 2011.

[78] S. Pezzagna, D. Wildanger, P. Mazarov, A. D. Wieck, Y. Sarov, I. Rangelow, B. Naydenov, F. Jelezko, S. W. Hell, and J. Meijer. Nanoscale engineering and optical addressing of single spins in diamond. *Small*, 6(19):2117, 2010.

[79] S. W. Hell and J. Wichmann. Breaking the diffraction resolution limit by stimulated-emission-depletion fluorescence microscopy. *Optics Letters*, 19(11):780, 1994.

[80] S. Pezzagna, D. Rogalla, D. Wildanger, J. Meijer, and A. Zaitsev. Creation and nature of optical centers in diamond for single-photon emission-overview and critical remarks. *New J Phys*, 13:035024, 2011.

[81] C. C. Lo, J. Bokor, T. Schenkel, A. M. Tyryshkin, and S. A. Lyon. Spin-dependent scattering off neutral antimony donors in Si-28 field-effect transistors. *Appl. Phys. Lett.*, 91(24):242106, 2007.

[82] C. C. Lo, V. Lang, R. E. George, J. J. L. Morton, A. M. Tyryshkin, S. A. Lyon, J. Bokor, and T. Schenkel. Electrically detected magnetic resonance of neutral donors interacting with a two-dimensional electron gas. *Phys. Rev. Lett.*, 106(20):207601, 2011.

[83] M. A. Nielsen and I. L. Chuang. *Quantum Computation and Quantum Information*. Cambridge University Press, 1st edition, October 2000.

[84] D. McMahon. *Quantum Computing Explained*. Wiley-IEEE Computer Society Pr, December 2007.

[85] J. F. Ziegler, J. P. Biersack, and M. D. Ziegler. *SRIM - The Stopping and Range of Ions in Matter*. SRIM Co., Chester, Maryland (USA), 2008.

[86] R. P. Feynman. Simulation physics with computers. *Int J Theor Phys*, 21(6-7):467, 1982.

[87] D. Deutsch. Quantum-Theory, the Church-Turing principle and the universal quantum computer. *P Roy Soc Lond A Mat*, 400(1818):97, 1985.

[88] F. Shi, X. Rong, N. Xu, Y. Wang, J. Wu, B. Chong, X. Peng, J. Kniepert, R.-S. Schoenfeld, W. Harneit, M. Feng, and J. Du. Room-temperature implementation of the Deutsch-Jozsa algorithm with a single electronic spin in diamond. *Phys. Rev. Lett.*, 105(4):040504, 2010.

[89] L. M. K. Vandersypen, M. Steffen, G. Breyta, C. S. Yannoni, M. H. Sherwood, and I. L. Chuang. Experimental realization of Shor's quantum factoring algorithm using nuclear magnetic resonance. *Nature*, 414(6866):883, 2001.

[90] B. P. Lanyon, T. J. Weinhold, N. K. Langford, M. Barbieri, D. F. V. James, A. Gilchrist, and A. G. White. Experimental demonstration of a compiled version of Shor's algorithm with quantum entanglement. *Phys. Rev. Lett.*, 99(25):250505, 2007.

[91] C.-Y. Lu, D. E. Browne, T. Yang, and J.-W. Pan. Demonstration of a compiled version of Shor's quantum factoring algorithm using photonic qubits. *Phys. Rev. Lett.*, 99(25):250504, 2007.

[92] D. P. DiVincenzo. The physical implementation of quantum computation. *Fortschr Phys*, 48(9-11):771, 2000.

[93] M. Nakahara, S. Kanemitsu, M. M. Salomaa, and S. Takagi. *Physical Realization of Quantum Computing*. World Scientific, 2006.

[94] D. Gottesman. `http://www.perimeterinstitute.ca/personal/dgottesman/FTreqs.ppt`, accessed December 2010.

[95] J. Preskill. Fault-tolerant quantum computation. *arXiv*, 9712048v1, 1997.

[96] G. Binnig and H. Rohrer. Scanning tunneling microscopy. *Surf Sci*, 126(1-3):236, 1983.

[97] `http://nobelprize.org/nobel_prizes/physics/laureates/1986/`, accessed May 2011.

[98] J. R. Matey and J. Blanc. Scanning capacitance microscopy. *J Appl Phys*, 57(5):1437, 1985.

[99] M. Nonnenmacher, M. P. Oboyle, and H. K. Wickramasinghe. Kelvin probe microscopy. *Appl. Phys. Lett.*, 58(25):2921, 1991.

[100] E. Betzig, J. K. Trautman, T. D. Harris, J. S. Weiner, and R. L. Kostelak. Breaking the diffraction barrier - Optical microscopy on a nanometer scale. *Science*, 251(5000):1468, 1991.

[101] G. Binnig, C. F. Quate, and C. Gerber. Atomic force microscope. *Phys. Rev. Lett.*, 56(9):930–933, 1986.

[102] J. P. Cleveland, Manne S, D. Bocek, and P. K. Hansma. A nondestructive method for determining the spring constant of cantilevers for scanning force microscopy. *Rev Sci Instrum*, 64(2):403, 1993.

[103] J. E. Sader, J. W. M. Chon, and P. Mulvaney. Calibration of rectangular atomic force microscope cantilevers. *Rev Sci Instrum*, 70(10):3967, 1999.

[104] H. J. Butt and M. Jaschke. Calculation of thermal noise in atomic-force microscopy. *Nanotechnology*, 6(1):1, 1995.

[105] B. Ohler. Cantilever spring constant calibration using laser Doppler vibrometry. *Rev Sci Instrum*, 78(6):063701, 2007.

[106] I. W. Rangelow. Scanning proximity probes for nanoscience and nanofabrication. *Microelectron Eng*, 83(4-9):1449, 2006.

[107] M. Tortonese, R. C. Barrett, and C. F. Quate. Atomic resolution with an atomic force microscope using piezoresistive detection. *Appl. Phys. Lett.*, 62(8):834, 1993.

[108] R. Linnemann, T. Gotszalk, L. Hadjiiski, and I. W. Rangelow. Characterization of a cantilever with an integrated deflection sensor. *Thin Solid Films*, 264(2):159, 1995.

[109] T. Gotszalk, P. Grabiec, and I. W. Rangelow. Piezoresistive sensors for scanning probe microscopy. *Ultramicroscopy*, 82(1-4):39, 2000.

[110] L. C. Feldman, J. W. Mayer, and S. T. Picraux. *Materials Analysis by Ion Channeling*. Academic Press, 1982.

[111] G. Carter and J. S. Colligon. *Ion Bombardment of Solids*. American Elsevier, 1968.

[112] M. Nastasi and J. W. Mayer. *Ion Implantation and Synthesis of Materials*. Springer, Berlin Heidelberg, 2006.

[113] Y. Zengliang. *Introduction to Ion Beam Biotechnology*. Springer, 2006.

[114] H. Geiger and E. Marsden. On a diffuse reflection of the alpha-particles. *P R Soc Lond A-Conta*, 82(557):495, 1909.

[115] E. Rutherford. The scattering of $\alpha$ and $\beta$ particles by matter and the structure of the atom. *Philosophical Magazine Series 6*, 21(125):114, 1911.

[116] J. F. Ziegler, J. P. Biersack, and U. Littmark. *The Stopping Range of Ions in Matter*. SRIM, Co., Chester, MD, 2008.

[117] J. P. Biersack and L. G. Haggmark. A Monte-Carlo computer-program for the transport of energetic ions in amorphous targets. *Nucl Instrum Methods*, 174(1-2):257, 1980.

[118] U. Littmark and J. F. Ziegler. Ranges of energetic ions in matter. *Phys. Rev. A*, 23(1):64, 1981.

[119] `http://www-rsicc.ornl.gov/codes/psr/psr1/psr-137.html`, accessed May 2011.

[120] M. T. Robinson and I. M. Torrens. Computer-simulation of atomi-displacement cascades in solids in binary-collision approximation. *Phys. Rev. B*, 9(12):5008, 1974.

[121] M. T. Robinson. The temporal development of collision cascades in the binary-collision approximation. *Nucl Instrum Meth B*, 48(1-4):408, 1990.

[122] `http://www.silvaco.com/products/process_simulation/athena.html`, accessed May 2011.

[123] `http://www.eaglabs.com`.

[124] Private communication S. A. Lyon and A. M. Tyryshkin.

[125] T. Schenkel, A. V. Hamza, A. V. Barnes, and D. H. Schneider. Interaction of slow, very highly charged ions with surfaces. *Prog Surf Sci*, 61(2-4):23, 1999.

[126] T. Shinada, A. Ishikawa, M. Fujita, K. Yamashita, and I. Ohdomari. Influence of secondary electron detection efficiency on controllability of dopant ion number in single ion implantation. *Jpn J Appl Phys*, 38(6A):3419, 1999.

[127] D. Loss and D. P. DiVincenzo. Quantum computation with quantum dots. *Phys. Rev. A*, 57(1):120, 1998.

[128] J. R. Petta, A. C. Johnson, J. M. Taylor, E. A. Laird, A. Yacoby, M. D. Lukin, C. M. Marcus, M. P. Hanson, and A. C. Gossard. Coherent manipulation of coupled electron spins in semiconductor quantum dots. *Science*, 309(5744):2180, 2005.

[129] R. Hanson, L. P. Kouwenhoven, J. R. Petta, S. Tarucha, and L. M. K. Vandersypen. Spins in few-electron quantum dots. *Rev. Mod. Phys.*, 79(4):1217, 2007.

[130] D. Press, T. D. Ladd, B. Zhang, and Y. Yamamoto. Complete quantum control of a single quantum dot spin using ultrafast optical pulses. *Nature*, 456(7219):218, 2008.

[131] C. B. Simmons, J. R. Prance, B. J. Van Bael, T. S. Koh, Z. Shi, D. E. Savage, M. G. Lagally, R. Joynt, M. Friesen, S. N. Coppersmith, and M. A. Eriksson. Tunable spin loading and T-1 of a silicon spin qubit measured by single-shot readout. *Phys. Rev. Lett.*, 106(15):156804, 2011.

[132] H. Liu, T. Fujisawa, H. Inokawa, Y. Ono, A. Fujiwara, and Y. Hirayama. A gate-defined silicon quantum dot molecule. *Appl. Phys. Lett.*, 92(22):222104, 2008.

[133] L. A. Tracy, E. P. Nordberg, R. W. Young, C. B. Pinilla, H. L. Stalford, G. A. Ten Eyck, K. Eng, K. D. Childs, J. R. Wendt, R. K. Grubbs, J. Stevens, M. P. Lilly, M. A. Eriksson, and M. S. Carroll. Double quantum dot with tunable coupling in an enhancement-mode silicon metal-oxide semiconductor device with lateral geometry. *Appl. Phys. Lett.*, 97(19):192110, 2010.

[134] T. Schenkel, J. A. Liddle, A. Persaud, A. M. Tyryshkin, S. A. Lyon, R. de Sousa, K. B. Whaley, J. Bokor, J. Shangkuan, and I. Chakarov. Electrical activation and electron spin coherence of ultralow dose antimony implants in silicon. *Appl. Phys. Lett.*, 88(11):112101, 2006.

[135] A. M. Tyryshkin and S. A. Lyon. Electron spin coherence of phosphorus donors in high-purity 28Si silicon. In *Data presented at the Silicon Qubit Workshop at Sandia National Laboratories*, Albuquerque, NM, August 2010.

[136] A. M. Tyryshkin, S. Tojo, J. J. L. Morton, H. Riemann, N. V. Abrosimov, P. Becker, H.-J. Pohl, T. Schenkel, M. L. W. Thewalt, K. M. Itoh, and S. A. Lyon. Electron spin coherence exceeding seconds in high purity silicon. *arXiv*, 1105.3772v1, 2011.

[137] G. Feher. Electron spin resonance experiments on donors in silicon. 1. Electronic structure of donors by the electron nuclear double resonance technique. *Phys Rev*, 114(5):1219, 1959.

[138] J. J. L. Morton, A. M. Tyryshkin, R. M. Brown, S. Shankar, B. W. Lovett, A. Ardavan, T. Schenkel, E. E. Haller, J. W. Ager, and S. A. Lyon. Solid-state quantum memory using the P-31 nuclear spin. *Nature*, 455(7216):1085, 2008.

[139] L. C. L. Hollenberg, C. J. Wellard, C. I. Pakes, and A. G. Fowler. Single-spin readout for buried dopant semiconductor qubits. *Phys. Rev. B*, 69(23):233301, 2004.

[140] A. D. Greentree, A. R. Hamilton, L. C. L. Hollenberg, and R. G. Clark. Electrical readout of a spin qubit without double occupancy. *Phys. Rev. B*, 71(11):113310, 2005.

[141] A. R. Stegner, C. Boehme, H. Huebl, M. Stutzmann, K. Lips, and M. S. Brandt. Electrical detection of coherent P-31 spin quantum states. *Nature Physics*, 2(12):835, 2006.

[142] M. Sarovar, K. C. Young, T. Schenkel, and K. B. Whaley. Quantum nondemolition measurements of single donor spins in semiconductors. *Phys. Rev. B*, 78(24):245302, 2008.

[143] A. Morello, J. J. Pla, F. A. Zwanenburg, K. W. Chan, K. Y. Tan, H. Huebl, M. Mottonen, C. D. Nugroho, C. Yang, J. A. van Donkelaar, A. D. C. Alves, D. N. Jamieson, C. C. Escott, L. C. L. Hollenberg, R. G. Clark, and A. S. Dzurak. Single-shot readout of an electron spin in silicon. *Nature*, 467(7316):687, 2010.

[144] A. Morello, C. C. Escott, H. Huebl, L. H. W. van Beveren, L. C. L. Hollenberg, D. N. Jamieson, A. S. Dzurak, and R. G. Clark. Architecture for high-sensitivity single-shot readout and control of the electron spin of individual donors in silicon. *Phys. Rev. B*, 80(8):081307, 2009.

[145] D. R. Mccamey, J. Van Tol, G. W. Morley, and C. Boehme. Electronic spin storage in an electrically readable nuclear spin memory with a lifetime $> 100$ seconds. *Science*, 330(6011):1652, 2010.

[146] H. Bracht. Diffusion mechanisms and intrinsic point-defect properties in silicon. *Mrs Bull*, 25(6):22, 2000.

[147] J. Dabrowski, H. J. Mussig, V. Zavodinsky, R. Baierle, and M. J. Caldas. Mechanism of dopant segregation to $SiO_2$/Si(001) interfaces. *Phys. Rev. B*, 65(24):245305, 2002.

[148] L. H. Wei, P. K. Kuo, R. L. Thomas, T. R. Anthony, and W. F. Banholzer. Thermal-conductivity of isotopically modified single-crystal diamond. *Phys. Rev. Lett.*, 70(24):3764, 1993.

[149] G. A. J. Amaratunga. A dawn for carbon etectronics? *Science*, 297(5587):1657, 2002.

[150] S. J. Sque, R. Jones, J. P. Goss, and P. R. Briddon. Shallow donors in diamond: Chalcogens, pnictogens, and their hydrogen complexes. *Phys. Rev. Lett.*, 92(1):017402, 2004.

[151] M. W. Geis, N. N. Efremow, and D. D. Rathman. Device applications of diamonds. *J Vac Sci Technol A*, 6(3):1953, 1988.

[152] R. J. Trew, J. B. Yan, and P. M. Mock. The potential of diamond and sic electronic devices for microwave and millimeter-wave power applications. *P Ieee*, 79(5):598, 1991.

[153] K. Shenai, R. S. Scott, and B. J. Baliga. Optimum semiconductors for high-power electronics. *Ieee T Electron Dev*, 36(9):1811, 1989.

[154] J. Isberg, J. Hammersberg, E. Johansson, T. Wikstrom, D. J. Twitchen, A. J. Whitehead, S. E. Coe, and G. A. Scarsbrook. High carrier mobility in single-crystal plasma-deposited diamond. *Science*, 297(5587):1670, 2002.

[155] A. Gruber, A. Drabenstedt, C. Tietz, L. Fleury, J. Wrachtrup, and C. von Borczyskowski. Scanning confocal optical microscopy and magnetic resonance on single defect centers. *Science*, 276(5321):2012, 1997.

[156] P. Neumann, N. Mizuochi, F. Rempp, P. Hemmer, H. Watanabe, S. Yamasaki, V. Jacques, T. Gaebel, F. Jelezko, and J. Wrachtrup. Multipartite entanglement among single spins in diamond. *Science*, 320(5881):1326, 2008.

[157] R. Hanson, O. Gywat, and D. D. Awschalom. Room-temperature manipulation and decoherence of a single spin in diamond. *Phys. Rev. B*, 74(16):161203, 2006.

[158] N. Mizuochi, P. Neumann, F. Rempp, J. Beck, V. Jacques, P. Siyushev, K. Nakamura, D. Twitchen, H. Watanabe, S. Yamasaki, F. Jelezko, and J. Wrachtrup. Coherence of single spins coupled to a nuclear spin bath of varying density. *Phys. Rev. B*, 80(4):041201, 2009.

[159] G. D. Fuchs, V. V. Dobrovitski, D. M. Toyli, F. J. Heremans, and D. D. Awschalom. Gigahertz dynamics of a strongly driven single quantum spin. *Science*, 326(5959):1520, 2009.

[160] B. Smeltzer, J. McIntyre, and L. Childress. Robust control of individual nuclear spins in diamond. *Phys Rev A*, 80(5):050302, 2009.

[161] M. Mehring, J. Mende, and W. Scherer. Entanglement between an electron and a nuclear spin 1/2. *Phys. Rev. Lett.*, 90(15):153001, 2003.

[162] P. Neumann, R. Kolesov, B. Naydenov, J. Beck, F. Rempp, M. Steiner, V. Jacques, G. Balasubramanian, M. L. Markham, D. J. Twitchen, S. Pezzagna, J. Meijer, J. Twamley, F. Jelezko, and J. Wrachtrup. Quantum register based on coupled electron spins in a room-temperature solid. *Nature Physics*, 6(4):249, 2010.

[163] J. O. Orwa, A. D. Greentree, I. Aharonovich, A. D. C. Alves, J. Van Donkelaar, A. Stacey, and S. Prawer. Fabrication of single optical centres in diamond - A review. *Journal of Luminescence*, 130(9):1646, 2010.

[164] Alexander M. Zaitsev. *Optical properties of diamond: A data handbook*. Springer, 2010.

[165] G. Balasubramanian, P. Neumann, D. Twitchen, M. Markham, R. Kolesov, N. Mizuochi, J. Isoya, J. Achard, J. Beck, J. Tissler, V. Jacques, P. R. Hemmer, F. Jelezko, and J. Wrachtrup. Ultralong spin coherence time in isotopically engineered diamond. *Nature Materials*, 8(5):383, 2009.

[166] B. Naydenov, V. Richter, J. Beck, M. Steiner, P. Neumann, G. Balasubramanian, J. Achard, F. Jelezko, J. Wrachtrup, and R. Kalish. Enhanced generation of single optically active spins in diamond by ion implantation. *Appl. Phys. Lett.*, 96(16):163108, 2010.

[167] A. Lenef and S. C. Rand. Reply to "comment on 'electronic structure of the N-V center in diamond: Theory'". *Phys. Rev. B*, 56(24):16033, 1997.

[168] G. Waldherr, J. Beck, M. Steiner, P. Neumann, A. Gali, Th. Frauenheim, F. Jelezko, and J. Wrachtrup. Dark states of single NV centers in diamond unraveled by single shot NMR. *arXiv*, 1012.5017v2, 2010.

[169] J. R. Weber, W. F. Koehl, J. B. Varley, A. Janotti, B. B. Buckley, C. G. Van de Walle, and D. D. Awschalom. Quantum computing with defects. *P Natl Acad Sci USA*, 107(19):8513, 2010.

[170] J. Reijonen, M. Eardley, R. Gough, K. Leung, and R. Thomae. Microwave ion source for low charge state ion production. *Nuc Instr Meth A*, 511:301, 2003.

[171] Q. Ji. Compact permanent magnet microwave-driven neutron generator. accepted for publication, AIP Conference Proceedings 2011 (CAARI 2010), Volume 1336.

[172] T. Schenkel, A. Persaud, A. Kraemer, J. W. McDonald, J. P. Holder, A. V. Hamza, and D. H. Schneider. Extraction of highly charged ions from the electron beam ion trap at LBNL for applications in surface analysis and materials science. *Rev Sci Instrum*, 73(2):663, 2002.

[173] A. Persaud. *Aligned Ion Implantation using Scanning Probes*. PhD thesis, Johann Wolfgang Goethe - Universität, 2006.

[174] M. A. Levine, R. E. Marrs, J. R. Henderson, D. A. Knapp, and M. B. Schneider. The electron-beam ion trap - A new instrument for atomic physics measurements. *Phys. Scr.*, T22:157, 1988.

[175] I. W. Rangelow, P. Grabiec, T. Gotszalk, and K. Edinger. Piezoresistive SXM sensors. *Surf Interface Anal*, 33(2):59, 2002.

[176] T. Schenkel, A. Persaud, S. J. Park, J. Meijer, J. R. Kingsley, J. W. McDonald, J. P. Holder, J. Bokor, and D. H. Schneider. Single ion implantation for solid state quantum computer development. *J Vac Sci Technol B*, 20(6):2819, 2002.

[177] R. Geller, P. Ludwig, and G. Melin. Metal-ion production in ECRIS. *Rev Sci Instrum*, 63(4):2795, 1992.

[178] H. Koivisto, J. Arje, and M. Nurmia. Metal-ion beams from an ECR ion-source using volatile compounds. *Nucl Instrum Meth B*, 94(3):291, 1994.

[179] H. Koivisto, J. Arje, R. Seppala, and M. Nurmia. Production of titanium ion beams in an ECR ion source. *Nucl Instrum Meth B*, 187(1):111, 2002.

[180] K. E. Stiebing, S. Biri, J. Arje, F. Ditroi, H. Koivisto, J. Palinkas, L. Schmidt, and A. Valek. Highly charged metal ions by placing a ferrocene container inside the ECR ion source. *Phys. Scr.*, T80B:509, 1999.

[181] T. Nakagawa, J. Arje, Y. Miyazawa, M. Hemmi, T. Chiba, N. Inabe, M. Kase, T. Kageyama, O. Kamigaito, M. Kidera, A. Goto, and Y. Yano. Production of intense beams of highly charged metallic ions from RIKEN 18 GHz electron cyclotron resonance ion source. *Rev Sci Instrum*, 69(2):637, 1998.

[182] A. Ullrich, P. Grubling, and G. Zschornack. Production of 3d metal ion electron cyclotron resonance plasmas and ion beams using volatile compounds, 1998.

[183] H. Koivisto, J. Arje, and M. Nurmia. Metal ions from the volatile compounds method for the production of metal ion beams. *Rev Sci Instrum*, 69(2):785, 1998.

[184] `http://www.sigmaaldrich.com/catalog/ProductDetail.do?D7=0&N5=SEARCH_CONCAT_PNO|BRAND_KEY&N4=470732|ALDRICH&N25=0&QS=ON&F=SPEC`, accessed April 2011.

[185] P. J. Sellin, A. W. Davies, F. Boroumand, A. Lohstroh, M. E. Özsan, J. Parkin, and M. Veale. *Semiconductors.*

[186] G. Vizkelethy, B. Doyle, D. Brice, P. Dodd, M. Shaneyfelt, and J. Schwank. *Nuc Instr Meth B.*

[187] M. B. H. Breese, D. N. Jamieson, and P. J. C. King. *Materials Analysis Using a Nuclear Microprobe.* John Willy & Sons, New York, 1996 (and references therein).

[188] C. C. Lo. *Electrical detection of spin-dependent transport in silicon.* PhD thesis, University of California at Berkeley, 2011.

[189] C. C. Lo, A. Persaud, S. Dhuey, D. Olynick, F. Borondics, M. C. Martin, H. A. Bechtel, J. Bokor, and T. Schenkel. Device fabrication and transport measurements of FinFETs built with Si-28 SOI wafers toward donor qubits in silicon. *Semicond Sci Tech*, 24(10):105022, 2009.

[190] H. F. Winters and J. W. Coburn. The etching of silicon with $XeF_2$ vapor. *Applied Physics Letters*, 34:70, 1979.

[191] S. J. Randolph, J. D. Fowlkes, and P. D. Rack. Focused electron-beam-induced etching of silicon dioxide. *J Appl Phys*, 98(3):034902, 2005.

[192] T. Schenkel, C. C. Lo, C. D. Weis, A. Schuh, A. Persaud, and J. Bokor. Critical issues in the formation of quantum computer test structures by ion implantation. *Nucl Instrum Meth B*, 267(16):2563, 2009.

[193] A. Schuh. Detection and imaging of single ion impact arrays in field effect transistors. Master's thesis, Technical University of Ilmenau (Germany), 2009.

[194] T. A. Ma and P. V. Dressendorfer. *Ionizing Radiation Effects in MOS Devices & Circuits*. Wiley, New York, 1989.

[195] G. A. Ausman Jr. and F. B. McLean. Electron-hole pair creation energy in $SiO_2$. *Applied Physics Letters*, 26(4):173, 1975.

[196] D. R. Mccamey, H. Huebl, M. S. Brandt, W. D. Hutchison, J. C. McCallum, R. G. Clark, and A. R. Hamilton. Electrically detected magnetic resonance in ion-implanted Si:P nanostructures. *Appl. Phys. Lett.*, 89(18):182115, 2006.

[197] F. Hoehne, H. Huebl, B. Galler, M. Stutzmann, and M. S. Brandt. Spin-dependent recombination between phosphorus donors in silicon and $Si/SiO_2$ interface states investigated with pulsed electrically detected electron double resonance. *Phys. Rev. Lett.*, 104(4):046402, 2010.

[198] F. Hoehne, L. Dreher, H. Huebl, M. Stutzmann, and M. S. Brandt. Electrical detection of coherent nuclear spin oscillations in phosphorus-doped silicon using pulsed endor. *Phys. Rev. Lett.*, 106(18):187601, 2011.

[199] G. W. Morley, D. Mccamey, H. A. Seipel, L. C. Brunel, J. Van Tol, and C. Boehme. Long-lived spin coherence in silicon with an electrical spin trap readout. *Phys. Rev. Lett.*, 101(20):207602, 2008.

[200] M. Koh, K. Hara, K. Horita, B. Shigeta, T. Matsukawa, A. Kishida, T. Tanii, M. Goto, and I. Ohdomari. Development of the single-ion beam-induced charge (SIBIC) imaging technique using the single-ion microprobe system. *Nucl Instrum Meth B*, 93(1):82, 1994.

[201] M. Koh, B. Shigeta, K. Igarashi, T. Matsukawa, T. Tanii, S. Mori, and I. Ohdomari. Quantitative analysis of radiation induced $Si/SiO_2$ interface defects by means of MeV He single ion irradiation. *Appl. Phys. Lett.*, 68(11):1552, 1996.

[202] M. Koh, K. Horita, B. Shigeta, T. Matsukawa, A. Kishida, T. Tanii, S. Mori, and I. Ohdomari. Radiation immunity of pMOSFETs and nMOSFETs examined by means of MeV He single ion microprobe. *Appl Surf Sci*, 104:364, 1996.

[203] T. R. Oldham and F. B. McLean. Total ionizing dose effects in MOS oxides and devices. *Ieee T Nucl Sci*, 50(3):483, 2003.

[204] R. Koga, W. R. Crain, K. B. Crawford, D. D. Lau, S. D. Pinkerton, B. K. Yi, and R. Chitty. On the suitability of non-hardened high-density srams for space applications. *Ieee T Nucl Sci*, 38(6):1507, 1991.

[205] C. Dufour, P. Garnier, T. Carriere, J. Beaucour, R. Ecoffet, and M. Labrunee. Heavy-ion induced single hard errors on submicronic memories. *Ieee T Nucl Sci*, 39(6):1693, 1992.

[206] T. R. Oldham, K. W. Bennett, J. Beaucour, T. Carriere, C. Polvey, and P. Garnier. Total-dose failures in advanced electronics from single ions. *Ieee T Nucl Sci*, 40(6):1820, 1993.

[207] C. Poivey, T. Carriere, J. Beaucour, and T. R. Oldham. Characterization of single hard errors (SHE) in 1M-bit SRAMs from single-ion. *Ieee T Nucl Sci*, 41(6):2235, 1994.

[208] K. K. Hung, P. K. Ko, C. M. Hu, and Y. C. Cheng. Random telegraph noise of deep-submicrometer MOSFETs. *Ieee Electr Device L*, 11(2):90, 1990.

[209] M. V. Gurudev Dutt, L. Childress, L. Jiang, E. Togan, J. Maze, F. Jelezko, A. S. Zibrov, P. R. Hemmer, and M. D. Lukin. Quantum register based on individual electronic and nuclear spin qubits in diamond. *Science*, 316:1312, 2007.

[210] P. Neumann, N. Mizuochi, F. Rempp, P. Hemmer, H. Watanabe, S. Yamasaki, V. Jacques, T. Gaebel, F. Jelezko, and J. Wrachtrup. Multipartite entanglement among single spins in diamond. *Science*, 320:1326, 2009.

[211] J. Wrachtrup, S. Y. Kilin, and A. P. Nizovtsev. Quantum computation using the C-13 nuclear spins near the single NV defect center in diamond. *Opt Spectrosc*, 91(3):429, 2001.

[212] C. F. Wang, R. Hanson, D. D. Awschalom, E. L. Hu, T. Feygelson, J. Yang, and J. E. Butler. Fabrication and characterization of two-dimensional photonic crystal microcavities in nanocrystalline diamond. *Appl. Phys. Lett.*, 91(20):201112, 2007.

[213] C. F. Wang, Y.-S. Choi, J. C. Lee, E. L. Hu, J. Yang, and J. E. Butler. Observation of whispering gallery modes in nanocrystalline diamond microdisks. *Appl. Phys. Lett.*, 90:081110, 2007.

[214] P. E. Barclay, K.-M. C. Fu, C. Santori, and R. G. Beausoleil. Chip-based microcavities coupled to nitrogen-vacancy centers in single crystal diamond. *Appl. Phys. Lett.*, 95:191115, 2009.

[215] G. Davies. *Properties And Growth of Diamond*. INSPEC, 1994.

[216] G. Davies and M. F. Hamer. Optical studies of 1.945 eV vibronic band in diamond. *P Roy Soc Lond A Mat*, 348(1653):285, 1976.

[217] F. C. Waldermann, P. Olivero, J. Nunn, K. Surmacz, Z. Y. Wang, D. Jaksch, R. A. Taylor, I. A. Walmsley, M. Draganski, P. Reichart, A. D. Greentree, D. N. Jamieson, and S. Prawer. Creating diamond color centers for quantum optical applications. *Diam Relat Mater*, 16(11):1887, 2007.

[218] C. Santori, P. E. Barclay, K.-M. C. Fu, and R. G. Beausoleil. Vertical distribution of nitrogen-vacancy centers in diamond formed by ion implantation and annealing. *Phys. Rev. B*, 79(12):125313, 2009.

[219] L. Allers, A. T. Collins, and J. Hiscock. The annealing of interstitial-related optical centers in type II natural and CVD diamond. *Diam Relat Mater*, 7(2-5):228, 1998.

[220] J. A. van Wyk, E. C. Reynhardt, G. L. High, and I. Kiflawi. The dependences of ESR line widths and spin-spin relaxation times of single nitrogen defects on the concentration of nitrogen defects in diamond. *J Phys D Appl Phys*, 30(12):1790, 1997.

[221] B. R. Smith, D. W. Inglis, B. Sandnes, J. R. Rabeau, A. V. Zvyagin, D. Gruber, C. J. Noble, R. Vogel, E. Osawa, and T. Plakhotnik. Five-nanometer diamond with luminescent nitrogen-vacancy defect centers. *Small*, 5(14):1649, 2009.

[222] C. Bradac, T. Gaebel, N. Naidoo, M. J. Sellars, J. Twamley, L. J. Brown, A. S. Barnard, T. Plakhotnik, A. V. Zvyagin, and J. R. Rabeau. Observation and control of blinking nitrogen-vacancy centres in discrete nanodiamonds. *Nature Nanotechnology*, 5(5):345, 2010.

[223] T. van der Sar, E. C. Heeres, G. M. Dmochowski, G. de Lange, L. Robledo, T. H. Oosterkamp, and R. Hanson. Nanopositioning of a diamond nanocrystal containing a single nitrogen-vacancy defect center. *Appl. Phys. Lett.*, 94(17):173104, 2009.

[224] T. van der Sar, J. Hagemeier, W. Pfaff, E. C. Heeres, S. M. Thon, H. Kim, P. M. Petroff, T. H. Oosterkamp, D. Bouwmeester, and R. Hanson. Deterministic nanoassembly of a coupled quantum emitter-photonic crystal cavity system. *Appl. Phys. Lett.*, 98(19):193103, 2011.

[225] `http://www.e6cvd.com`.

[226] `http://www.sp3inc.com/wafers.htm`, accessed April 2011.

[227] O. Beffort, S. Vaucher, and F. A. Khalid. On the thermal and chemical stability of diamond during processing of Al/diamond composites by liquid metal infiltration (squeeze casting). *Diam Relat Mater*, 13(10):1834, 2004.

[228] G. Buchowicz, P. R. Stone, J. T. Robinson, C. D. Cress, J. W. Beeman, and O. D. Dubon. Correlation between structure and electrical transport in ion-irradiated graphene grown on Cu foils. *Appl. Phys. Lett.*, 98(3):032102, 2011.

[229] X. Liang, V. Giacometti, A. Ismach, B. D. Harteneck, D. L. Olynick, and S. Cabrini. Roller-style electrostatic printing of prepatterned few-layer-graphenes. *Appl. Phys. Lett.*, 96(1):013109, 2010.

[230] A. Ismach, C. Druzgalski, S. Penwell, A. Schwartzberg, M. Zheng, A. Javey, J. Bokor, and Y. Zhang. Direct chemical vapor deposition of graphene on dielectric surfaces. *Nano Lett.*, 10(5):1542, 2010.

[231] E. I. Cherepov, E. G. Tishkovsky, V. I. Obodnikov, J. N. Pal'yanov, A. G. Sokol, and N. V. Sobolev. Redistribution of nitrogen implanted in the crystals of synthetic diamond. *Nucl Instrum Meth B*, 183(3-4):301, 2001.

[232] T. E. Derry, R. W. Fearick, and J. P. F. Sellschop. Ion channeling in natural diamonds - Minimum yields. *Phys. Rev. B*, 24(7):3675, 1981.

[233] T. E. Derry, R. W. Fearick, and J. P. F. Sellschop. Ion channeling in natural diamond - Critical Angles. *Phys. Rev. B*, 26(1):17, 1982.

[234] R. W. Fearick, T. E. Derry, and J. P. F. Sellschop. Dechanneling of protons in diamond. *Phys. Rev. B*, 40(7, Part A):10704, SEP 1 1989.

[235] R. J. Schreutelkampa, V. Raineri, F. W. Sansa, R. E. Kaimb, J. F. M. Westendorp, P. F. H. M. van der Meulen, and K. T. F. Janssen. Channeling implantation of B and P in silicon. *Nucl Instrum Meth B*, 55:615, 1991.

# List of Figures

# List of Tables

# List of Abbreviations

| | |
|---|---|
| a-FET | accumulation Field Effect Transistor |
| AFM | Atomic Force Microscope |
| BCA | Binary Collision Approximation |
| box | Buried Oxide |
| CMOS | Complementary Metal-Oxide-Semiconductor |
| CVD | Chemical Vapor Deposition |
| DI | De-Ionized |
| DOS | Diamond on Silicon |
| ebeam | Electron Beam |
| EBIT | Electron Beam Ion Trap |
| EBS | Elastic Backscattering Spectroscopy |
| ECR | Electron Cyclotron Resonance |
| ERD | Elastic Recoil Detection |
| eV | Electron Volt |
| FET | Field Effect Transistor |
| FD | Force Distance |
| FIB | Focused Ion Beam |
| FinFET | Fin Field Effect Transistor |
| HFS | Hydrogen Forward Scattering Spectrometry |
| HOPG | Highly Ordered Pyrolytic Graphite |
| IBIC | Ion Beam Induced Charge |
| ITRS | International Technology Roadmap for Semiconductors |
| LBNL | Lawrence Berkeley National Laboratory |
| LTO | Low Temperature Oxide |
| n-FET | enhancement Field Effect Transistor |

| | |
|---|---|
| NA | Numerical Aperture |
| NMR | Nuclear Magnetic Resonance |
| NRA | Nuclear Reaction Analysis |
| NSA | National Security Agency |
| ODMR | Optically Detected Magnetic Resonance |
| PIXE | Particle Induced X-ray Emission |
| PL | Photo-Luminescence |
| ppb | Parts Per Billion ($10^{-9}$) |
| ppm | Parts Per Million |
| Qubit | Quantum Bit |
| RBS | Rutherford Back Scattering |
| RTA | Rapid Thermal Annealing |
| RTN | Random Telegraph Noise |
| SEM | Scanning Electron Microscope |
| SII | Single Ion Impacts |
| SIMS | Secondary Ion Mass Spectroscopy |
| SOI | Silicon on Insulator |
| SPM | Scanning Probe Microscope/microscopy |
| STED | Stimulated Emission Depletion |
| STM | Scanning Transmission Microscopy |
| VOC | Volatile Organic Compounds |

# Acknowledgments

First, I would like to thank Prof. Ivo Rangelow and Dr. Thomas Schenkel. As my thesis advisor, Ivo offered me the opportunity to conduct my entire research work abroad and allowed me to disappear for all these years. Thomas gave me the chance to work in his research group and supported and guided me throughout this work. Giving me all the possibilities to travel to conferences, participate in collaborations and sharing his philosophy about running and leading a research group and project management were greatly appreciated.

I would like to thank Cheuk Chi Lo for his help and advice about device layout and fabrication. His experience saved me from going through a lot of fabrication tests and working devices were obtained in the first device run. Further, in numerous discussions he shared his seemingly infinite wisdom about semiconductors with me. It should be mentioned that this did not only apply to areas of his expertise. Despite the fact that his hockey knowledge is quite the opposite, he never held back to join or initiate discussions about the major sport of his mother land and somehow managed to be spot wrong about pretty much anything. His persistence and vigor in refusing to accept hockey truths and reality is worth special mention.

Further thanks are to Arun Persaud for being a helpful predecessor on this project. He was a valuable resource discussing new and already attempted ideas. He also initiated our sort of weekly roller hockey games and without him I would have never gotten around to watch a flaming puck unicycle hockey game. He and Frances Allen were motivated, creative and skilled team members of our Berkeley Lab's Anonymous ⊠⊠⊠⊠⊠⊠⊠⊠ Building Team, setting scientific firsts and becoming part of LBNL's history.

I also would like to thank Arunabh Batra who was a great co-worker and always good for discussions about vapor pressures, boiling points and vintage shirts and thus made research days more than just enjoyable.

I would like to thank all the members of the Ion Beam Technology Group at LBNL throughout the years for offering enough distraction via stories and conversations that kept my sanity level in the more or less normal range and created a pleasant work atmosphere.

I would like to thank Michael Dickinson, Paul Wong, Steve Wilde and Tom McVeigh for their help, support and ideas with electrical and mechanical issues that arose during this work.

Finally, I want to thank the the UC Berkeley Microlab & Nanolab and LBNL Molecular Foundry staff for keeping the cleanrooms and their tools up and running and providing nanofabrication capabilities. Dealing mainly with current or future Ph.D. holders, who all have their own opinion and philosophy about cleanliness and tool treatment, disregarding the majority of simple but essential rules must be quiet a joy.

# List of Publications

- J. Schwartz, P. Michaelides, C. D. Weis, T. Schenkel. In situ optimization of co-implantation and substrate temperature conditions for nitrogen-vacancy center formation in single-crystal diamonds. New Journal of Physics **13**, 035022 (2011).

- G. D. Fuchs, V. V. Dobrovitski, D. M. Toyli, F. J. Heremans, C. D. Weis, T. Schenkel, D. D. Awschalom. Excited-state spin coherence of a single nitrogen-vacancy centre in diamond. Nature Physics **6** (9), 668 (2010).

- D. M. Toyli, C. D. Weis, G. D. Fuchs, T. Schenkel, D. D. Awschalom. Chip-Scale Nanofabrication of single spins and spin arrays in diamond. Nano Letters **10** (8), 3168 (2010).

- E. Sideras-Haddad, T. Schenkel, S. Shrivastava, T. Makgato, A. Batra, C. D. Weis, A. Persaud, R. Erasmus, B. Mwakikunga. Possible diamond-like nanoscale structures induced by slow highly-charged ions on graphite (HOPG). Nuclear Instruments & Methods in Physics Research **B 267** (16), 2774 (2009).

- T. Schenkel, C. C. Lo, C. D. Weis, A. Schuh, A. Persaud, J. Bokor. Critical issues in the formation of quantum computer test structures by ion implantation. Nuclear Instruments & Methods in Physics Research **B 267** (16), 2563 (2009).

- C. D. Weis, A. Schuh, A. Batra, A. Persaud, I. W. Rangelow, J. Bokor, C. C. Lo, S. Cabrini, D. Olynick, S. Duhey, T. Schenkel. Mapping of ion beam induced current changes in FinFETs. Nuclear Instruments & Methods in Physics Research **B 267** (8-9), 1222 (2009).

- C. D. Weis, A. Schuh, A. Batra, A. Persaud, I. W. Rangelow, J. Bokor, C. C. Lo, S. Cabrini, E. Sideras-Haddad, G. D. Fuchs, R. Hanson, D. D. Awschalom, T. Schenkel. Single-atom doping for quantum device development in diamond and silicon. Journal of Vacuum Science & Technology **B 26**(6), 2596 (2008).

- G. D. Fuchs, V. V. Dobrovitski, R. Hanson, A. Batra, C. D. Weis, T. Schenkel, D. D. Awschalom. Excited-state spectroscopy using single-spin manipulation in diamond. Physical Review Letters **101**, 117601 (2008).

- A. Batra, C. D. Weis, J. Reijonen, A. Persaud, S. Cabrini, C. C. Lo, J. Bokor, T. Schenkel. Detection of low energy single ion impacts in micron scale transistors at room temperature. Applied Physics Letters **91**, 193502 (2007).

- D. E. Starr, C. Weis, S. Yamamoto, A. Nilsson, H. Bluhm. $NO_2$ Adsorption on Ag(100) Supported MgO(100) Thin Films: Controlling the Adsorption State with Film Thickness. Journal of Physical Chemistry C **113** (17), 7355 (2009).

- X. Y. Deng, A. Verdaguer, T. Herranz, C. Weis, H. Bluhm, M. Salmeron. Surface chemistry of Cu in the presence of $CO_2$ and $H_2O$. Langmuir **24** (17), 9474 (2008).

- X. Deng, T. Herranz, C. Weis, H. Bluhm, M. Salmeron. Adsorption of water on $Cu_2O$ and $Al_2O_3$ thin films. Journal of Physical Chemistry C **112** (26), 9668 (2008).

- A. Verdaguer, C. Weis, G. Oncins, G. Ketteler, H. Bluhm, M. Salmeron. Growth and structure of water on $SiO_2$ films on Si investigated by Kelvin probe microscopy and in situ x-ray spectroscopies. Langmuir **23** (19), 9699 (2007).

# List of Conference Presentations

- C. D. Weis, A. Batra, C. C. Lo, A. Persaud, J. Bokor, T. Schenkel. Single Ion Implantation with Scanning Probe Alignment. *Contributed Poster:* Electrical Engineering & Computer Sciences Annual Research Symposium, UC Berkeley, USA (2008).

- C. D. Weis, A. Batra, S. Cabrini, J. Bokor, C. C. Lo and T. Schenkel. Detection of low energy single ion impacts in silicon transistors. *Contributed Talk:* American Physical Society March Meeting, New Orleans, USA (2008).

- C. D. Weis, A. Schuh, A. Batra, S. Cabrini, A. Persaud, J. Bokor, C. C. Lo, I. W. Rangelow, T. Schenkel. Single ion doping of silicon transistors at room temperature. *Contributed Poster:* Berkeley Nanotechnology Forum, Berkeley, USA (2008).

- C. D. Weis, A. Batra, S. Cabrini, A. Persaud, J. Bokor, C. C. Lo, I. W. Rangelow, T. Schenkel. Single ion doping of silicon transistors at room temperature. *Contributed Talk:* International Conference on Ion Beam Modification of Materials, Dresden, Germany (2008).

- C. D. Weis, A. Schuh, A. Batra, A. Persaud, I. W. Rangelow, J. Bokor, C. C. Lo, S. Cabrini, D. Olynick, S. Duhey, T. Schenkel. Ion doping for quantum computer structures in silicon and diamond. *Contributed Poster:* National Center for Electron Microscopy & The Molecular Foundry User's Meeting, Berkeley, USA (2008).

- C. D. Weis, A. Batra, A. Persaud, G. D. Fuchs, D. M. Toyli, D. D. Awschalom, T. Schenkel. Formation of color centers in diamond by ion implantation with scanning probe alignment. *Contributed Talk:* Workshop on spin dynamics in diamond, Santa Barbara, USA (2009).

- C. D. Weis, A. Persaud, C. C. Lo, J. Bokor, T. Schenkel. Formation of quantum computer test structures by ion implantation with scanning probe alignment. *Contributed Talk:* Materials Research Society Spring Meeting, San Francisco, USA (2009).

- C. D. Weis, A. Persaud, T. Schenkel. Scanning probe aligned ion implantation and application to the development of quantum computer test structures. *Invited Talk:* Huntsville Ion Beam Institute, Huntsville, USA (2009).

- C. D. Weis, C. C. Lo, A. Persaud, J. Bokor, T. Schenkel. Single ion doping for spin readout transistors. *Contributed Talk:* Silicon Qubit - Quantum Information Science and Technology Workshop, Berkeley, USA (2009).

- C. D. Weis, C. C. Lo, A. Persaud, A. M. Tyryshkin, S. Dhuey, D. Olynick, J. Bokor, S. A. Lyon, T. Schenkel. Process Development for Spin-State Detection in Silicon. *Contributed Poster:* Silicon Qubit - Quantum Information Science and Technology Workshop, Berkeley, USA (2009).

- C. D. Weis, C. C. Lo, A. Persaud, A. M. Tyryshkin, S. Dhuey, D. Olynick, J. Bokor, S. A. Lyon, T. Schenkel. Process Development for Spin-State Detection in Silicon. *Contributed Poster:* National Center for Electron Microscopy & The Molecular Foundry User's Meeting, Berkeley, USA (2009).

- C. D. Weis, D. M. Toyli, I. Chakarov, E. Herrmann, A. Persaud, G. D. Fuchs, F. J. Heremans, D. D. Awschalom, T. Schenkel. Spatial placement limits of nitrogen vacancy centers in diamond via ion implantation. *Contributed Talk:* American Physical Society March Meeting, Portland, USA (2010).

- C. D. Weis, T. Schenkel. Progress in Single Ion Implantation for Qubit Integration in Silicon and Diamond. *Invited Talk:* International Conference on the Application of Accelerators in Research and Industry, Fort Worth, USA (2010).

# Erklärung

Ich versichere, dass ich die vorliegende Arbeit ohne unzulässige Hilfe Dritter und ohne Benutzung anderer als der angegebenen Hilfsmittel angefertigt habe. Die aus anderen Quellen direkt oder indirekt übernommenen Daten und Konzepte sind unter Angabe der Quelle gekennzeichnet.

Weitere Personen waren an der inhaltlich-materiellen Erstellung der vorliegenden Arbeit nicht beteiligt. Insbesondere habe ich hierfür nicht die entgeltliche Hilfe von Vermittlungs- bzw. Beratungsdiensten (Promotionsberater oder anderer Personen) in Anspruch genommen. Niemand hat von mir unmittelbar oder mittelbar geldwerte Leistungen für Arbeiten erhalten, die im Zusammenhang mit dem Inhalte der vorgelegten Dissertation stehen.

Die Arbeit wurde bisher weder im In- noch im Ausland in gleicher oder ähnlicher Form einer Prüfungsbehörde vorgelegt.

Ich bin darauf hingewiesen worden, dass die Unrichtigkeit der vorstehenden Erklärung als Täuschungsversuch angesehen wird und den erfolglosen Abbruch des Promotionsverfahrens zu Folge hat.

Berkeley (USA), den 04. Oktober 2011

(Christoph Weis)

# Thesen

- Antimonionen können durch das Einbringen von Antimon in fester Phase in die in der Arbeit benutzten Elektron-Zyklotron Resonanz Ionenquellen erzeugt werden.
- Niederenergetische Ionen die in elektrische Bauteile einschlagen, können Änderungen in ihren elektrischen Bauteilcharakteristiken hervorrufen.
- Zum Nachweis von einzelnen Einschlägen niederenergetischer Ionen sind hochgeladene Ionen oder die Durchführung bei niedrige Bauteiltemperaturen nicht grundsätzlich von Nöten.
- Elektrische Bauteile mit charakteristischen Grössenordnung von ein paar Mikrometern und kleiner können verwendet werden, um einzelne Ioneneinschläge mittels der Änderungen in den Bauteilcharakteristiken bei Umgebungstemperatur nachzuweisen.
- Mittels Kollimatoren in Cantilevern von Rasterkraftmikroskopen können Ionenstrahlen auf elektrischen Bauteilen und anderen Proben in präziser Art und Weise platziert werden.
- Diese Technik ist sehr vielseitig einsetzbar und kann zur lokalen Dotierung von Silizium-Bauteilen oder Einbringung von Stickstoffatomen in Diamondproben zur Herstellung von Stickstoff-Fehlstellen-Zentren angewandt werden.